Studies on the Influence of PPM-Water-Pollutions in the Working Gas of Square Meter Micromegas Detectors for the ATLAS New Small Wheel Upgrade and Identification of Muons in High Background Environments

Ludwig-Maximilians-Universität München
Department of Physics

Master Thesis in Physics

Sebastian Daniel Trost

Studien über den Einfluss von Wasserverunreinigungen im ppm Bereich des Arbeitsgases von Quadratmeter großen Micromegas Detektoren für das ATLAS New Small Wheel Upgrade und Identifikation von Myonen vor starken Hintergründen

Ludwig-Maximilians-Universität München

Fakultät der Physik

Masterarbeit in Physik

Author: Sebastian Trost

Supervisor: Prof. Dr. Otmar Biebel

Advisor: Dr. Maximillian Herrmann

Submission date: 21.12.2020

Abstract

The Large-Hadron-Collider (LHC) operated by the European Organization for Nuclear Research (CERN) is one of the most extensive and imposing undertakings of mankind. At the time of this thesis the LHC is undergoing major upgrades. The High-Luminosity-Upgrade aims to increase the LHC luminosity tenfold compared to the original design-value. The increased rate of particle collisions will unavoidably lead to a decrease in efficiency of the current detector systems. Accordingly, the experiments positioned around the 27 km long ring are being upgraded. ATLAS, the biggest experiment at the LHC, is planned to undergo several changes to perform effectively under the upcoming conditions. One of the upgrades of the ATLAS detector is the New Small Wheel (NSW) upgrade, which aims to exchange the inner endcap detectors of the muon detector system. The NSW is comprised of two detector technologies, sTGC (small-strip Thin Gap Chambers) for triggering and Micromegas (Micromesh Gaseous Structure) for precision tracking. Four types of Micromegas modules are built by a collaboration of multiple countries and universities.
The Small Micromegas modules 2 (SM2) are being built in Germany. They were developed and commisioned at the LMU Munich, where they are also tested. Micromegas are gaseous detectors utilizing a grounded micromesh 0.12 mm above a micropattern stripanode on positive high voltage, to reconstruct the passage of ionizing particles. SM2 modules are built as quadruplets, allowing particle tracks to be reconstructed by their points of passage in each of their four layers.

In this thesis the performance of SM2 modules is examined under aggravated conditions. At ATLAS the modules will face constant background radiation, called cavern background. The influence of water vapour in the detector gas was studied in the second part of this thesis. Two experiments were executed to investigate the behavior of modules under these influences.
To examine the efficiency of the module under a particle background it was irradiated with neutrons at the tandem accelerator of the MLL Forschungszentrum Garching near Munich. A system of plastic scintillators sandwiching the detector triggered on the passage of cosmic muons to record the events. The clusters recorded during the several days long experiment were initially investigated for their parameters, like cluster charge or size. In this initial step of the analysis characteristic muon cluster parameters are determined to reconstruct tracks from three layers, in order to investigate the efficiency in the fourth layer. This analysis step was also applied to data free of background, recorded with the same module at the Cosmic Ray Facility (CRF). As the CRF uses cosmic muons exclusively, the collected pure muon data yielded insights on the signal characteristic of muons in the SM2 module. Ultimately the cluster timing was determined as the characteristic muon cluster parameter, which together with geometrical attributes of the experiment enabled the reconstruction of almost pure muon tracks. The efficiency showed a direct correllation with the neutron background.
The CRF was also used as the location for an several weeks long study, aiming to observe the effect of ppm water-pollutions in the Ar:CO_2 working gas of the SM2 detector. For the

study a humidifier was built to allow the induction of well defined water-portions in the working gas within an accuracy of a few hundred ppm. The study verified the detrimental effect of prolonged humidification in the working gas of SM2 modules by observing the decline in HV stability.

Zusammenfassung

Der Large-Hadron-Collider (LHC), der von der Europäischen Organisation für Kernforschung (CERN) betrieben wird, ist eines der umfangreichsten und imposantesten Projekte der Menschheit. Zum Zeitpunkt dieser Arbeit erfährt der LHC mit dem High-Luminosity-Upgrade eine erhebliche Aufrüstung. Das High-Luminosity-Upgrade zielt darauf ab, die Luminosität des LHC im Vergleich zum ursprünglichen Designwert zu verzehnfachen. Die erhöhte Rate an Teilchenkollisionen wird unweigerlich zu einer Abnahme der Effizienz der aktuellen Detektorsysteme führen. Entsprechend werden die Experimente, die um den 27 km langen Ring positioniert sind, aufgerüstet. ATLAS, das größte Experiment am LHC, soll mehrere Upgrades erhalten, um unter den kommenden Bedingungen effektiv arbeiten zu können. Eines der Upgrades ist das New Small Wheel (NSW) Upgrade, welches den Austausch der inneren Endkappendetektoren des Myonendetektorsystems zum Ziel hat. Das NSW nutzt zwei Detektortechnologien, sTGC (small-strip Thin Gap Chambers) die hauptsächlich as Trigger zum Einsatz kommen und Micromegas (Micromesh Gaseous Structure) zur Präzisionsverfolgung. Vier Typen von Micromegas-Modulen werden durch eine Kollaboration von mehreren Ländern und Universitäten gebaut.
Module des Typs small Micromegas Module 2 (SM2) werden in Deutschland gebaut. Sie wurden an der LMU München entwickelt und in Betrieb genommen und werden hier auch getestet. Micromegas sind Gasdetektoren, die ein geerdetes Mikromesh 0,12 mm über einer Mikropattern-Stripanode an positiver Hochspannung verwenden, um den Durchgang von ionisierenden Teilchen zu rekonstruieren. Die SM2-Module sind als Quadruplet aufgebaut, so dass die Teilchenspuren anhand ihrer Durchgangspunkte in jeder der vier Schichten rekonstruiert werden können.

In dieser Arbeit wird die Performance der SM2 Modules unter Störgrößen untersucht. Am ATLAS werden die Module einer enormen Hintergrundstrahlung ausgesetzt. Der Einfluss von Wasserdampf im Detektorgas wurde im ersten Teil dieser Arbeit untersucht. Es wurden zwei Experimente durchgeführt, um das Verhalten der Module unter diesen Einflüssen zu untersuchen.
Um die Leistungsfähigkeit des Moduls unter einem Teilchenhintergrund zu untersuchen, wurde es am Tandembeschleuniger des MLL am Forschungszentrum Garching bei München mit Neutronen bestrahlt. Ein System von Plastikszintillatoren, welches den Detektor sandwichartig umgibt, löste beim Durchgang von kosmischen Myonen aus und zeichnete die Ereignisse auf. Die während des mehrtägigen Experiments aufgezeichneten Cluster wurden zunächst auf ihre Parameter, wie Cluster-Ladung oder Größe, untersucht. In diesem ersten Analyseschritt werden charakteristische Myonen-Cluster-Parameter bestimmt. Diese erlauben die Rekonstruktion von Spuren aus drei Lagen, um die Effizienz in der vierten Lage zu untersuchen. Dieser Analyseschritt wurde auch auf untergrundfreie Daten angewendet, die mit dem gleichen Modul an der Cosmic Ray Facility (CRF) aufgenommen wurden. Da die CRF ausschließlich kosmische Myonen verwendet, lieferten die gesammelten reinen Myonendaten Erkenntnisse über die Signalcharakteristik von Myonen im SM2-Modul. Letztendlich wurde das Cluster-Timing als charakteristischer Myonen-Cluster-Parameter

gewählt, der zusammen mit geometrischen Eigenschaften des Experiments die Rekonstruktion nahezu reiner Myonen-Spuren ermöglichte. Die Effizienz zeigte eine direkte Korrelation mit dem Neutronenhintergrund.
Die CRF wurde auch als Standort für eine mehrwöchige Feuchtigkeits-Studie genutzt, die darauf abzielte, den Effekt von ppm-Wasser-Verunreinigungen im Ar:CO_2-Arbeitsgas des SM2-Detektors zu beobachten. Für die Studie wurde ein Befeuchter entwickelt, der einen gut definierten Wasseranteil im Arbeitsgas mit einer Genauigkeit von einigen hundert ppm ermöglicht. Die Studie zeigte einen schädlichen Effekt einer andauernden Befeuchtung im Arbeitsgas von SM2-Modulen durch die Beobachtung einer eindeutigen Abnahme der HV-Stabilität.

Contents

Chapter 1

Introduction

Motivation

The field of physics emerged with mankind describing nature through their senses, mathematics and logic. Microscopes revealed a world too small for our eyes. Observed Brownian Motion gave only hints at the existence of atoms or even smaller particles. To investigate events so far beyond our senses, mankind has undertaken ever increasing efforts like the Large Hadron Collider (LHC) operated by European Organization for Nuclear Research (CERN). At the time of this thesis, the LHC is being upgraded even further, with the High Luminosity LHC (HL-LHC) aiming for an increase in luminosity exceeding ten times its design value (ATLAS Collaboration, 2013). Particle bunches will see significantly stronger focusation at the expriments, resulting in more intense collisions. The resulting environment demands new hardware for the experiments located around the nearly 27 km long ring tunnel.
At the "A Torodial LHC ApparatuS (ATLAS)", the biggest experiment at the LHC, the New Small Wheel project will replace its predecessor as part of the ATLAS muon spectrometer. One of the four module-types used as Micromegas tracking detectors is the Small Module 2 (SM2). These SM2s are gaseous detectors designed for precision tracking and were developed and built by a German collaboration. At ATLAS they will face strong background irradiation, as well as temperature gradients of several degrees. The humidity of the detector gas should be well controlled.

Accordingly, this thesis investigates the performance of these SM2 Micromegas modules by analyzing the efficiency under an accelerator-generated neutron background, as well as observe the impact of induced water portions in the $ArCO_2$ 93:7 detector gas. The performance under backgrounds is obviously essential for any particle detector to be oprated at an extensive project like ATLAS. The effect of humidity is however uncertain. Several groups, working on a variety of detectors, reported varying effects after humidifying their systems. From detrimental effects on the performance, which one might promptly assume for any pollution of the working gas, to beneficial behavior, like regenerating high voltage stability. To this end a module was flushed with moistened working gas for an extended time period and its High Voltage (HV) behaviour was observed.

Structure of the Work

Chapter 2 introduces the wider frame of this thesis, giving brief overviews of the LHC and ATLAS, explaining the structure and working principle of the SM2 module and introducing the Cosmic Ray Facility (CRF), which was used as a pure-muon reference for the data collected at the Tandem experiment and at which the water pollution studies took place.

In Chapter 3 the water pollution studies and the humidifier are described. This chapter will focus in the development of a humidifying device and its application at the CRF.

Chapter 4 forms the core of this thesis, presenting the evaluation of the Tandem experiment. First the setup of the experiment is explained. The evaluation of the expriment begins with the principle of track reconstruction used for the analysis of the collected data. The same analysis was applied to data taken at the CRF. The comparison with the pure muon data from the CRF and the characteristics of the setup at the tandem formed the basis for implementations, like corrections and applied cuts. The resulting efficiency-analysis of the module under neutron background will be presented.

Finally Chapter 5 will discuss the findings and give an assessment of potential follow-up research.

Chapter 2

Overview

This chapter provides the context and background to the thesis. The LHC at CERN and the ATLAS experiment are introduced briefly, followed by the ATLAS New Small Wheel (NSW) upgrade. Afterwards the SM2 module and its features relevant to this thesis are explained. Finally the CRF is introduced.

2.1 The Large Hadron Collider and ATLAS

2.1.1 The Large Hadron Collider

The LHC is a circular accelerator with a nearly 27 km long ring-tunnel (fig. 2.1) (Brüning et al., 2004). Protons and ions are created and pre-accelerated at several linear accelerators and then progressively accelerated further by consecutive secondary accelerators before being injected into the main ring tunnel in bunches of particles. Half of the bunches run along the ring contrary to the direction of the other half. Opposing bunches are then collided at designated intersection areas with experiments like ATLAS purpose-built around the spot of collision.

At the time of this thesis, the LHC is being upgraded in view of the High Luminosity LHC (HL-LHC). The final upgrade is aiming for a tenfold increase in luminosity compared to the design value of the LHC (ATLAS Collaboration, 2013). Luminosity is a measure of particle collisions per given area and time and is measured in (femto-)barn^{-1}. New superconducting quadruple magnets will be installed at the ATLAS (and CMS) experiments, focussing incoming bunches with magnetic fields of presumably up to 12 Tesla - one and a half times the field strength prior to the shut down. To perform under the unprecedented conditions of the HL-LHC, all the major experiments at the LHC undergo major upgrades as well.

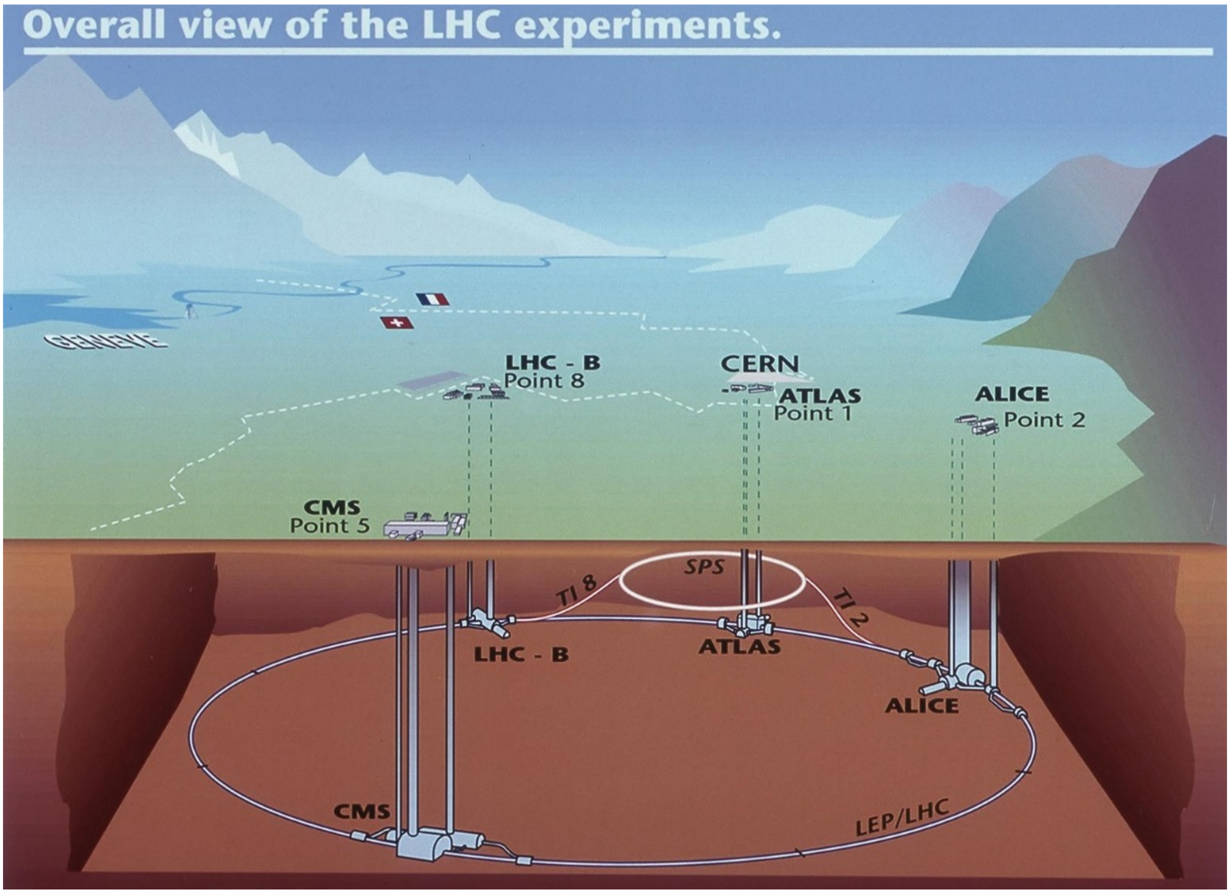

Figure 2.1: Depiction of the LHC at CERN near Geneva with the locations of the experiments ALICE, ATLAS, CMS and LHCb. Taken from (Caron, 1998).

2.1.2 The ATLAS Experiment

ATLAS itself is a general-purpose particle detector, designed to observe the plethora of particles produced at the beam-intersection simultaneously (ATLAS Collaboration, 2008). It is renowned for its involvement in the search for and investigation of the Higgs particle. The detector is a combination of several detector systems tailored to specific particles, capable of tracking and calorimetrical reconstruction. The whole system is build cylindrically around the collision-point, parallel to the beam-axis with end caps at each end of the cylinder. Muons traverse the inner systems almost unhindered. Thus the ATLAS muon-spectrometer encompasses the whole detector-system (ATLAS Collaboration, 2008).

The ATLAS muon-spectrometer consits of two outer and two inner endcap-wheels as well as three layers of cylindrically arranged tracking chambers (see fig. 2.2 and fig. 2.3). This thesis exclusively focusses on the SM2 modules applied in the NSW in preperation for the HL-LHC. As the current Monitored Drift Tube (MDT) detectors will supposedly experience losses in efficiency at this position, the NSW will replace its predecessor on both inner endcap-wheels (depicted for one side as the left (green) component in fig. 2.3).

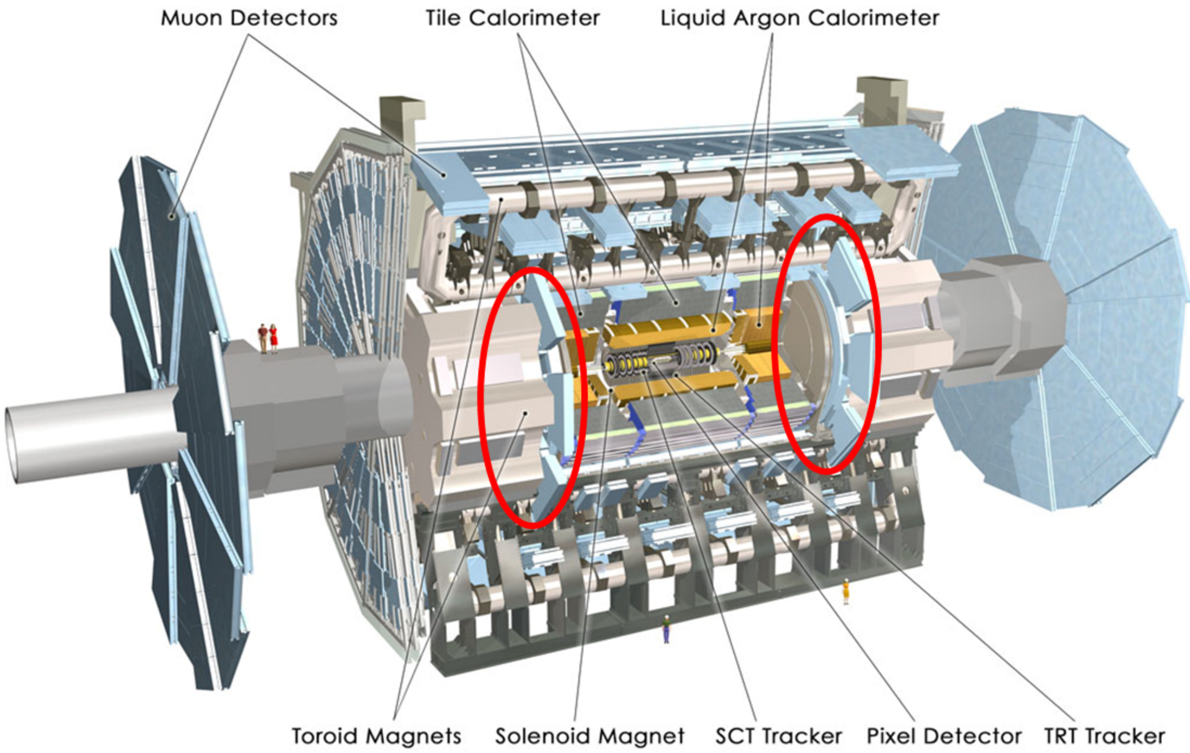

Figure 2.2: Cross-section of the ATLAS detector. Highlighted in blue are the components of the muon-spectrometer. This thesis focusses on the inner endcaps (marked in red), of which the SM2 modules are part of. Taken from (Pequenao, 2008).

The new detectors aim to perform under the higher collision-rates of the HL-LHC and aid in the identification and rejection of false triggers.

2.2 New Small Wheel Project

The NSW (ATLAS Collaboration, 2013) project is a collaboration of several groups working across various nations to prepare new detectors, fit to perform at higher rates. The wheel will be covered by tracking modules of four types. The Large Micromegas Module 1 (LM1) is being built by a French collaboration at the Commissariat *à* L'*é*nergie atomique (C.E.A) in Saclay near Paris, the Large Micromegas Module 2 (LM2) by a Greek-Russian collaboration in Thessaloniki and Dubna and the Small Micromegas Module 1 (SM1) is built at the Istituto Nazionale di Fisica Nucleare (INFN) by an Italian collaboration. Finally the SM2 is built by a German collaboration, lead by the Ludwig-Maximilians-Universität München (LMU).

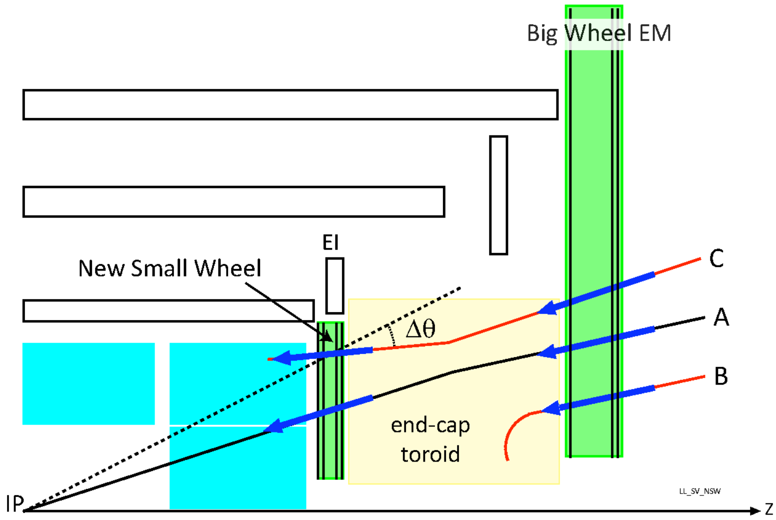

Figure 2.3: Positioning of the small (left) and the big (right) endcap-wheels. In conjunction they generate redundancy in the online tracking, allowing for reduction of false-trigger-rates at trigger level. Taken from (ATLAS Collaboration, 2013).

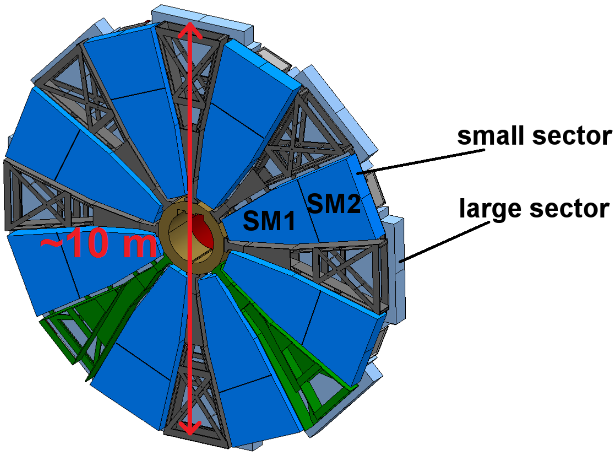

(a) New Small Wheel

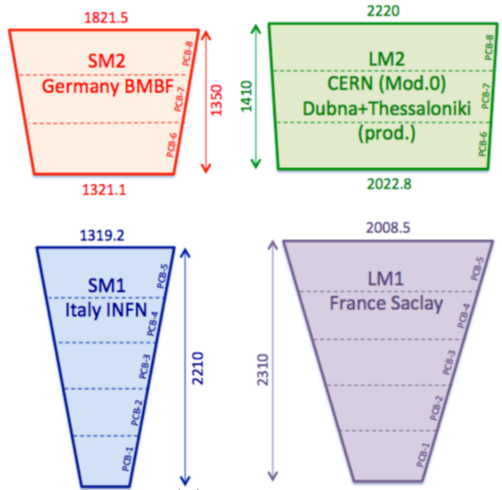

(b) NSW modules

Figure 2.4: (a) Layout of the New Small Wheel planned to replace the current inner endcaps of the ATLAS muon spectrometer. (b) Dimensions of the four Micromegas module types of the New Small Wheel. The Small Module 2 is the object of this thesis. Taken from (ATLAS Collaboration, 2013).

To cover the disc shaped end-caps, four trapezoidal module types are being built (see fig. 2.4 (ATLAS Collaboration, 2013)). These new detectors utilize two technologies to further the redundancy in the whole detector-system. Small-strip Thin Gap Chambers (sTGC)s, which will primarily be used for triggering and Micromesh Gaseous Structure (Micromegas) for precision tracking. The SM2 modules are of the latter kind. All module-types of the NSW are four-layered and shaped as trapezoids, so to cover the whole wheel (see fig. 2.4a).

2.3 Resistive Strip Micromegas Modules

2.3.1 Working Principle

This section describes the working principle and signal generation of the SM2 Micromegas detector. As this thesis focusses exclusively on the SM2 detector, principles and details are presented.
Note that the Micromegas technology (Giomataris, Rebourgeard, Robert & Charpak, 1996) is seeing ongoing development beyond its application at ATLAS (Bortfeldt, 2014), (Klitzner, 2019).

Energy-Deposition of Minimum-Ionizing-Particles

$$-\left\langle \frac{\mathrm{d}E}{\mathrm{d}x} \right\rangle = 4\pi r_e^2 m_e c^2 N_0 \frac{Zz^2}{A\beta^2} \left[ln \left(\frac{2m_e c^2 \beta^2}{I(1-\beta^2)} \right) - \beta^2 \right] \tag{2.1}$$

Table 2.1: Variables of the Bethe-Equation

variable	value	unit	description
re	2.8179403227(19)	m	classical electron radius
me	$9.10938356(11)\ 10^{-31}$	kg	electron mass
c	299792458	m/s	speed of light
N0	$6.02214076\ 10^{23}$	mol-1	Avogadro constant
Z			material atomic number
z			projectile charge in unit-charges
A			material mass number
β	v/c		velocity of the traversing particle
I	Z·10eV	eV	effective ionization potential of the material

Heavy charged particles traversing a medium lose energy over the distance traveled due to electro-magentic interactions with the medium as described by the Bethe-Equation displayed in eq. 2.1 (variables described in tab 2.1). (Bethe, 1930)
This stopping-power can be interpreted as a mean rate of energy-depostion per length traveled. For sufficiently high energy depositions, ionization occurs in the medium, which is the effect Micromegas detectors make use of.
The amount of energy deposited varies, depending on the particle in question, its momentum and the medium traversed (see fig. 2.5). For a muon the stopping-power has a minimum around a $\beta\gamma$ of 3 (or a momentum of 300MeV/c). Particles in this momentum-regime are called Minimum Ionizing Particle (MIP) - cosmic muons fall into this group.

A muon traversing the SM2 working gas-mixture of 93 volume % argon (Ar) and 7 volume % carbon-dioxide (CO_2) creates electron-ion-pairs which lead to a signal.

The single electrons created by the primary ionization need to be seperated from the ions and then amplified to create reliable and distinguishable signals. This is achieved by the application of high electrical fields.

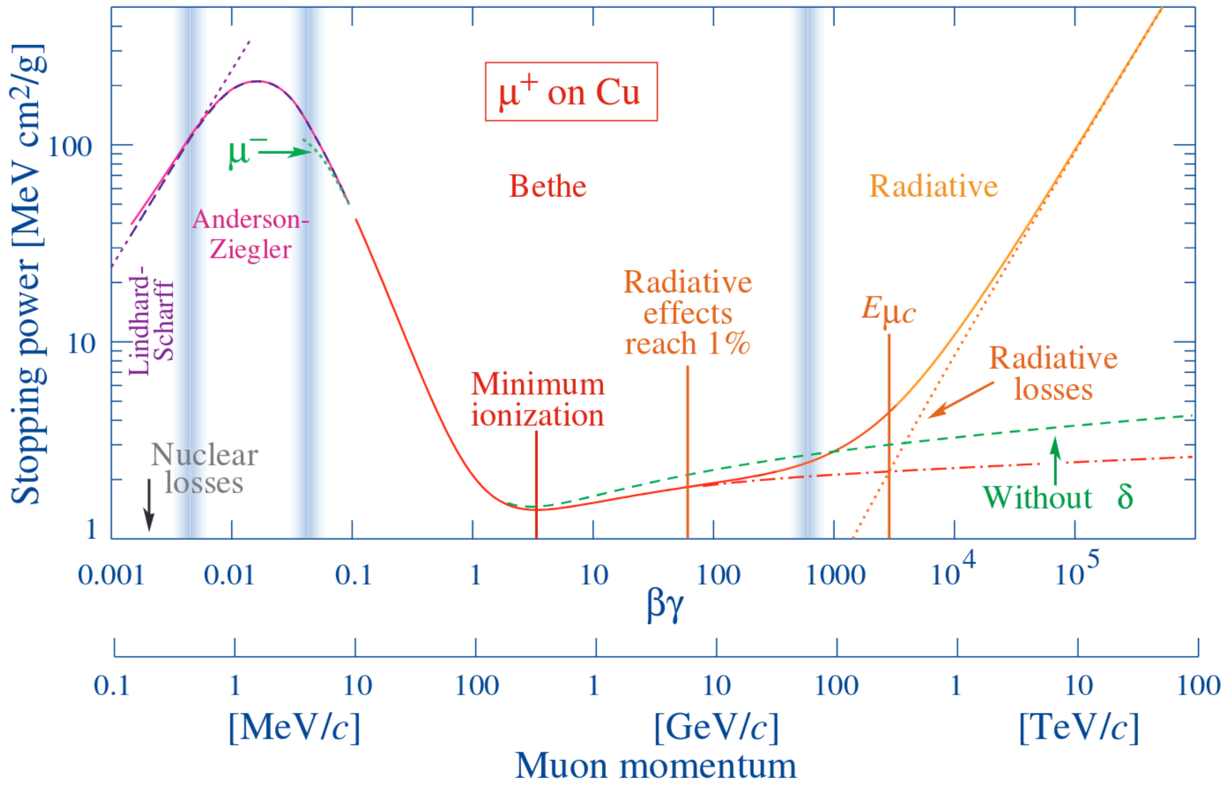

Figure 2.5: Energy deposition as a function of muon-momentum for an anitmuon on copper. (Olive et al., 2014), (Groom et al., 2001). The shape of the graph is similar/identical for all combinations of materials and charged particles (with the exception of electrons or lighter paricles).

Signal Generation via Applied High-Voltage Fields

To create a sufficiently strong and reliable signal, the electron-ion-pairs created by the primary ionization have to be seperated and kept from recombination or diffusion to the utmost. The gas-volume is sandwiched by a planar cathode set to -300 volts and a grounded micromesh made from stainless steel parallel to the cathode. At a distance of 5 mm between the cathode and the mesh, the resulting electrical field has a strength of 0.6kV/cm (see fig. 2.6a). Like a plate capacitor, the planar and parallel construction of the module creates a field of homogeneous strength.

Any created electron drifts along the field towards the mesh at a drift-velocity of 47 μm/ns in the Ar:CO_2 working-gas. The anode is positioned parallel to the mesh and on the opposite side to the cathode and is operated at a voltage of +570V at a distance of 0.12 mm to the mesh. The amplification gap between the mesh and the cathode recieves a field of about 47.5 kV/cm. This field causes the electrons to create Townsend-Avalanches

(Townsend, 1910), increasing the number of electrons by a factor of 5000 to 10000 in the amplification region.
Copper readout strips underneath the anode allow for the precise recording of the position of an avalanche. The copper strips are covered by the anode resisitive strips to prevent discharges.

2.3.2 SM2-Module Layout

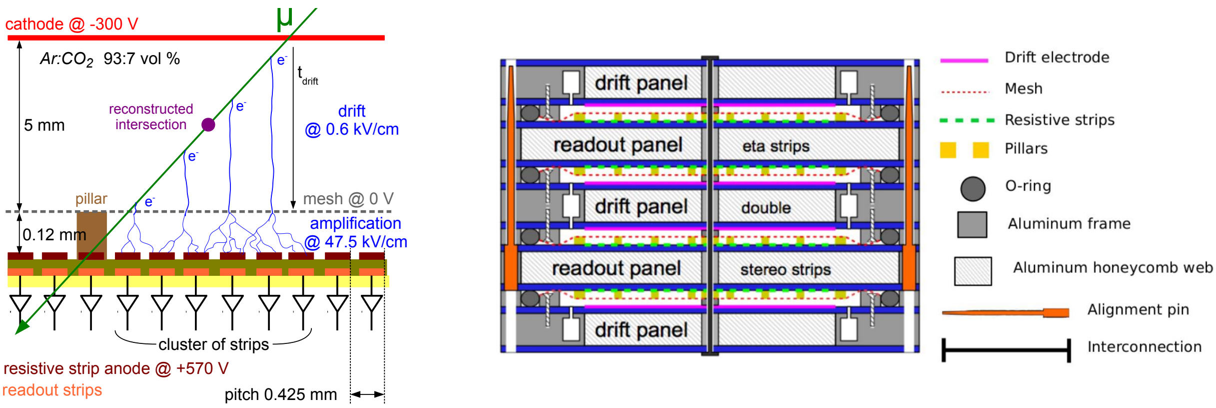

(a) Micromegas working principle (b) SM2 cross-section

Figure 2.6: (a) SM2 Micromegas modules utilize three parallel electrodes: The catode at -300V, a grounded stainless steel micromesh and the strip-anode at +570V. The mesh seperates the volume into a drift region and an amplification region. MIPs like muons create free electrons in the working-gas which follow the field towards the mesh. Entering the amplification region, the electrons are amplified to electron avalanches. The distance in the amplification region is garantueed by insulating pillars. The signals are collected by the readout-strips, allowing for position and track reconstruction. (Herrmann, 2019)
(b) An SM2 module is built from five panels. The four strip layers are attached to the two readout panels in pairs, one for the eta layers and one for the stereo layers. Each pair is orientated opposingly and attached to one of the four active gas volumes. The central drift panel contains the two inner active gas volumes. (Sidiropoulou, 2018)

The SM2 module contains four of the previously described Micromegas volumes along with the corresponding drift and readout panels. The four layers are called Outer ETA layer (EO), Inner ETA layer (EI), Inner Stereo layer (SI) and Outer Stereo layer (SO). The direction perpendicular to the planes of the layers is defined as the z-axis of the module.
The anodes for the eta and the stereo layers are assembled pairwise as readout-panels. As a result the quadruplet is built from five panels: two outer drift panels, two readout panels and the central drift panel, which is shared by the inner layers (see fig. 2.6b). The central drift panel holds the cathode for both inner layers, while the outer drift panels each have one cathode at their inner surfaces.

The SM2 has an active surface-area of roughly $2m^2$ covered by 3072 parallel strips per layer. The strips of the eta layers run parallel to the parallel edges of the trapezoidal frame (see fig. 2.7a). Through the number of a strip detecting a signal, the location of the signal is determined precisely in direction perpendicular to the strips. This defines the Precision (P) direction of the module as perpendicular to the strips. Each strip has a width of 0.325 mm. In the eta layers the centers of adjacent strips are 0.425 mm apart. This is called pitch and the measure for the precision of the module. With 0.42485 mm the pitch of the stereo layers is smaller. The deviant width of the stereo pitch is a result of the stereo layers being angled by 1.5 degrees towards the eta-strips and by 3 degrees towards each other (see fig. 2.7b). The angle between the stereo layers enables reconstruction along the Non-Precision (NP) direction.

The SM2 readout-anodes are segmented into three Printed Circuit Boards (PCB) (see fig. 2.7a). Six Front End Connector cards (FEC) are connected to a single detector plane. Each FEC covers 512 strips of each layer. To cover each of the three PCBs, the FECs are positioned alternating on opposing dissimilar edges of the trapezoid, such that each PCB has half of its strips connected to one FEC at each edge. Each FEC is connected to one adapter-board per layer, each of which holds four APVs. One APV covers 128 strip. An APV is an Application Specific Integrated Circuit (ASIC) and is used as an interim replacement as development of the readout-electronics is ongoing (De Geronimo et al., 2012). The version used is the so-called APV25.
The modules are operated at slight overpressure. One applicable way to generate the overpressure is a bubbler at the end of the gas line(which will be discussed in chapter 4).

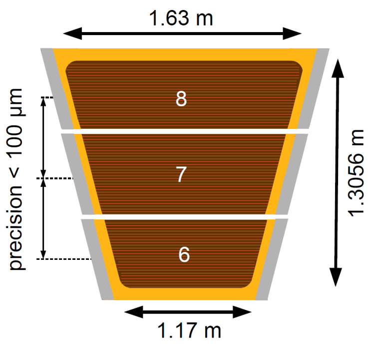

(a) SM2 segmentation

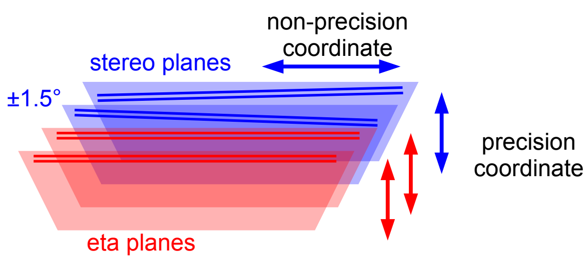

(b) Stereo alignment

Figure 2.7: (a) Dimensions and strip-layout of the SM2 readout-anode (not to scale). Each layer has 3072 strips forming the active area brown. In the Eta layers the strips run parallel to the parallel edges of the trapezoid. The strips are equally distributed across three segments, called small, central and large board. Each board is connected to one readout-PCB. (Herrmann, 2019)
(b) The strips of the Stereo layers are inclined by 1.5° compared to the Eta-strips and opposing each other. This enables the component along the x-axis (or NP) of points of passage to be calculated for particles registered in both Stereo layers. (Herrmann, 2019)

2.3.3 Signal Evaluation

Centroid cluster position: The SM2 module is designed as a precision-tracking detector. The point of passage of a charged particle is determined by the cluster of strips recieving the signal. To take this effect into account, the position of a cluster is determined by the so-called centroid position-reconstruction: For all strip-channels attributed to a cluster the channel-numbers are weighted by their individual charge and the resulting values summed up. The total value of charge-weighted channels is then divided by the total sum of charges in the cluster (depicted in red in fig. 2.8 a)). This charge-weighted position is also referred to as the centroid of the cluster.

$$y_{CPR} = \frac{1}{Q} \sum_{i=1}^{n} q_i \cdot y_i \tag{2.2}$$

total charge	$Q = \sum_{i=1}^{n} q_i$
number of strips in the cluster	n
strip with charge q_i:	y_i

Table 2.2: parameters for eq.2.2: Charge weighted cluster-position reconstruction

To get a more intuitive position-value, the centroid-position in strips can be multiplied by the pitch of the corresponding layer (0.425 mm per strip in the eta-layers) to get the position in mm. The centroid-positions of clusters are also essential to calculate the Non-Precision position, as will be discussed in chapter 5.

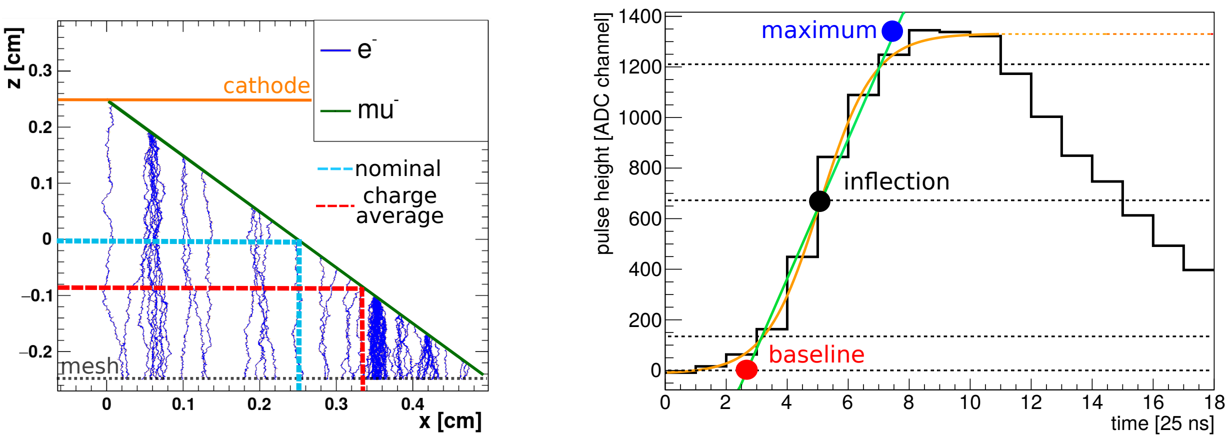

(a) Charge-weighted Centroid

(b) Signal Time Evolution

Figure 2.8: (a) Simulation of the inhomogeneous ionization along the muon-track (green). (Flierl, 2018) (b) Determination of the signal-time for a single strip. Via application of an inverse Fermi-funtion on the time evolution of the charge-signal, the inflection-point can be found and used as a stable signal-time. (Herrmann, 2019)

Signaltime: The timing of a signal is an essential cluster-property. The SM2 is designed for high frequency sensitivity, but the readout electronics are still under development. The APVs used are an interim solution, capable of measuring timing in teps of 25 ns. The

timing of a cluster is calculated from the timing of its individual strips.
At the tandem-experiment the timing of all clusters of each event was recorded over a period of 24 timesteps (timebins). The timeframe of a recorded signal is defined relative to the event-trigger with a determined delay. Similar to the centroid of a cluster,an improved position is reconstructed from a combination of the timings of the strip signals. As discussed by (Flierl, 2018), muons tend to deposit energy in an inhomogeneous matter along their track in the drift region (see fig. 2.8 a)).

The charge-signal on each singular strip is recorded (see fig. 2.8b). To assign a specific time to the signal of a strip, an inverse-Fermi-function is fitted to the rising-edge of the signal. The inverse- Fermi-function is almost independent of the height of the pulse. This approach determines the 50%-time of the signal via the inflection-point of the inverse-Fermi-function and the slope of the rising edge (Herrmann, 2019). The inflection-point is defined as the signal-time of the strip.
For a full cluster, being comprised of several signal-recieving strips, the charge-averaged clustertime is used. Similar to the centroid-method, all channels belonging to the cluster have their time weighted with the channel charge and summed up. The sum is divided by the total charge of the cluster, yielding the charge-averaged clustertime.

2.3.4 High Voltage stability

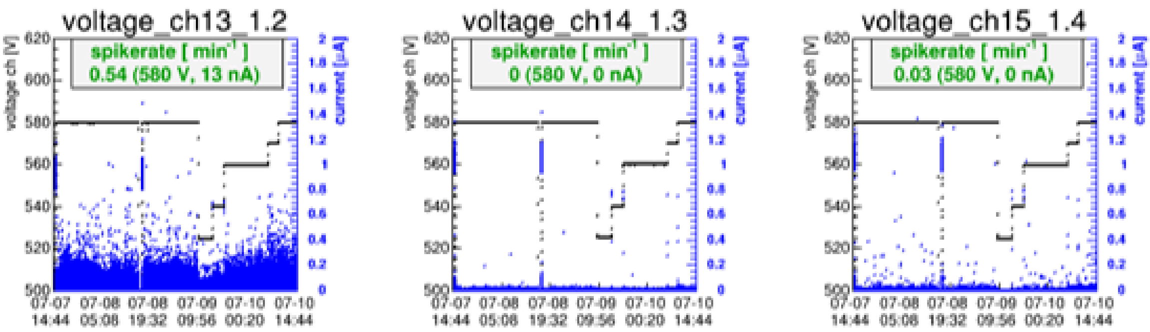

Figure 2.9: HV plots of three sectors of an SM2 Micromegas displaying the voltage applied (black) and currents (blue) as a function of time. The step-like increases of the voltage mark the voltage scan, a procedure performed on modules at the beginning of an measurement at the CRF.

As described SM2 modules use ionization of the Ar:CO_2 working-gas to detect muons, by guiding and amplifying the generated electrons along the HV field lines to the readout-strips. The module is operated at high voltages to guarantee seperation of the ion-electron pairs, maximize the signal-amplification and to neutralize the ions in the amplification-region.
The term 'HV-stability' describes the ability to hold stable voltages without the occurence of discharges or leakage-currents caused by the field. Discharges occur if the number of free

electrons exceeds the Raether-limit (Raether, 1964), creating a conducting plasma between the anode and the mesh.

These can permanently damage the anode. Their presence distorts the field and equalizes the potential in the amplification region, reducing the efficiency of the detector (Herrmann, 2019). Therefore discharges have to be prevented.
The water-pollution-studies aimed to clarify wether water-portions in the working gas have a beneficial effect, like for the ATLAS Cathode-strip chambers (CSC) detectors, or a detrimental effect on the HV-behaviour.

Each of the four detector-layers has six HV-sectors. All 24 sectors of the detector can be monitored for their HV-behaviour. Fig. 2.9 exemplarily shows plots for three of these 24 sectors. Ideally currents (blue) are at 0 nA and the voltage (black) is keept a stable level. Channel 14 (sector three at layer 1, i.e. one half of the centralPCB) shows few and small currents. By comparison channel 13 at the neighbouring board of the same layer shows significant currents.

2.4 Cosmic Ray Facility

The CRF in Garching by Munich, originally a purpose-built facility for testing Monitored Drift Tubes (MDT), was modified for the evaluation and calibration of SM2 modules (Biebel et al., 2003), (Kortner, 2002), (Rauscher, 2005). To evaluate the modules, the CRF encompasses one module at a time acting as a reference detector system. Able to detect and reconstruct passing cosmic muons - hence the name - the CRF utilizes cosmics as a particle source. The CRF is used for the water-pullution studies, as well as a source of reference data for the neutron-background analysis (see chapters 4 and 5).

MDTs are drift chambers comprised of layers of aluminium tubes, each with tensioned wires at its center. The wires are set to high voltage, leading to avalanches of electrons once a particle causes ionization in a tube. The muon path can be reconstructed in two dimensions from the tube position and the signal time distribution (see fig. 2.10 right).

The precision-axis of the CRF is given perpendicular to the orientation of the MDT tubes (see figure 2.10). The z-axis is defined pointing skywards - corresponding with the estimated mean inclination of cosmic muons hitting the system. The x-axis of the CRF is defined parallel to the MDT tubes, allowing for precise track-reconstructions in the y-z-plane. This orientation is chosen to coincide with the precision-direction of an inserted SM2 Micromegas, such that the reference tracks can be matched accurately. Each of the two MDT chambers is arrayed as a pair of triple-layers to reconstruct muons using multiple hit-points. The SM2 sits between two of these chambers.

For triggering, three layers of plastic scintillator are used in coincidence. These are aligned parallel to each other along the y-axis and therefore perpendicular to the MDTs. This allows the CRF to coarsely resolve the x-axis component of muon-tracks. The scintillator-

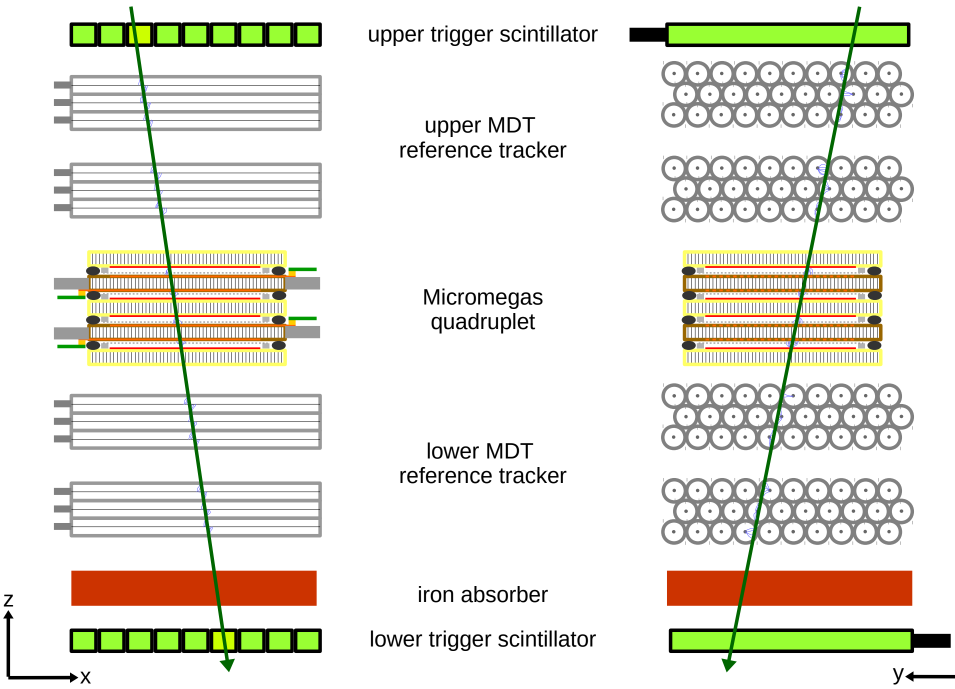

Figure 2.10: Sketch of the CRF setup and muon detection depicted from two sides. The Micromegas module is positioned between two MDT reference trackers. The MDTs are oriented to be parallel to the the strips of the inserted module, such that the precis ion coordinates of the CRF and the SM2 module align. A muon path can be reconstructed in the y-z-plane. Taken from (Herrmann, 2019). (Sketch not to scale)

layers encompass the whole CRF, with one layer at the top and two at the bottom. An iron absorber of 34 cm thickness blocks low-momentum muons. It sits just above the bottom trigger-scintillators.

The final feature of the CRF is a sliding holding structure on which a SM2 module is placed for insertion (see figures 2.11 a) and b)). This allows to align the module and connect the readout electronics outside of the spacial confinements of the CRF. This is a necessity as the MDTs are precisely positioned and sensible to deformation. The module can then simply be pushed into the predetermined position.

Measurements at the CRF are usually taken over a peroid of several days to a few weeks. During this time several million muons are measured. This thesis uses pure muon data as a reference of the characteristics of muon signals in the analysis of the tandem data. Furthermore the water-pollution-studies took place at the CRF, as these were time intensive and needed running modules.

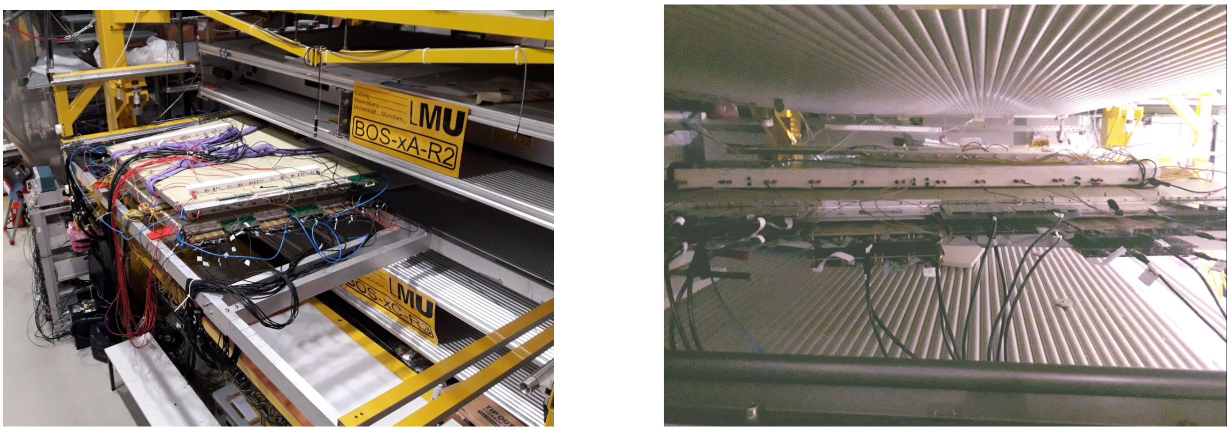

(a) SM2 module on the CRF's sledge

(b) SM2 module inside the CRF

Figure 2.11: (a) To insert an SM2 module into the CRF it is positioned onto a sledge. This allows to position and orientate the module and connect the readout electronics without endangering the sensible MDTs. (b) The prepared module in position between the MDTs. Note the MDT orientation parallel to the strips of the module. Pictures taken from (Herrmann, 2019).

Chapter 3

Water-Pollution Studies

At the ATLAS detector warm and humid conditions are present. With a diameter of roughly 23 m and an considerable amount of readout electronics the detector sees a temperature gradient of several degrees (Aleid, 2020). As measurements in the CRF have shown, the modules emit water at their gas outlet. This inner humidity can have several reasons. New modules are wet cleaned thoroughly during assembly and contain water despite active drying in a purpose-built drying cabinet. They also draw in water from their surrounding environment during storage or gas outages while in operation.
During operation, the module is constantly flushed with a dry Ar:CO_2 93:7 gas-mixture. Over several days the module humidity output reduces until an equilibrium is reached. This equilibrium was at roughly 2000 ppm in the CRF at a gas flowrate of 15 l/h. This indicates that water permeates the detector along its surfaces.

The incentive to investigate the HV-stability is inspired by (Iengo, Alviggi, Iodice & Sekhniaidze, 2018). Several groups, working on different gas-detector technologies, had varying results when inducing water portions around 4000 ppm into their detectors. From positive effects, like a regeneration of HV-stability and reduction in spark-rates to detrimental results, like increased discharge probabily at lower gain rates - the widely different behaviour of related detector-types made corresponding investigations of the SM2-module necessary. To study the effect of water within the detector and the working gas, an affordable yet tunable solution had to be found. Therefore a humidifier made from simple components was built.

3.1 Humidifier

In this chapter the design and application of the humidifier are discussed. The studies took place at the CRF, as modules are operated there continously for extended durations, usually several days to weeks. To add a water-portion to the working gas, the humidifier is integrated into the gas-system right before the module (see fig. 3.1). A test-module was operated with the standard working-gas of Ar:CO_2 in the ratio 93:7 at a flow rate of 15 l/h. To connect the gas-system to the humidifier, it was built with the same FESTO© tubing components (see Appendix) as used on the modules. Likewise this allowed to seamlessly connect the humidifier to the module.

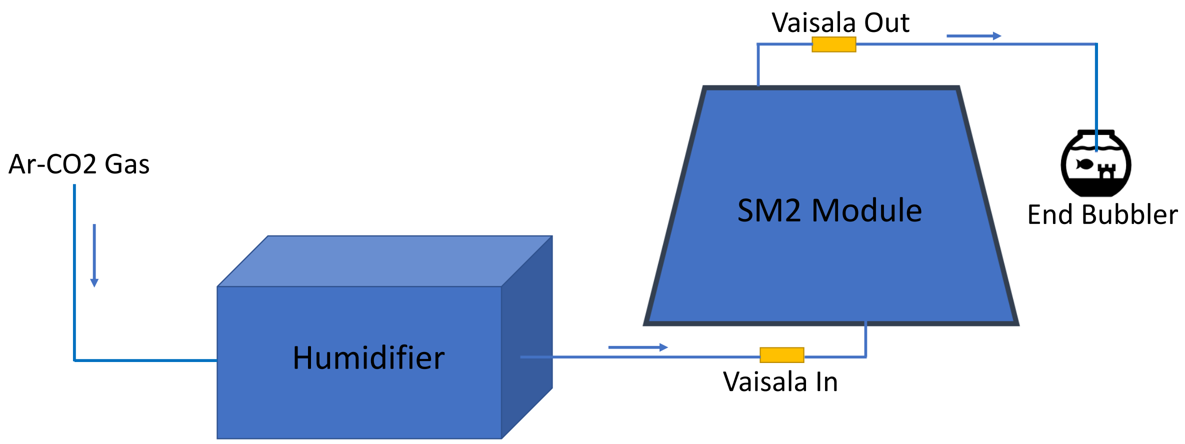

Figure 3.1: The humidifier is plugged into the gas tubing in front of an SM2. Vaisala© Drycap® dewpoint-transmitters (see Appendix) (Vaisala) (orange) record the humidity in the Ar:CO_2 working-gas before and after the module. An end-bubbler generates a slight overpressure inside the module.

The humidifier has several components, which in ensemble grant a tunable source of water induction. The goal was to reach an absolute water portion of 4000ppm in the working gas with a minimal fluctuation. The final device allows initial tuning of the water portion with a precision of less then 10ppm. The fluctuation of the set mixing-humidity could then only be limited to a few hundred ppm over several hours, as changes in temperature and air pressure have an impact on the humidifaction. The temperature of the CRF is kept within a few degrees thanks to climate control, the air pressure cannot be controlled.

3.1.1 Humidifier Layout

The layout is depicted in fig 3.2. The main element of the humidifier is a water reservoir which humidifies the passing Ar:CO_2 gas prior to the detector. Purely blowing gas through the water reservoir would result in full saturation of the gas flow. Therefore, the gas flow is split into two paths, called the *wet path* and the *bypass path*. The gas in the former is humidified at the reservoir while the latter is kept pure for mixing. Mixing is simply done by reuniting both paths.

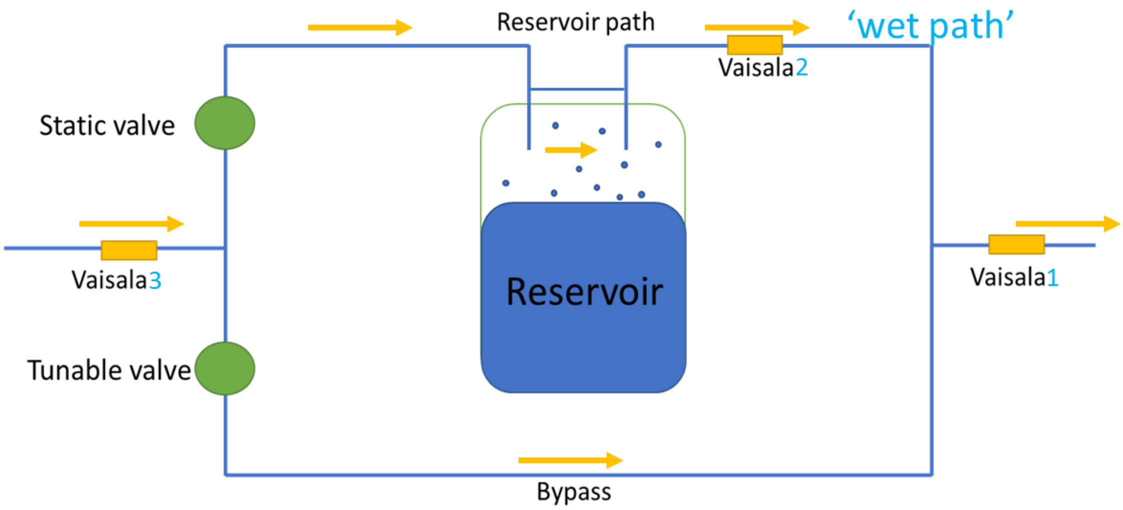

Figure 3.2: Layout of the Humidifier. Incoming gas (arrows)is split into a reservoir path (also referred to as wet path) and a bypass (also dry path). At the reservoir the gas flow is humidified and then mixed with the dry bypass gas. The reservoir is depicted with a short bypass explained below.
Humidity is tuned via the distribution of the gas flow by the two valves (green). Two Vaisalas (1 and 2 in orange) monitor the reservoir and mixing humidities. Vaisala 3 was only used during development and then removed due to the fresh gas having a stable humidity below 100ppm.

Humidity is measured with Vaisala dew point sensors. One Vaisala is positioned behind the mixing point to observe the water portion leaving the humidifier and entering the SM2 module. A second Vaisala behind the reservoir is used for monitoring changes in the wet path.

The distribution of the gas flow is achieved and controlled by using two valves directly after splitting the gas flow. It is necessary to have two valves to force the airflow through the wet path and to set a flow ratio between both paths. The flow rate of the gas could be used as another tunable factor. However, the flow is normally set to 15 l/h for CRF measurements and all adjustments and measurements beyond the prototype were done at that rate. Notably the positioning of the valve in the wet path is important. By placing the valve in front of the reservoir, unwanted water build-up is avoided.
The valve in the reservoir path is adjusted to a static position and then secured in that setting, yielding a baseline for adjustment. It is therefore called the *static valve* (green). Tuning of the water portion in the gas-flow is done via the tunable valve in the bypass path.

3.1.2 Development

Tubing: The high humidification in the wet path needs to be balanced by the bypass path. To keep the pure gas as arid as possible this path should be made as short as possible. Back diffusion of water vapor into the tubes depends on the length of the tubing (see fig. 3.3). This test used three Vaisalas over a length of 4.3 m soft FESTO tubing. Both tubing segments in this test (from Vaisala 0 to 1 and from 1 to 2) were of equal length and the gas flow set to 5 l/h.
Vaisala 1 measures the water vapor content after 2.15 m of tubing and Vaisala 2 after 4.3 m respectively. Thus, the saturation water vapor stays at higher levels along the tubing, representing the water vapor diffusion through the walls of the plastic tube. At the tested total length of 4.3 m, the humidity scales directly with the length of tubing (see fig. 3.3). From the first Vaisala to the last, the humdity increases from roughly 300 over 750 to 1300 ppm (see fig. 3.3, at 03-09h). This linear increase with the tubing length should end when approaching humidity levels near the environmental humidity, but was not investigated further.
Note that the response times at the beginning of the curves are retarded accordingly. Thus Vaisala 0 reaches its equilibrium in the shortest time and Vaisala 2 takes the longest to dry.

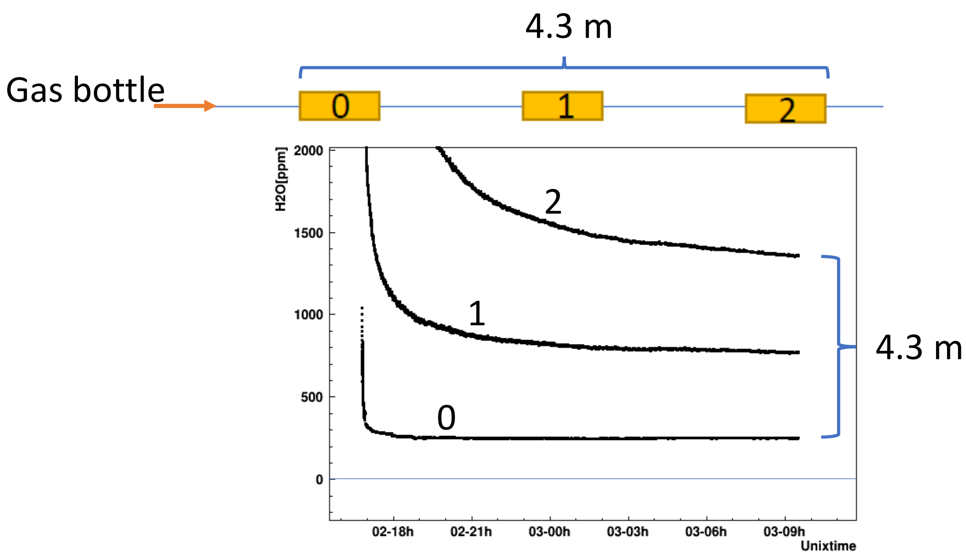

Figure 3.3: Impact of the length of soft (see Appendix) (FESTO) tubing. Three Vaisala sensors (orange) were arranged in a row along tubing of 4.3 m total length, with an end-bubbler behind the last one. The distances between Vaisala 0 and 1 is the same as from Vaisala 1 to 2. For a gas flow of 5 l/h the humidity ranges from 300 ppm for the first position, to 750 ppm for the central and 1300 ppm for the last position (at 03-09h). The gain in humidity scales directly with the tubing length.

Additionally, the difference for using hard tubing material was tested. Fig. 3.4 shows the effect of exchanging FESTO soft tubing (material: TPE-U(PU)) of 4.3 m length with equally long hard FESTO tubing (material: polyethylene (PE)). The setup is similar to fig. 3.3, albeit without the central Vaisala 1, as that one was used to monitor the environemntal humdity. The lower graph shows the humidity of the fresh gas at Vaisala 0. The upper graph in fig. 3.4 shows the humdity at the end of the tubing. Behind the last measuring position an end-bubbler is placed.

The drying process inside the tubing happens a lot faster, as depicted by the sudden fall of the upper humidity graph. Prior to the exchange the segment of hard tubing lied open in surrounding humidity of roughly 13,000 ppm (as indicated by the thin spike in fig. 3.4 at the moment of switching).
The drying process also reached lower humidties with a stable 130 ppm after a few minutes. In an earlier measurement, the soft tubing reached levels of 360 ppm for a gas flow of 15 l/h over the same length. This shows that perfusion for the hard polyethylene tubing is significantly lower.

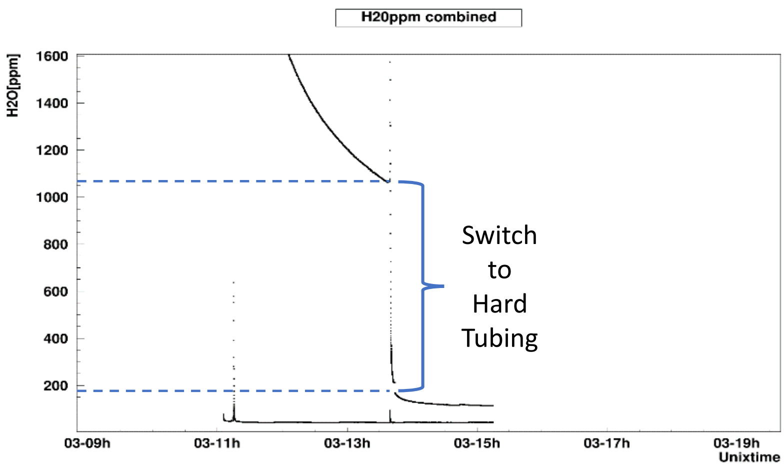

Figure 3.4: Depicted are two graphs showing the humidity as a function of time at two pistions with 4.3 m of tubing between them. The lower graph is sitting at 50 ppm and is measured by Vaisala 0 in fig. 3.3. The upper graph refers to Vaisala 2. The measurement was taken at 15 l/h with an end-bubbler behind the second Vaisala. Manually switching the FESTO tubing from soft TPE-U(PU) to hard (PE) material of equal length, immediately decreases the humidity in the system from over 1000 to 200 ppm within seconds. Afterwards the humidity decreases further to 130 ppm. By comparison the humidity in soft tubing dropped from 1400 ppm to 350 ppm at 4.3 m after min. The environment had a humdity of roughly 13,000 ppm or about 50% RH at 22° C.

Blower and Bubbler: The original concept used a so-called Bubbler as a simple way to humidify gas by pumping it through the water in the reservoir (see fig. 3.5 left pictogram). Bubblers are commonly used as End-Bubblers behind gas detectors to build up overpressure in the confined gasvolume - i.e. the gas detector. The over-pressure is dependent on the

depth of the insertion of the gas tubing into the water-reservoir.
Because of the overpressure in the path with the Bubbler-reservoir, no valve would be needed on this path. The pressure cannot be adjusted and is sharply defined, which makes manual adjustments difficult. Using a bubbler for humidification leaves the gas in the wet-path close to saturated. The target-humidity of 4000 ppm could not be reached by mixing with the dry bypass-path due to the high portions in the wet-path.

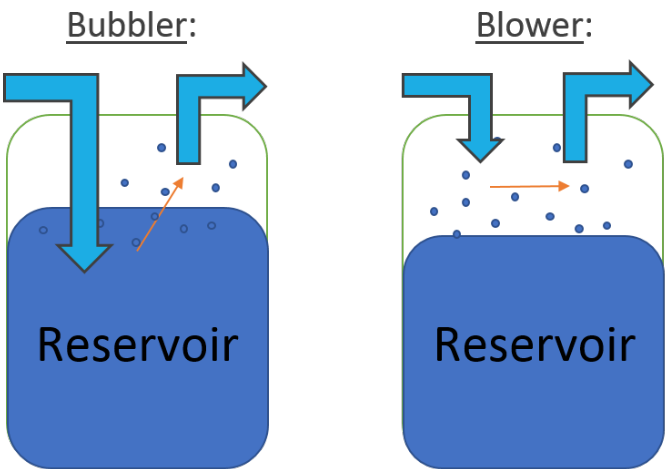

Figure 3.5: A Bubbler pumps gas into a water reservoir humidifying the gas in the proces. A Blower picks up water-portions from the vapor above the reservoir.

A Blower leads the gas-flow into a confined volume containing the water reservoir (see fig. 3.5 right pictogram). The gas flow picks up small water-portions being forced through the volume, without the pressure increase of a water-column. This necessitates tunable valves in both the dry and wet-paths to set the desired ratio for the gas flow.
The Blower humidifies consistantly with water-portions around 20kppm. As this configuration is tunable, it reaches low enough mixing-humidites. It is however affected by changes in surrounding temperature and air-pressure and the setting of the valves is delicate.

Small Bypass: The prototype as described was hard to adjust manually as it demanded very different settings for the valves. This proved detrimental at the low flow rates of the facility as the tunable valve (see fig. 3.2) tended to close up during prolonged measurements, resulting in unstable humidification. The time frame until closure is strongly dependent on the valve settings and their divergency. The best results were observed at similar valve settings as described in the following paragraphs.

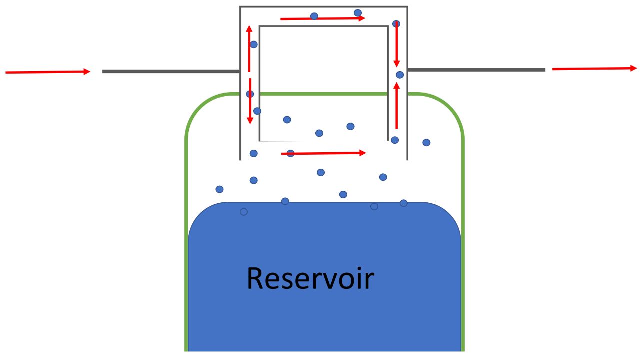

Figure 3.6: A short bypass on top of the reservoir reduces the amount of water picked up by the gas flow. This allows to lower the water portions in the wet-path to 16kppm.

Therefore, a second bypass was introduced around the reservoir to reduce the humidification within the reservoir path and to allow for more equal gas flows in both paths (see fig. 3.6). This resulted in lower reservoir humidities and more stable mixing-water-portions. This improved manual tunability as the tunable valve could be adjusted within a wider range with flows being less different between the two paths.

FESTO soft tubing was used for the reservoir-bypass, due to its flexibility. This allowed for the reservoir-bypass to be more compact.
Note that a bypass at the reservoir is only possible in the Blower configuration, as the gas flow would bypass a Bubbler completely.

3.1.3 Performance and Limitations

The humidifier could be manually adjusted to a desired water-portion with a precision of less then 10 ppm (see fig. 3.7a). Due to daily changes in temperature and air-pressure in the CRF the humidity at the SM2 gas-inlet could vary by ca. 400 ppm. In periods of constant weather the humidification is sufficently constant (see fig. 3.7b).
Dynamic valves reacting to the Vaisala-outputs could improve the stability significantly if desired.

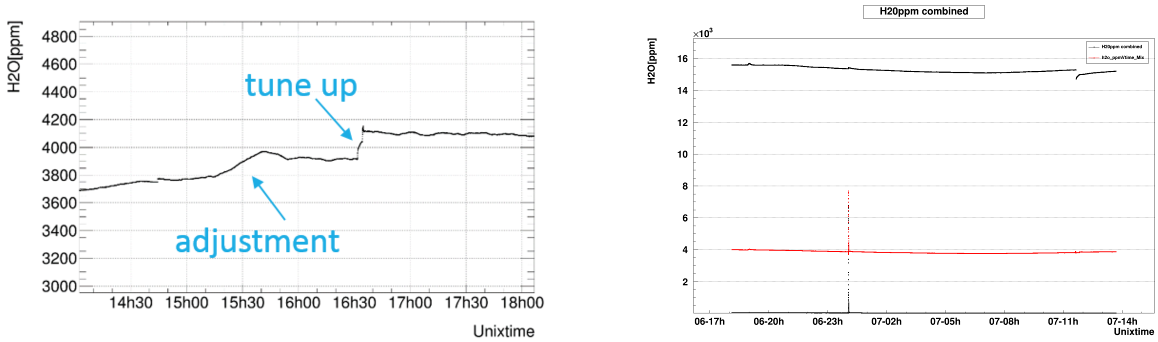

(a) Module dryingtime (b) Humidity equilibrium

Figure 3.7: (a) To set the desired mixing humidity, the static valve is adjusted to set the baseline humidity and the dynamic valve to tune the mixing ratio. (b) A level mixing humidity (red) can be held for 19 h.

Tunability comes at the price of a pressure increase in front of the valves at the gas system. The increase in front pressure was limited to less then 100 mbar during measurements to limit aberrations from normal conditions and to avoid damage - though as the gas system is designed for an overpressure of 3 bar and the module operated at 1 bar, an increase of a few hundred mbar does not pose a threat for the system.

3.2 Measurements

The humidifier was installed at the CRF on the movable sledge. This allowed the exchange of modules without any additional steps and kept the humdifier reachable from the backside once the sledge was driven in.
Measurements were taken over a period of two month, july and august 2020. The temperature at the module, environemtal humditiy and the inlet and outlet humdities were recorded.
Gas flowrates were kept at 15 l/h. The pressure in the gas system leading to the humidifier and supplying the module was checked regularly. This was a precautionary practice, as the valves used originally tended to lock up after gas outages which led to increased pressures in the gas system. A defect of the humidifier can be detected by an increase in the gas-system pressure and a change of the Vaisala output at the reservoir.

Measurements were taken with and without the humidifer connected to the module to obtain the drying times of a humid module. During all measurements, data for HV-levels and currents were recorded as is standard for modules in the CRF.

3.3 Observations

This section describes the observed behaviour of the SM2. The findings are grouped into two categories. The first category covers how the module adapts to changes in the gas flow and gas humidity. Afterwards the HV behaviour of an extensively humidified module is described.

3.3.1 Attenuated Adaptation to induced Humidity

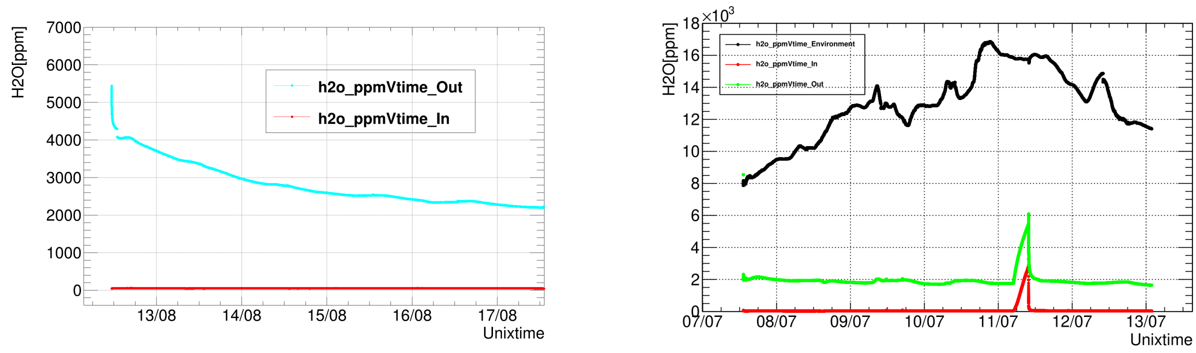

(a) Module dryingtime (b) Humidity equilibrium

Figure 3.8: (a) Decrease of the humidity over time measured at the SM2 gas-outlet (blue). The inlet humidity (red) is at roughly 100ppm. Recorded mid august. (b) A dry module stays at roughly 2000ppm outlet-humidity (green) and is hardly impacted by environmental humdity (black). The spike marks an outage in the gas system. Recorded early july.

As was already known from the construction and operation of modules, drying a module by flushing it with gas takes several days (four days in fig. 3.8a). This is expected as several components of the module can absorb and store small portions of water. Additionally the many components of the module offer manifold opportunity for water to accumulate at edges, folds and between surfaces.

The adaptation of the SM2 to changes in the working gas is delayed. Inducing humidity to a module that was previously in a drying process, will not immediately show a change at the outlet. It can take up to 6 hours until the outlet-humidity stops decreasing and increases (see fig. 3.9b after the two-days drying period).
Drying a humid module sees a faster response time of the outlet with a delay of ca. two hours until a decrease in humidity sets in (see fig. 3.9b). *Dried out* by the relatively arid Ar:CO_2 working gas, the absorbent components (like Kapton® tape) might absorb most of the initial water-portions. This fits the observation that humid modules react faster to changes in the gas than to dry modules.
Note that an outage in the gas flow results in imediate rises both at the in- and outlets of the module, as water from the reservoir, the end-Bubbler and the environment start permeating the module instantly.

3.3.2 HV-Stability

The effect on the HV stability was observed on a test module, which was operated at the CRF for over a month starting early july. To evaluate the changes in behaviour, two measurements are compared. The first measurement was done with the module freshly installed in early july. The second measurment started around the beginning of august after the module was operated under humidification for about a month. Both measurements were done at a stable gas flow of 15 l/h.

Initially, the freshly installed module was thoroughly dried by the Ar:CO_2 gas until a humdity level around 2000 ppm was held for several days (see fig. 3.9a). The first HV was taken from july 7th to 10th in a dry state.
After that the module was humidified constantly, in part in a controlled manner using the humidifier, as well as passively during gas outages occuring late july. During gas outages, the SM2 absorbs humidity through its surface from the environment, as well as from the humidifier reservoir and end-bubbler along the inlet and outlet tubing. After three weeks of repeated humidification, the secong HV measurement began on july 29th.
The humidity during the second measurement is depicted in fig. 3.9b. The module was connected to the humidifier for two parts of this measurement and flushed once with pure Ar:CO_2 between the humidification periods.

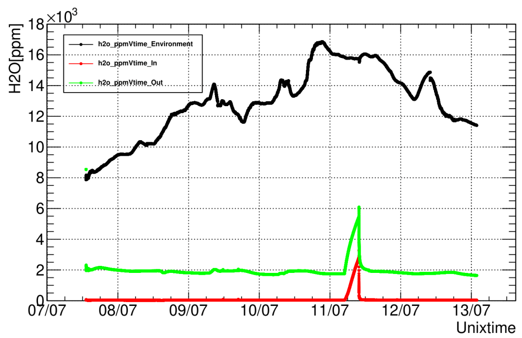

(a) module M28 drying period july

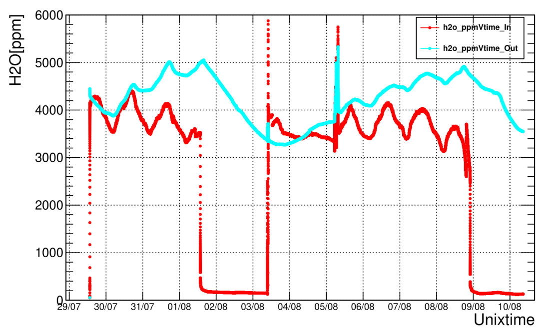

(b) module M28 wet period august

Figure 3.9: Humidity measurements for the module M28 at the CRF. (a) Measurement from july 7th to 13th: Pure Ar:CO_2 gas was used, resulting in a dry module during at an inlet-humidity (red) of roughly 80 ppm and an outlet-humdity (green) of 2000 ppm. The Environmental humidity (black) shows no significant impact on the module during un-humidified operation. The spike denotes a gas-outage and vanishes immediately after the restart of the gas-system. (b) Humidification of the SM2 module M XY from july 29th to august 10th. Graphs for induced (red) and outlet-humidity (blue). Sudden change in the incoming humidity denote the removal (august 1st around noon) and implementation (august 3rd around noon) of the humidifier. The removal is followed by a decrease in outlet humidity after two hours. It takes six hours until the outlet humidity begins increasing after the humidifier is reconnected.

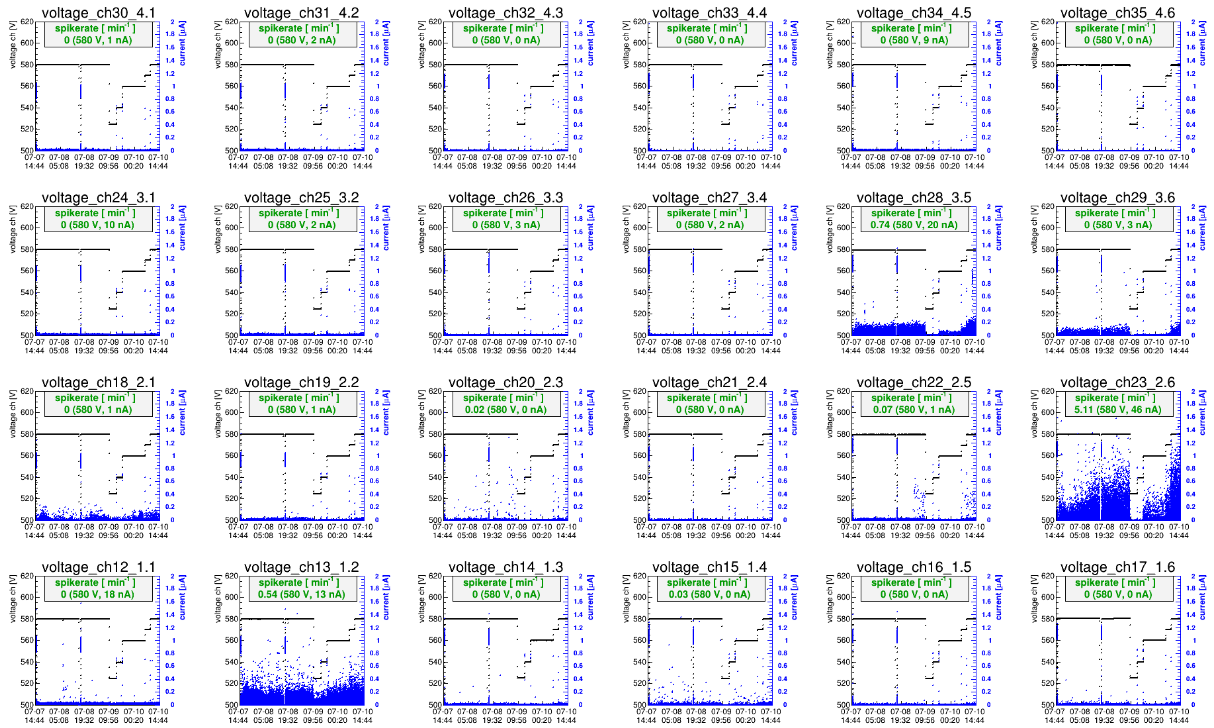

Figure 3.10: Initial HV measurements from july 7th to 10th (horizontal axis) for a module freshly installed at the CRF. Five channels show considerable currents (blue): Channels 1.2, 2.1, 2.6, 3.5 and 3.6. The other 19 channels showed only occasional currents. The voltage (black) was stable. The step-like voltage levels (starting july 9th) are part of the testing procedure of newly inserted modules at the CRF.
Pure Ar:CO_2 gas was used during the measurement, resulting in a dry module at an inlet-humidity of roughly 80 ppm and an outlet-humdity of 2000 ppm (fig. 3.9a).

Ideally the module holds a stable voltage of 580 V and does not draw currents during operation. Fig. 3.10 shows the behaviour of the module after being installed in the CRF and at a stable 2000 ppm outlet-humidity. Only five critical sectors were observed in the dry measurement (fig. 3.10: Channels 1.2, 2.1, 2.6, 3.5 and 3.6), as well occasional currents in the other channels. The voltages of each channel were stable at 580 V during the first two days of testing and showed no defects during the following testing procedure (step-like increases in voltage levels), which is performed during measurements for every module in the CRF.

Fig. 3.11 shows the SM2 HV plots with the measurment starting on july 29th. Depicted are the voltage (black) and currents (blue) over time (horizontal axis). The water vapor content was about 4000 ppm. All 24 HV sectors of the module were operated at 580 V (black lines) and able to hold a stable voltage. Five channels (1.3, 2.5, 3.3, 3.5 and 4.6) showed small fluctuations of a few volts. Apparently the humidity did not directly impide the capability of the module to reach and hold its operating voltage. However, the humid module showed severe currents in most sectors. Only sectors 3 and 4 in layer three and 3 to 6 in layer four showed no currents, while sector 3.1 showed small currents. The other 17

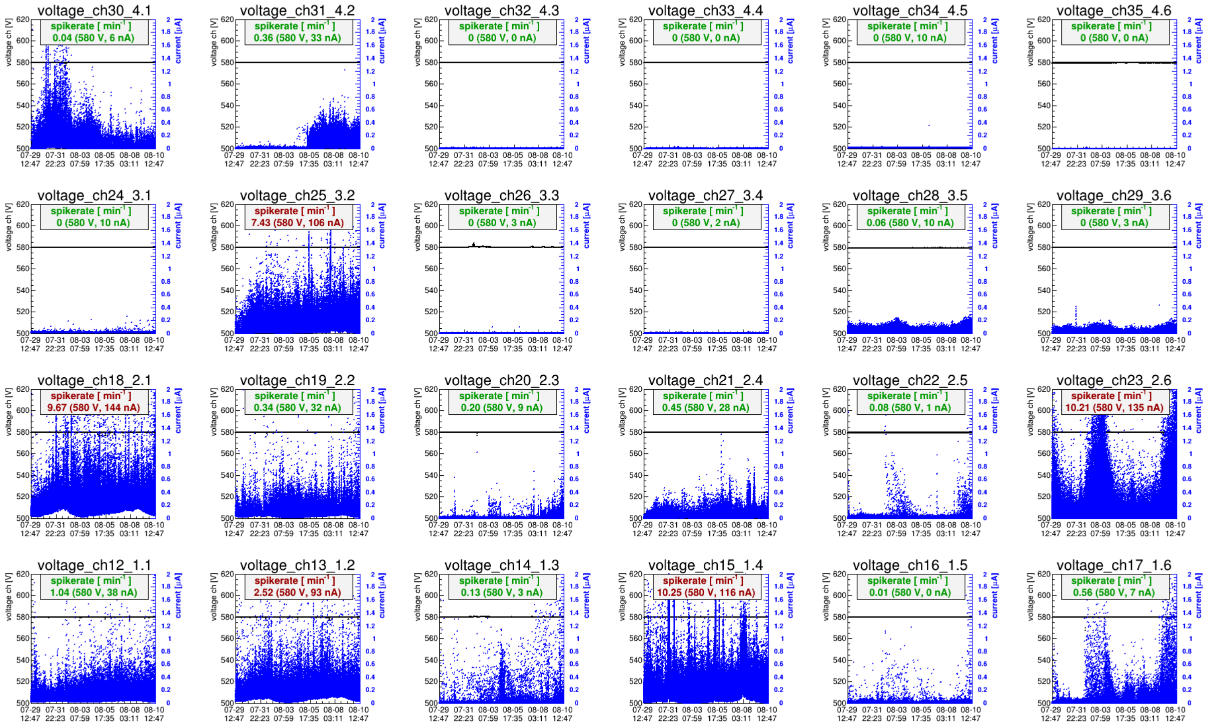

Figure 3.11: HV plot for the time from july 29th to august 10th (horizontal axis). The voltage held by each are depicted in black, currents in blue. Red labels mark sectors which exceeded a set threshold. This module was humidified for roughly a month. By the end it showed only small voltage fluctuations of a few volts in five sectors, with the highest fluctuation in sector 3.3 (the third sector of layer three). However, 17 sectors showed severe currents. Ideally the voltage is constant and no currents flow.

channels showed currents of different severities, with five channels (1.2, 1.4, 2.1, 2.6, 3.2) exceeding the allowed limit. By comparing the dry measurement (fig. 3.10) and humidified measurement (fig. 3.11), the development of the module under humidifcation is observed: Over the month the two channels 3.5 and 3.6 did not change significantly. Channels 1.2, 2.1 and 2.6 worsened and twelve channels started drawing currents. Prolonged humidification with 4000 ppm water in the Ar:CO_2 working gas of the SM2 module resulted in running currents in several sectors. Only seven out of 24 channels showed no or low currents (channels 3 to 6 in layer four and channels 1, 3 and 4 in layer three). Channel 3.1 showed a small increase in currents. Keeping the module at humidity-levels between 4000 and 5000 ppm proved to be detrimental. In general the channels' discharge rates worsened with time. The short drying period did not restore the HV stability in any way.

This experiment proved water-pollutions in the working gas create detrimental effects in the SM2 module. For prolonged humidifaction the amount of discharges increased. These threaten to cause damage to the detector, aside from reducing its efficiency. Humidification of the module showed none of the positive effects reported from other detector systems. Hence humidity in the working gas should be avoided.

Chapter 4

Neutron Background Studies

The evaluation of the performance of the SM2 module under background radiation is part of the ongoing investigation and development of the modules. The approach is based on the recent works of (Herrmann, 2019), (Flierl, 2018) and (Klitzner, 2019).

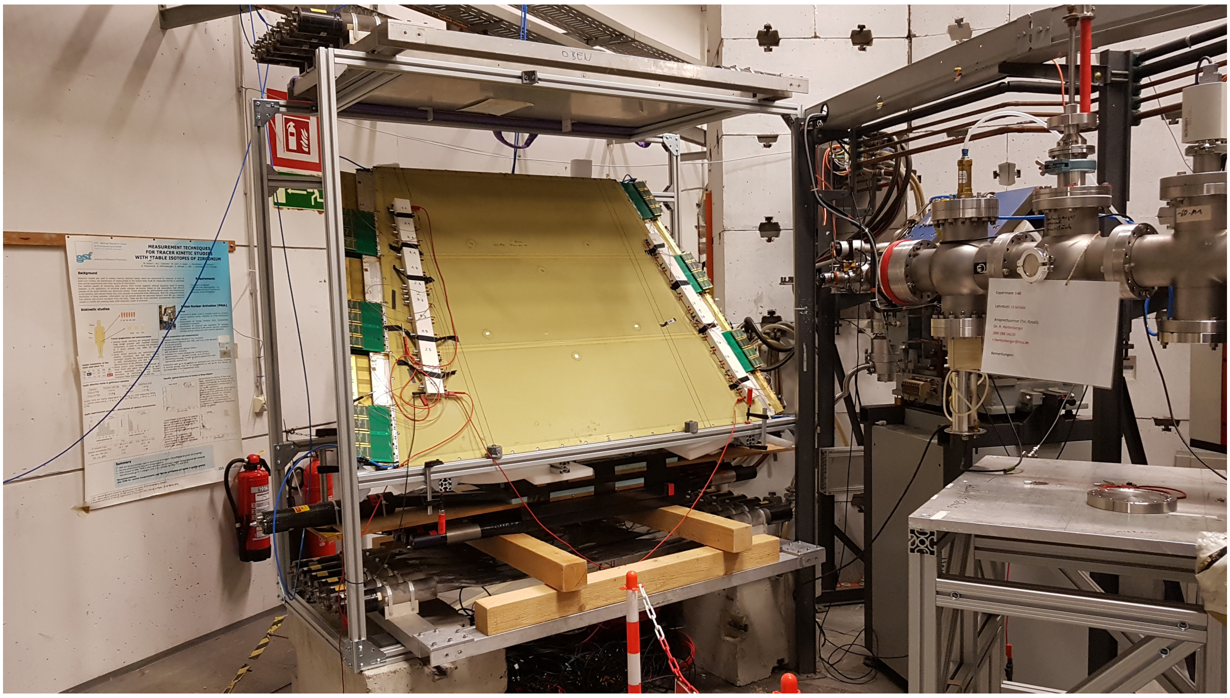

Figure 4.1: SM2 module *M3* at the tandem-accelerator. The module is set up at an angle of 60° to the horizontal plane and is irradiated by neutrons. The setup results in a mean inclination for cosmic muons of 60° against the precision axis of the module. To create the neutron background, a beryllium target is hit by the horizontal deuterium beam from the accelerator. The module is sandwiched between six layers of plastic scintillators connected to Photo Multiplier Tubes, which trigger on the cosmic muons and allow for reconstruction of their tracks as reference.

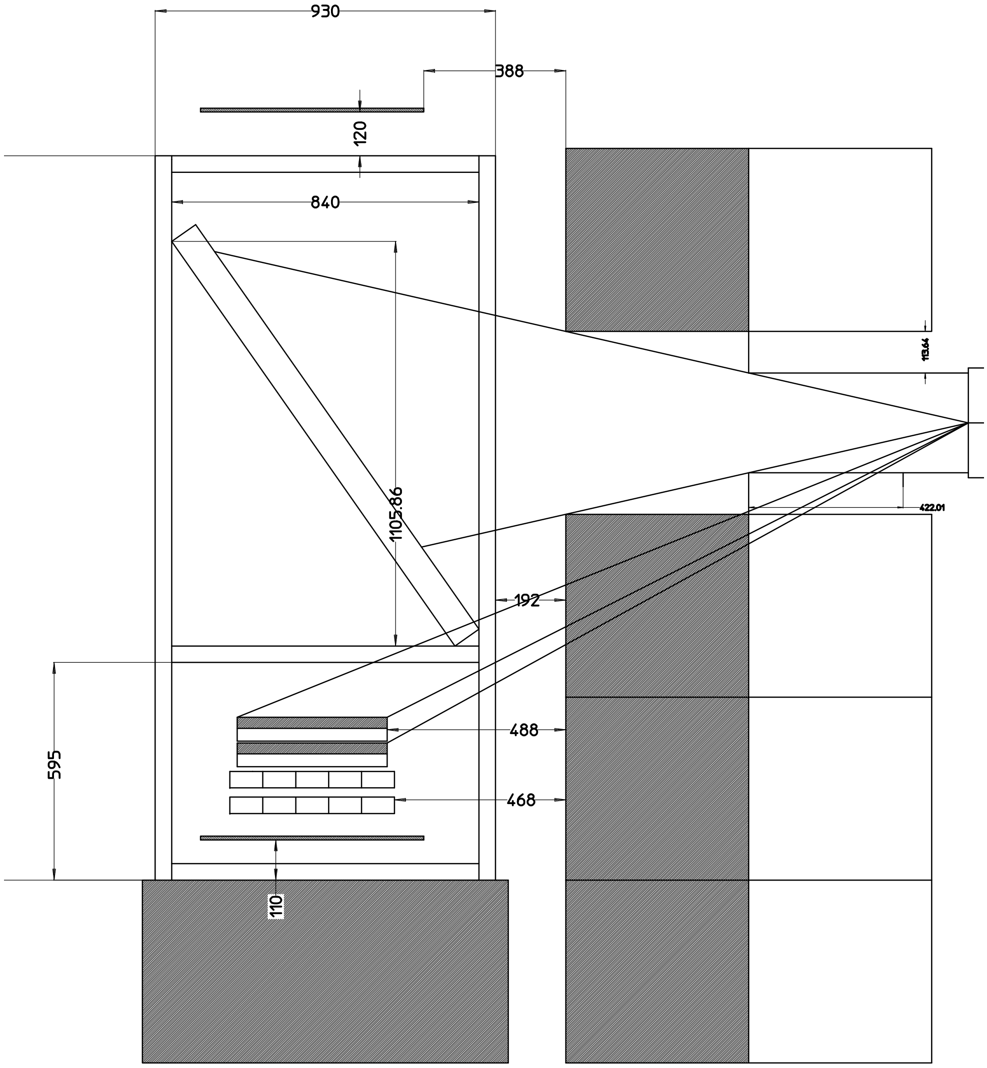

Figure 4.2: Schematic of the tandem experiment. The SM2 module *M3* is set up at an angle of 60°, such that the neutron beam irradiates most of the module surface. Plastic scintillators are used to trigger on cosmic muons and encompass the irradiated portion of the module. Concrete blocks (black squares) obscure the trigger scintillators from direct irradiation. See fig. 4.3a for a simplified schematic.

4.1 Experimental Setup

Due to its planned application at ATLAS the SM2 will be exposed to a significiant radiation background during operation. To probe the module performance under background an experiment was conducted at the tandem-accelerator in Garching (see fig. 4.1 , fig. 4.2 and fig. 4.3a).

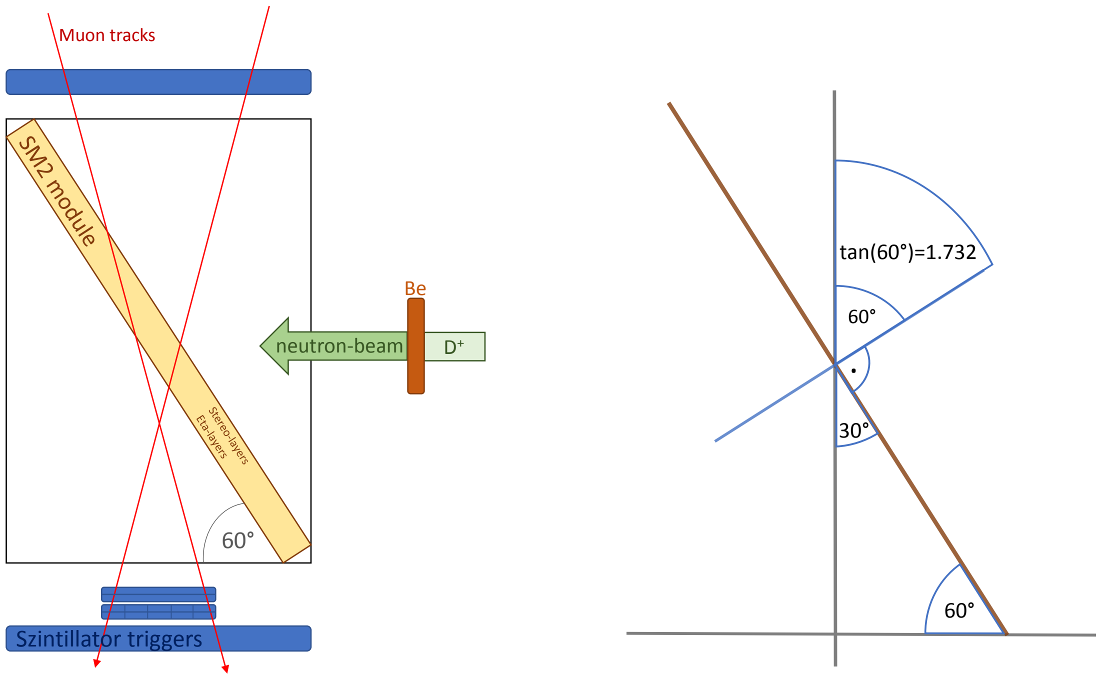

(a) Simplified schematic of the experiment

(b) Mean angle of muon-incidence

Figure 4.3: (a) Schematic of the setup of the tandem-experiment. The module (yellow) is setup at a 60° angle. For triggers six layers of scintillator tubes (blue) encompass the module. The triggers detect passing muons (red) and trigger the recording of the event. The module is irradiated by a neutron beam generated from deuterium (D^+) breakup (green) on a beryllium target (brown).
(b) The average muon inclination is assumed to be perpendicular to the ground. The module is made from four prallalel layers through which the inclination can be calculated. A zero inclination for the SM2 is defined perpendicular to the module. The expected mean inclination measured should be 60°.

The SM2 module M3 was set up at a 60 degree angle against the horizontal plane with the short edge facing upwards (see fig. 4.1 and fig. 4.3b). The module was oriented such that the Outer Stereo layer (SO) faced the neutron-beam. Six plastic scintillator layers were placed encompassing the module, one above and five below the module (blue fig. 4.3a), to trigger on traversing cosmic muons (red fig. 4.3a). Each scintillator is connected to one or two Photo Multiplier Tubes, which amplify the photon signals created in the scintillators for readout. Coincidences on these triggers cause an event to be recorded. The sixfold coincidence reduced the number of accidental coincidences induced by the intense neutron beam to a level similar to the trigger rate of cosmic muons. One third of the events are estimated to be actual muon-events with the other two thirds coinciding by chance.

Beam current I_D	neutron flux rate density	Trigger rate	Period of time
0 nA	$0\frac{n}{cm^2 s}$	0.871 Hz	Nov 01-03 h until 01-08 h
50 nA	$1.5 \cdot 10^4 \frac{n}{cm^2 s}$	1.026 Hz	Nov 02-18 h until 03-05 h
100 nA	$3 \cdot 10^4 \frac{n}{cm^2 s}$	1.805 Hz	Nov 01-08 h until 02-18 h

Table 4.1: Beam currents and the resulting trigger rates during the experiment

An ongoing neutron beam was generated from deuterium breakup (dark and light green in fig. 4.3a) on a beryllium target (brown). The deuterium energy of 20 MeV generates neutrons of 10±10 MeV. The intensity of the the beam was controlled by an applied current (I_D). Three currents were applied during the measurement: 0, 50 and 100 nA. The neutron flux-rate-density scales with the applied current. The sixfold coincidence of the trigger system resulted in a trigger rate of 1.805 Hz for the strongest neutron background and 0.871 Hz while the beam was off.

4.2 Data Analysis

The analysis of the data aims to find selection-parameters which reliably remove neutron related clusters and keep the muon clusters to form a muon-track (see fig. 4.4b). To derive these, the characteristics of the data have been analyzed by the parameters of each cluster and with a track-reconstruction method explained below.

4.2.1 Events

In two days of data taking a total of 170,273 events have been recorded and 1,567,491 clusters reconstructed. Each event consists of a number of clusters distributed over the four detector-layers (see fig. 4.4a), reconstructed from the signals collected in a timeframe of 600 ns (APV: 24 timebins of 25 ns).
To identify a muon the clusters caused by the neutron-background have to be eliminated. The majority of muons passes the detector in straight manner, ideally creating a track of four clusters. Neutrons interact mostly in one layer only (if at all) and do not create tracks. The analysis of the data aims to find selection-parameters which reliably reduce the clusters of the event to form a muon-track (see fig. 4.4b).
Each cluster has several parameters: Centroid, timing, charge (see chapter 2), size and

μTPC-slope (explained in section 4.3.3). Some of these proved to be potent selection-parameters. They will be discussed later.

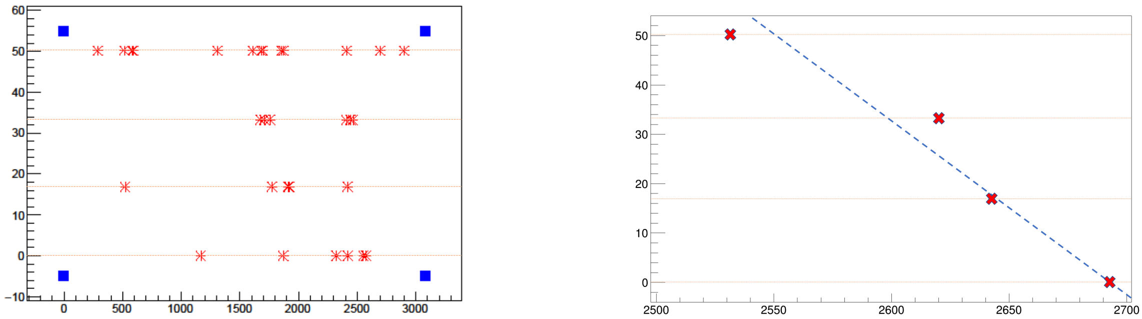

(a) Event display of raw data

(b) Selected clusters for muon-track

Figure 4.4: Event displays without (a) and with (b) filtering: The horizontal axis represents the position along the precision-coordinate of the detector in strip number. The vertical axis is given in mm and correlates to the layers of the detector, represented by the orange horizontal lines. The red markings on each layer are clusters recorded for the event. Two different events are shown, to give tangible impressions of the potential number of clusters in an event (a) and of a reconstructed track (b).
(a) This display shows the positions of all clusters recorded during an event. The four blue squares are visual aids and represent the confinements of the detector in the precision direction. (b) By application of derived filter-parameters the number of clusters can be reduced and muon tracks reconstructed. The muon-track is indicated by the blue line.

4.2.2 Track Reconstruction for Data Analysis

The analysis of the events builds on track-reconstruction via the *Residual* method. This broad data analysis aims to examine the events for characteristics, which can then be used to select muon clusters. This method will also be referred to as (*initial*) *data analysis* from chapter 4.3.4 onwards, which uses a similar method based on the cuts derived from the data analysis.
To reconstruct the most-likely track of an event, all possible combinations of event clusters are iterated. Figure 4.5a illustrates one iteration.

Beginning with the two stereo-layers, one cluster from each layer is chosen. The centroid-parameter denotes the position of each cluster as a strip number. From those two clusters a virtual cluster (red) is generated using eq. 4.1. The centroid-values of the SO and SI clusters are inserted for u and v. Each stereo layer is tilted by an angle α of ± 1.5 degrees compared to the eta layers. The virtual stereo-cluster is placed at the calculated position along the precision (P) direction and between the two stereo-layers along the z-axis of the module.
At this point in the iteration the position along the non-precision (NP) direction can be calculated using eq. 4.3. Note that the NP direction of the module is defined along the strips and perpendicular to the P direction. In relation to the map-plots (fig. 4.13), the

precision direction is also referred to using 'y' and the non-precision direction using 'x'.
Next an EO-cluster (purple) is chosen. A track through this cluster and the virtual stereo cluster is formed. At this point the trackslope can be calculated.
Finally the intersection-point of the track with the EI layer is calculated and compared to the clusters in this layer (yellow). The residual is defined as the distance between the track intersection and the cluster centroid (Figure 4.5b). The combination of clusters forming the smallest residual is chosen as a final track.

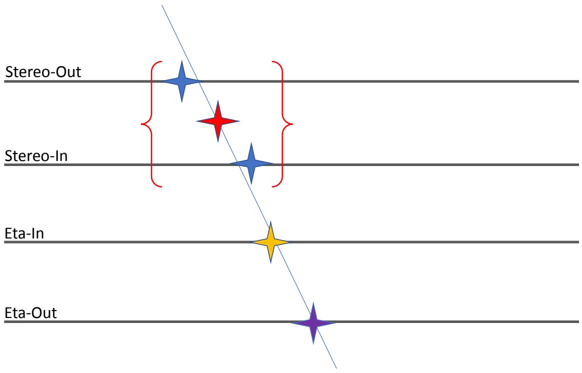

(a) Track Reconstruction

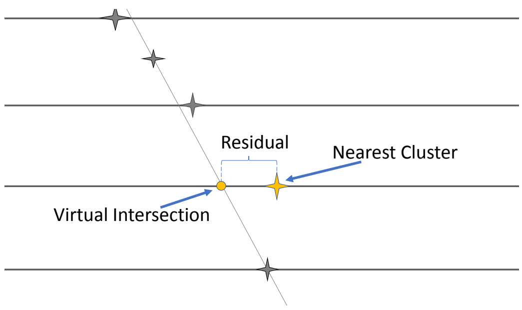

(b) Residual Definition

Figure 4.5: (a) Schematic of the track-reconstruction method depicted for four arbitrary clusters. A virtual Stereo-cluster (red) and an EO-cluster (purple) form the track, which is then probed against an EI-cluster (yellow). (b) Schematic of the definition of the residual as the distance of the nearest cluster from the virtual intersection of the track with the EI layer.

The iteration is done by four loops nested into one antoher, starting with the outermost loop over all SI-clusters. For each one, the loop includes all SO clusters so that each combination form a corresponding virtual stereo-cluster. The next inner loop iterates through all EO clusters to form tracks for the current combination of clusters from SO and SI. The innermost loop calculates the residuals for all EI clusters for the current SI-SO-EO combination.
This way all combinations of clusters for the event are calculated and the one combination with the smallest residual is selected.

4.3 Cluster Selection Parameters

Ideally all clusters used for track reconstruction of any given event, are caused exclusively by traversing muon particles. To this end, a selection-process is needed to seperate muon-clusters from background-clusters (see fig. 4.4 a). Through deliberately chosen cuts unsuitable clusters can be neglected during the track reconstruction. These cuts can be sorted into two categories: Cluster parameters and setup-properties. Cluster parameters

are properties of the clusters themselves, like the charge or the size of the cluster. Additionally, properties of the setup can be used to discriminate tracks.
Note that the appearance of cluster parameters can be dependent on the setup, too. In particular the timing of a given cluster, which is measured relative to the trigger signal, is dependent on distances as well as the readout logic and electronics of the experimental setup.

A single cut could not be found, which on its own would select muon-only clusters. Therefore the goal was to identify cuts, which in conjunction select muons as reliable as possible by addressing distinct characteristics.

4.3.1 Comparison with CRF-Data

The CRF pure-muon data is used for comparison with the data recorded at the tandem experiment. To verify that the track-reconstruction and data analysis worked, the algorithm was tested on data recorded at the CRF with the identical module used at the tandem. This was done to reduce module-specific effects. Unfortunately the readout electronics were not the same during the measurements.
The information extracted from the comparison of the CRF-data and the tandem-data will be presented in the following sections together with their application in the analysis of the experiment.

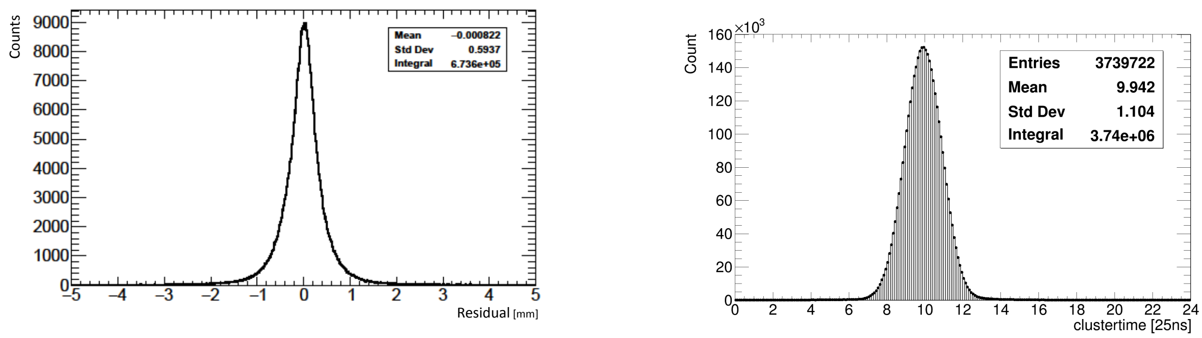

(a) CRF: Track residual

(b) CRF: Clustertime

Figure 4.6: The pure muon data of the CRF reveal distinct characteristics without the application of cuts. (a) Residual for the CRF-data. The width of track residuals is dependent on the track-inclinations. Due to the mean normal inclination and limited range of inclinations present at the CRF, the resulting residual is well definded and has a small width.
(b) Depiction of the timing of all clusters recorded. The timing of all clusters is evenly distributed around the peak. The distribution has a total width of 6 timebins.

The CRF data was analyzed without the application of cuts and with the adjustment of zero inclination - i.e. a horizontal module. The method of track-finding by minimizing the residual (as explained above) reconstructs the majority of tracks correctly. The analysis shows a distinct and even distribution of the residual and the timing (see fig. 4.6)

aggreeing with the work of (Herrmann, 2019).
Note that the symmetrical correlation is a result of the module lying horizontally. Under tilted inclinations the shape of this correlation is deformed diagonally. The positions of the virtual stereo clusters (formed from a pair of clusters in the stereo layers) recreates the shape of the modules (see fig. 4.8 a). This can be attributed to the high number of pure muon-events at the CRF during the extended measurement-times and low noise. However 1.3% of events were falsely reconstructed outside the active area of the module, as the application of a simple geometric cut on the active surface shows (see fig. 4.8 b).

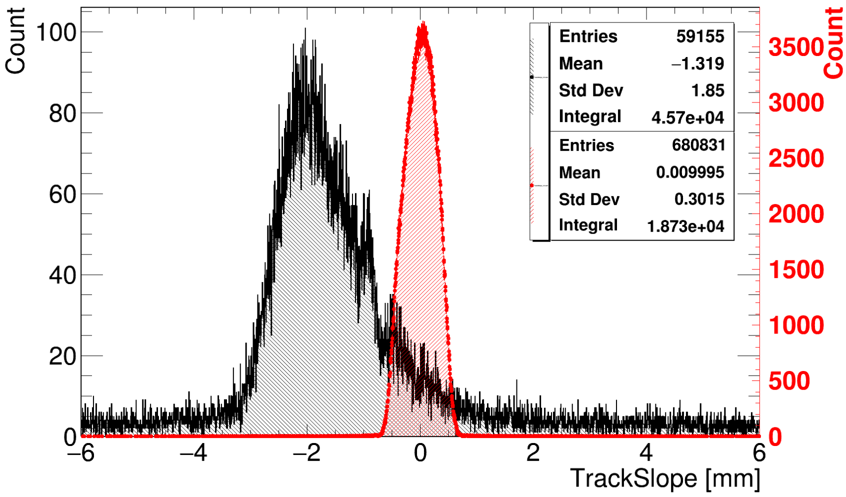

Figure 4.7: Slopes at the CRF are equally distributed around zero-inclination (red). By comparison the tracks reconstructed for uncut tandem-tracks (black) show a bias towards a slope of -2, corresponding to the 60 ° inclination. Positive slopes are impossible for cosmic muons, as those do not pass the trigger scintillators.

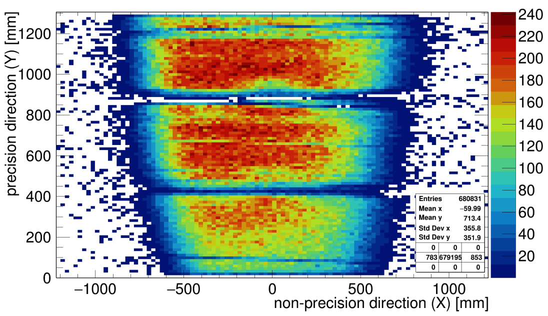

(a) CRF map raw

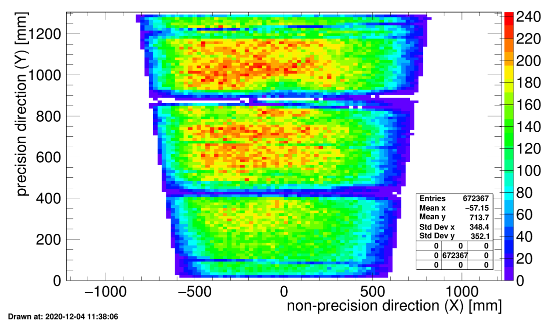

(b) CRF map cut

Figure 4.8: (a) Positions of virtual stereo-clusters which were part of reconstructed tracks without the application of cuts. Note that a small margin is reconstructed outside the active area. (b) By restriction to the active area 1.3 % of entries are lost.

4.3.2 Chosen Cut-Parameters

In this section the parameters are investigated, which are applied to seperate muon and neutron-clusters. Cuts were chosen according to characteristics of muons and the experiment. The cut with the highest impact was the selection of the cluster-timing and was applied generally on all clusters by the algorithm.
The second cut applied only to clusters in the stereo-layers by only allowing combinations of those which were located inside the active area.
The final selection-parameter was the slope of the reconstructed track.

Additionally, two more necessary selections were implemented to eliminate noisy channels and times of unsteady irradiation by the accelerator. The cut of rate-fluctuations of the accelerator is discussed in the results-section due to the connection to the efficiency.

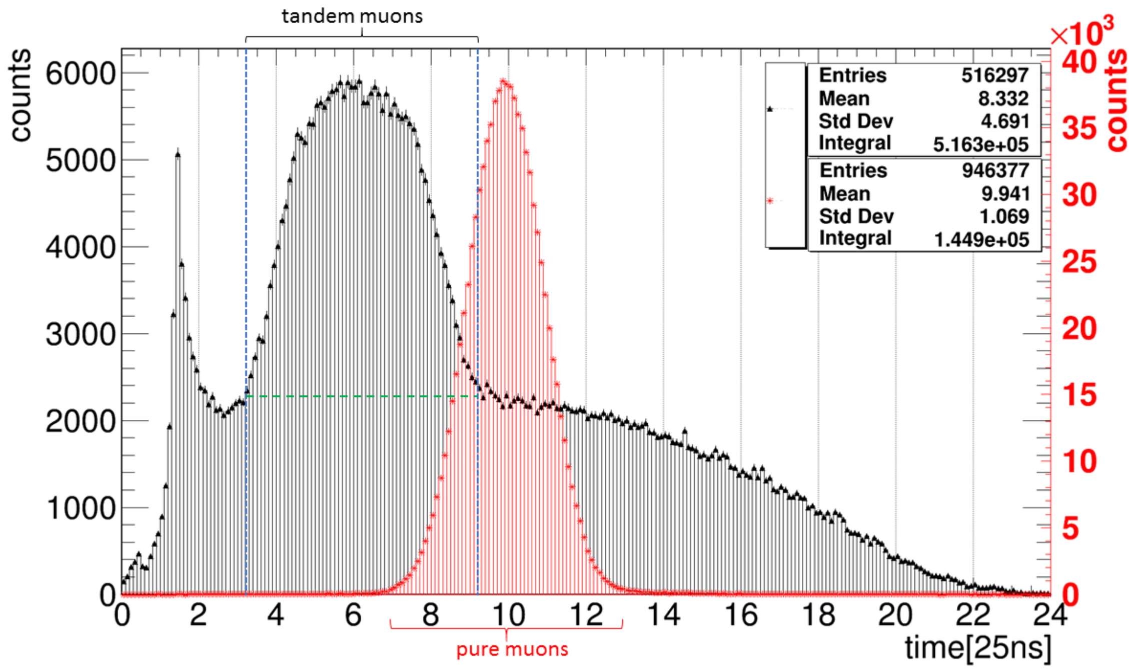

Figure 4.9: Comparison of the timing-parameter for EI clusters from the tandem data (black) with pure muon clusters from the CRF data (red). The distribution of the CRF data ranges from timebin 7 to 13, the tandem peak from timebin 3 to 9. Both peaks have a width of 6 timebins (i.e. 150 ns) as a result of the maximum drift time in the 5 mm thick drift region. The neutron background within the 6 timebins is assumed homogeneously distributed (green line). The area above represents the muons in the tandem experiement. The Gaussian shape of the pure muon distribution (red) is caused by diffusion in the drift region. The peak in the tandem data has a broader, non-Gaussian shape, due to the more even activation of strips under the 60° inlination of the muons. The distinct timing of muons makes this a potent characteristic for cluster selection.

Timing - 'τ' Timing is a parameter of every single cluster and is measured relative to the trigger of an event. The timing is evaluated for every strip of the clusters individually,

with stripsignals being recorded at a 40 MHz rate. The charge weighted average of the striptimes is then assigned as the timing of the cluster. An improvement of this 25 ns resolution is achieved by a signalfit using a Fermi-like function.
To apply a timing cut, evaluation of the timing of measured clusters is necessary as the parameter is dependent on the setup and tuning of the experiment. The total width and shape of the timing distribution for muons is assumed to be equal in both the tandem data and the muon data.

The reference data taken at the CRF shows a distinct behavior for the timing for pure muons (see red curve in fig. 4.9). By contrast, the neutron background is expected to be timed almost evenly (green line), due to the constant and random background. The distribution of the timing of all clusters recorded shows a peak around timebin 6 (see black curve in fig. 4.9). The shape of the distribution is uniform across all four layers (see fig. 4.10). Note the SO-distribution has a frayed appearance due to noisy channels in that layer. The peak reveals the most common timing for muon clusters. Additionally an early sharp peak and a steady decline towards the end of the event are present. The early spike is attributed to the algorithm calculating the timing of clusters.

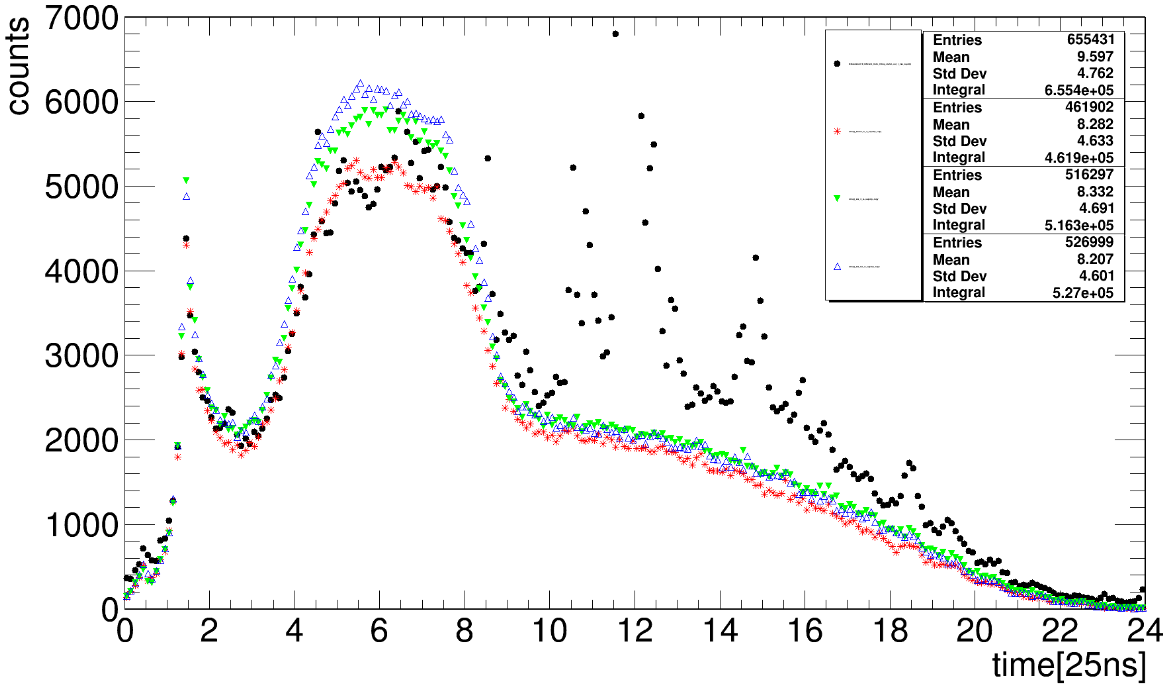

Figure 4.10: Distribution of cluster-timings for each detector-layer without selection. The peak between timebins 3 and 9 is attributed to muon clusters and is dominant in all four layers. The distribution in the SO layer (black) is less defined than in the others due to noise in the readout electronics.

The position of the peak is dependent on the physical setup of the experiment, explicitly the cable length of the triggers and the electronics and trigger-logic. As depicted in fig 4.9

(red) the curve of the CRF data shows a total width of 6 timebins around the peak close to timebin 10. The width of 6 timebins (or 150 ns) represents the maximum drift time in the 5 mm thick drift region of each layer. At the CRF muons hit the detector at zero inclination (perpendicular to the module surface). Due to diffusion in the drift region additional strips are activated, causing a Gaussian distribution of the timing.

The total width of the peak in the tandem data (black) is as well 6 timebins broad. Its substructure is broader and non-Gaussian due to the 60° inlination of the muons, as the strips are activated more evenly.
The range of +- 3 timebins is applied around the peak at bin number 6 in the tandem-data as a cut on all clusters. As a result only clusters which were recorded within this range were used for track reconstruction.
The timing cut is very distinctive, discarding every cluster with a timing outside of the 150 ns around timebin 6. On its own it is however not sufficient to select muon clusters, as a signifcant background remains within this range. Furthermore the timing cut was the only parameter intrinsic to clusters that was used for cluster-selection.

Active Detector Area - 'A': The position of the virtual stereo-cluster used for defining a track can be calculated from the two involved stereo clusters following the approach of (Flierl, 2018). The precision-coordinate (P) can be derived precisely as this coordinate is close to perpendicular to the strips. The non-precision (NP) component of an event can be coarsely reconstructed ($\mathcal{O}(mm)$) due to the tilt of $\alpha = 1.5°$ of both stereo layers compared to the eta layers (see fig. 4.11).

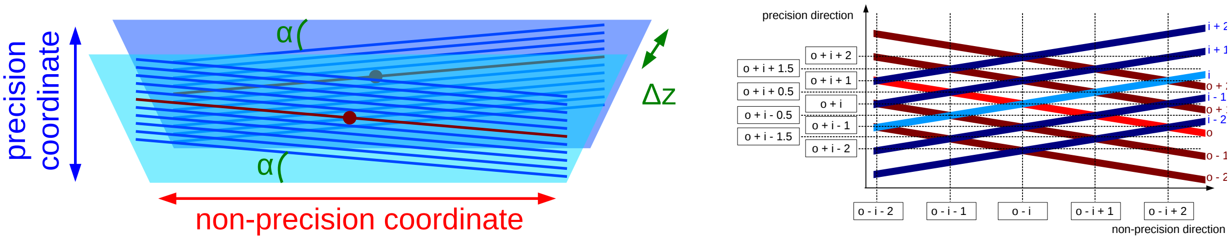

(a) Angled stereo layers (b) stereo-strip combinatoric

Figure 4.11: (a) The angle between the stereo layers allows to reconstruct the NP-coordinate of a muon point of intersection with the module. (b) The position is calculated from the difference in the strip numbers. (Herrmann, 2019)

The P-direction is defined throughout this thesis as along the y-axis eq. 4.1, the NP-direction along the x-axis eq. 4.3 of the module. The strip numbers of the SO and SI clusters are inserted in v and u respectively.
Note that the naming convention at ATLAS is different (using η for the P and ϕ for the NP directions).

$$y = \frac{v + u}{2 \cdot cos\alpha} \tag{4.1}$$

$$\Delta y = -\frac{tan\alpha}{2} \cdot \Delta z \cdot tan\Theta \cdot cos\Phi \tag{4.2}$$

$$x = \frac{v - u}{2 \cdot sin\alpha} \tag{4.3}$$

$$\Delta x = -\frac{1}{2tan\alpha} \cdot \Delta z \cdot tan\Theta \cdot sin\Phi \tag{4.4}$$

Eqs. 4.1 and 4.3 apply to inclinations of zero or if the layers of u and v share a drift region. For the 60 degree inclination in this experiment, eq. 4.3 falsely shifts the virtual stereo clusters along the x-axis by an equivalent of 1315 strips and must be corrected using eq. 4.4. The effect of the inclination on the y-axis is significantly smaller (roughly 0.38 mm $<$ 1 strip) and is corrected using eq. 4.2.
The corrections result in the correct positioning of the virtual clusters (see fig. 4.13b).
Δz = 16.9 mm marks the gap between both stereo-layers. The angles Θ and Φ are track angles given in polar-coordinates. To adapt the correction for the tandem experiment, mean assumptions for Θ and Φ were used. A mean slope of $\Theta = 60$ degrees in the P plane was assumed, corresponding to the setup of the module. Setting Θ to a mean parameter instead of dynamically applying the slope of any reconstructed track is sufficient, as the correction is miniscule compared to the value derived by eq. 4.1.
For the NP slope a mean inclination perpendicular to the module was assumed. In the experiment the only source of NP coordinates is the SM2 itself, giving only one data point in NP direction. Thus no NP inlcinations could be derived due to a lack of a second data point.

The combination of any two clusters (and their centroids respectively) would mathematically allow for positions far outside the actual area of the module (see fig. 4.12) by combining strips which strip numbers are far apart (see fig. 4.11). These combinations must be forbidden.
By applying limits taken from the dimensions of the SM2, only combinations of SO and SI clusters are allowed which can be part of one track. The result of this cut is displayed in fig. 4.13a. The shift of the spot fig. 4.13b denotes the effect of the correction terms (eqs. 4.1 and 4.3).
The precision of this cut could be improved further with information of the non-precision slope of the muon tracks.

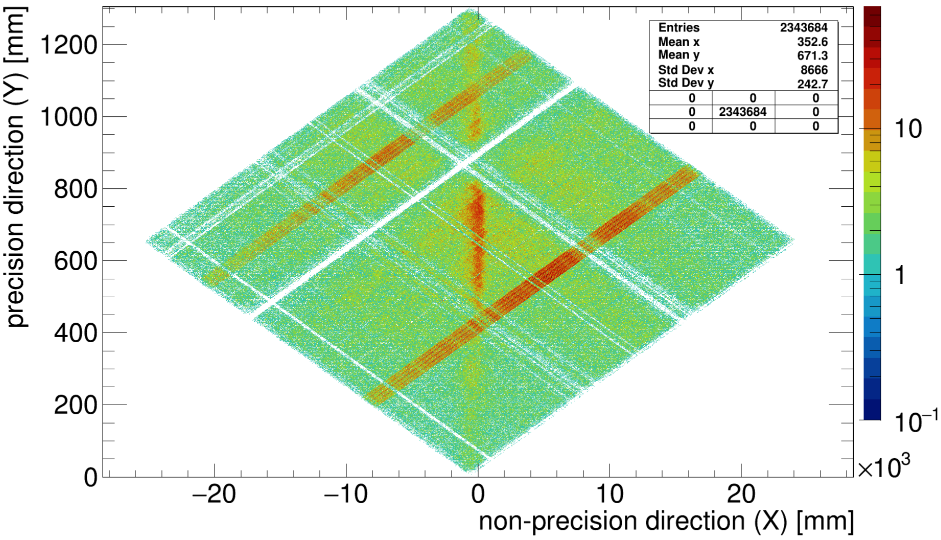

Figure 4.12: Random combinations of two clusters from two angled layers result in a rhombus-like distribution. The small angle of 3° between the stereo layers allows positions far outside the detector. The long parallel edge of an SM2 module is 1630 mm long, which relates to roughly 3800 strips.

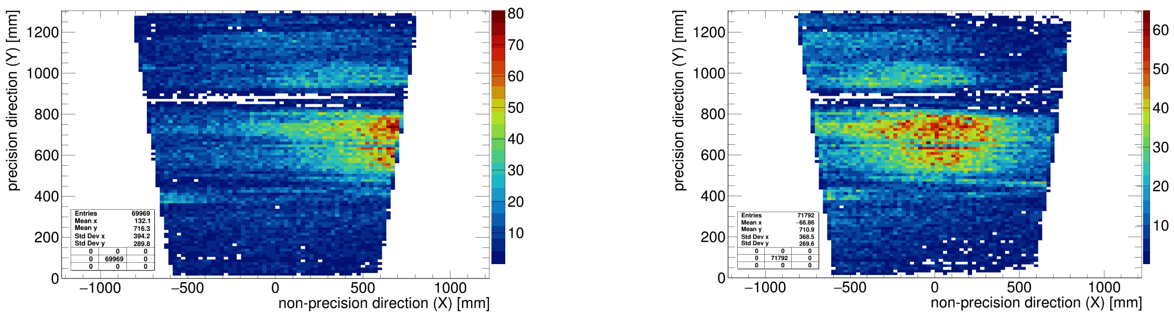

(a) Map without correction

(b) Map corrected

Figure 4.13: (a) The area cut restricts virtual stereo clusters to the active area of the detector. Due to the 60° inclination during the experiment and the distance $\Delta z = 16.9$ mm between the stereo layers, the virtual stereo clusters are shifted along the x-axis by an equivalent of 1315 strips (roughly 0.56 m). (b) Applying eq. 4.2 and eq. 4.4 corrects the positions.

Trackslopes - 'm': Assuming that cosmic muons hit the experiment only at angles of incidence within a limited variation around vertical inclination, allows for cuts on the track slope. Its range can be determined through evaluation of tracks reconstructed from all possible combinations of clusters. The random distribution of neutron clusters yields a broad spectrum of slopes for incorrect reconstructions. By contrast the directionally created muon clusters lead to a range of slopes that fits the geometric expectation.

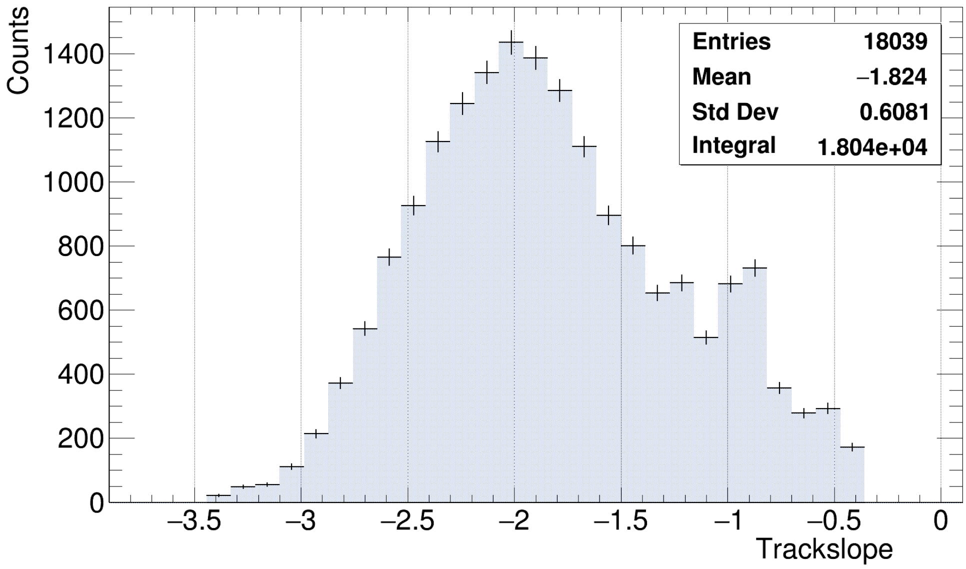

Figure 4.14: Distribution of slopes for muon-tracks derived by the efficiency-analysis. A cut limits slopes to a range between -3.4 and -0.4. Zero inclination would be equivalent to a perpendicular track through the detector. The peak at slope -2 is equivalent to an inclination of 63.4°. The deviation of 3.4° from the 60° inclination of the setup is a result of the track inclination dependence of the spatial resolution (Bortfeldt, 2014), as the slope is reconstructed using the centroids of three clusters. The source of the spike in counts of slopes around -0.9 is unknown. They can also be observed as in fig. 4.15

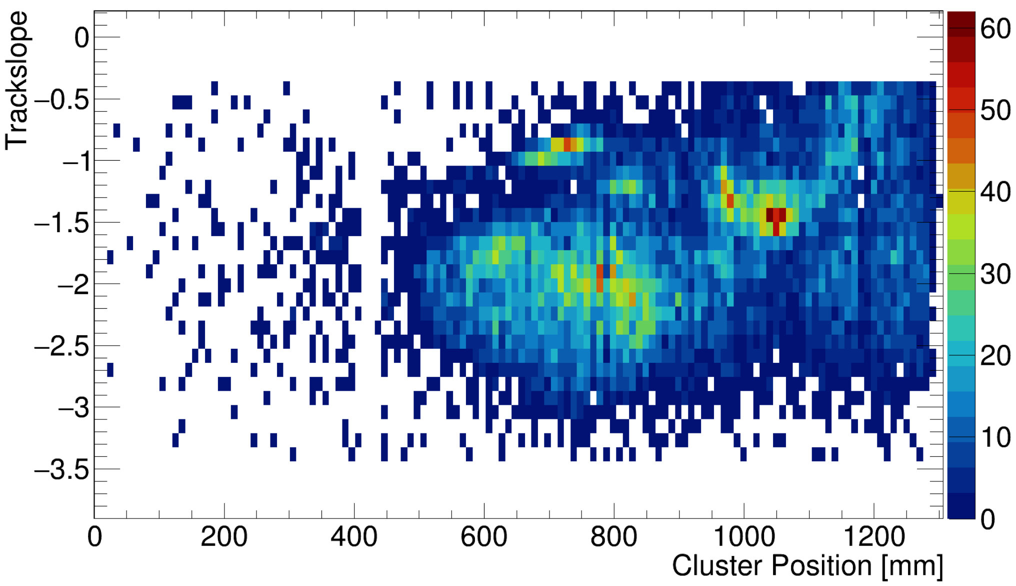

Figure 4.15: Trackslopes for efficient muon tracks as a function of the EI position in mm. The grouping of slopes of -1 and -0.9 around the 700 mm position contributes to the spike in the slope distribution (see fig. 4.14). The distiribution of slopes shows that few tracks are reconstructed in the small board.

Exclusion of noisy strips: This cut is not a general selection, like the A, τ and m cuts, but instead addresses localized electronical issues. There were four regions with strong noise across three detector layers. Typical sources of local noise are the connections by the zebra connectors, or defective APV-boards. Since clusters reconstructed within these regions are mostly noise, they were completely cut from the selection process.

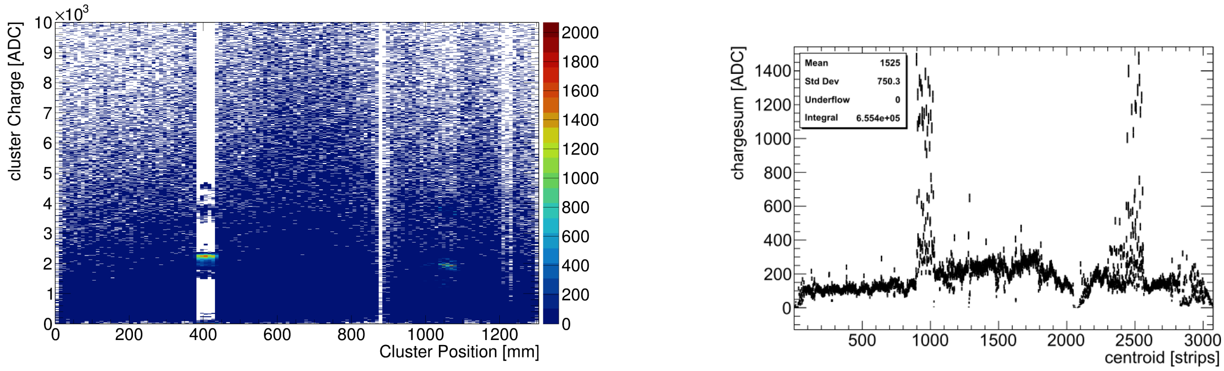

(a) Cluster charge measured in the SO-layer as function of the position in P-direction.

(b) StereoOut charge projected

Figure 4.16: (a) The SO layer shows noticeable noise-charges around the 425 mm position (stripnumber 1000). The second noisy region around the 1060 mm position (stripnumber 2500) is less visible in this depiction. These noise regions measure mostly charges around 2000 ADC. The two white sections around 400 and 880 mm are insensitive areas due to faulty connection of the frontend boards. (b) The projected charge entries as a fucntion of the centroid position shows two noisy regions, one around strip 1000 and one around strip 2500.

Noisy strips were excluded for the analysis, by cutting centroids located in two regions of the SO layer and in one area in each of the layers SO and EI. The regions were determined by investigation of cluster charges as function of the centroid position (see fig. 4.16). Each region had a length of 128 strips, which implies that APVs were the cause of the noise.
Tracks are defined through the layers SO, SI and EO. The loss of three regions in these layers does not directly impact the efficiency, but reduces the amount of tracks found.
Since tracks in the efficiency-analysis (see below) are only accepted if they can be verified by a cluster in the EI layer, the loss of a region in that layer could dismiss some tracks. However removal of the noisy clusters in the EI layer had no impact on the number of efficient tracks, implying that the cut redundancy worked for that particular region.
The loss in active surface is unfortunate, as some of the noisy areas fall within the most active areas of the detector during the experiment.

Additional notes: The timing-cut was also tested in the following analysis of the efficiency with range of 4 timebins, motivated by the low number of clusters at the edges of the timing-range in the CRF data compared to the supposedly high number of background-clusters within these edge-bins in the tandem-data. This resulted in efficiency gain of 1.1 percent at the cost of 3000 accepted tracks, equaling one sixth of the number of accepted tracks at a range of 6 timebins. As such the full derived width of 6 timebins was kept, as the tradeoff was deemend unworthy.

The residual shows a correlation with the cluster timing (see fig. 4.17a). As (Herrmann, 2019) describes, this is an effect of tracks with an inclination. The inhomogeneous ionization of muons along their path in the drift-region distorts the charge-averaged position-reconstruction. This effect is to be attributed to the trackslope, yet appears as a timing effect due to the signal evaluation and centroid reconstruction-method. To correct the residual (see fig. 4.17b) the slope of the clustertime-residual-correlation is used.

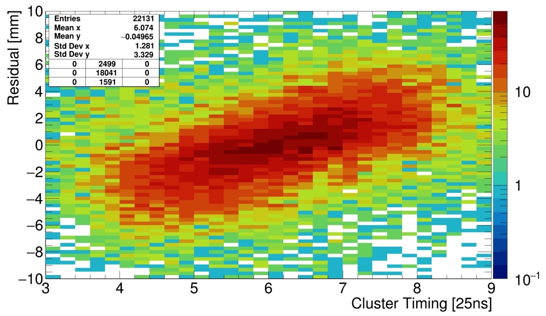

(a) Muon residual without time-correction

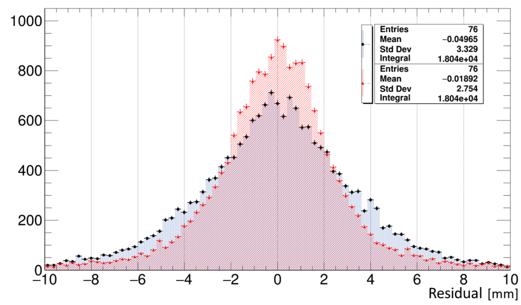

(b) Time corrected muon-resiudal

Figure 4.17: (a) The residual shows a correlation with the timing of the cluster. (b) Time-corrected residual (red) compared to the uncorrected residual (black)

4.3.3 Neglected Cut-Parameters

The cluster-parameters that weren't used were neglected due to them being not distinctive. The clusterparameters charge, size and μTPC-slope had near-total overlap with the pure-muon reference-data from the CRF. The cuts were tested individually but showed no improvements at a loss of tracks. Combinations of the neglected cut-parameters were also tested assuming that the interaction would select muon clusters. The assumption was negated as the application resulted in the reconstruction of zero tracks. As such the loss in tracks was deemed too severe to justify the application of these parameters as cuts.

Cluster-size The number of strips in one cluster is not distinct enough to filter the tandem data. The size of clusters generated by muons within the gas volume is misleading, as much of the signal is lost along the path for the 60 degree setup. For a muon at 60° inclination passing the 5 mm thick drift-gap, the cluster size should cover around 20 strips (8.7 mm). This leads to clusters which are split due to missing strips in between.
These disrupted clusters will be discussed in the results of this chapter.

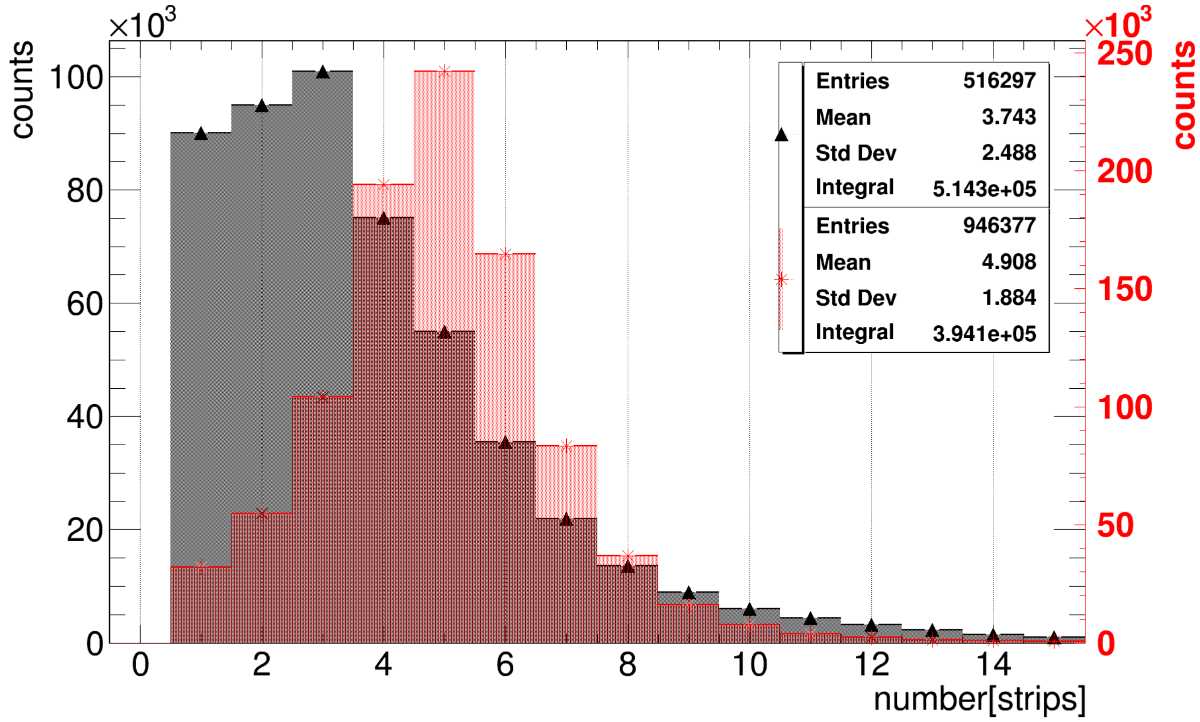

Figure 4.18: Comparison of cluster-sizes for CRF and tandem data (black). The size of a cluster is given by the number of strips recording a signal.

The size distributions for the CRF (fig. 4.18 red curve) and tandem-data (black) should be very different. Muons have zero inclination at the CRF, which results in a mean size of 4.9 strips. The expected size of about 20 strips at the tandem experiment was not observed in the reconstructed clusters.
Thus the size distribution of the CRF is not comparable to the tandem-distribution (black) as it was measured with a mean inclination of zero for muons. Because of the overlapp and the uncertain comparability the size-cut was not applied. It might be applicible in experiments with more information.

Cluster-charge The cluster charge showed no usable distinction by comparing CRF and tandem data (fig. 4.19). Assuming the shape of the muon-charge-distribtion persists at the tandem experiment, the most frequent cluster charges would need to be cut. As such this parameter was not applied due to the overlapp and lack of distinction.

Note that the distribution for the CRF data in fig. 4.19 was measured over a significantly longer time with only muon clusters forming the distribution. Due to the contribution of neutron clusters and the short measurement-period of three days, the hidden muon distribution might be less pronounced.
As will be discussed in the results section, the formation of disrupted clusters hints at low charge values for muons and incomplete ionization along the track.

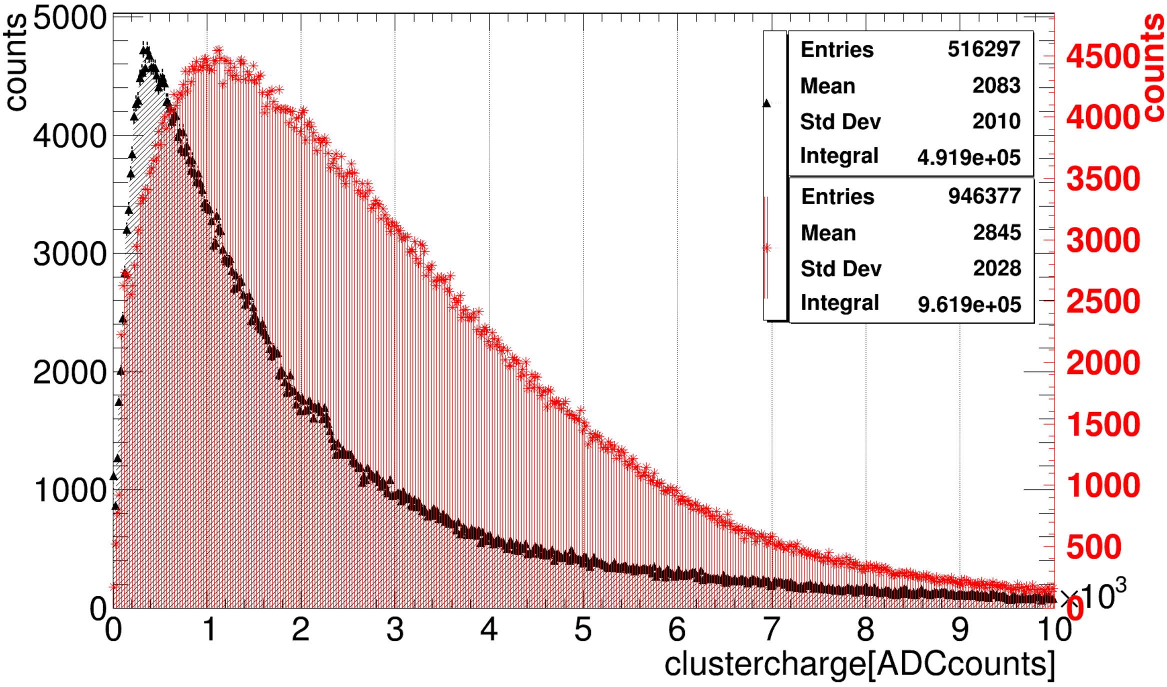

Figure 4.19: Comparison of cluster-charges in ADC counts for CRF and tandem data (black).

μTPC-Slope The so-called μTPC-method allows to reconstruct the slope of a particle track within a single detector layer. If the drift-velocity is known the slope of the track can be reconstructed from the timing and position of the signals (see fig. 2.8a). Note that the signal of ionization happening near the cathode reaches the strips last due to the distance, while signals created near the mesh are registered first.
Fig. 4.20 shows the comparison of the CRF (red) and tandem data (black). As expected the tandem distribution shows a clear asymmetry, which might have been exploited. From the setup, distinct negative slopes are expected for muons. The distribution does not match that expectation. Note that the unit of the μTPC-slope is different from the unit of the trackslope reconstructed from centroids.
The the sharp tip in the center of the distribution indicates a failure in the μTPC-reconstruction. Thus this parameter was neglected due to the uncertain reliability of the reconstructed μTPC-slope.

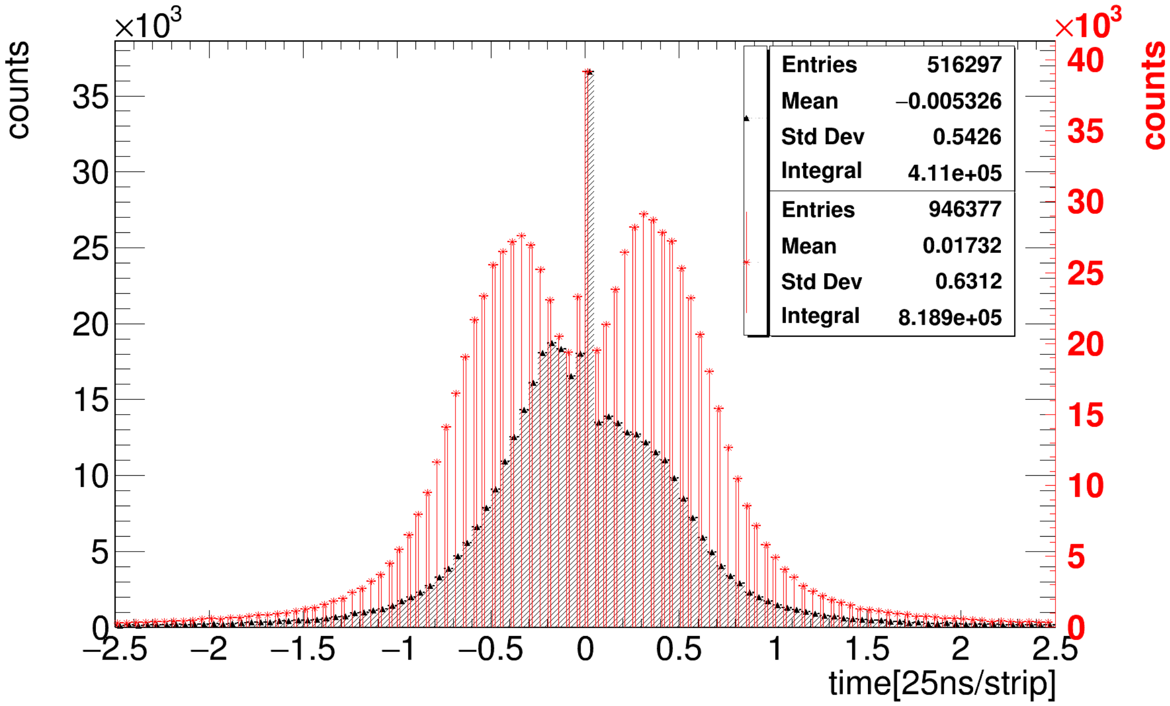

Figure 4.20: Comparison of the track slope reconstructed with the μTPC-method for CRF and tandem data. Both data sets show a distinct spike at zero-inclination caused by inaccurate μTPC reconstruction.

4.3.4 Track Reconstruction for Muon Analysis

The track reconstruction for the efficiency-calculation is a different appraoch compared to the preceeding analysis. The goal of the latter was to find and test selection parameters by minimizing the residual. The efficiency-analysis does not define its tracks by minimizing the residual, but is only reliant on the derived cuts minimizing the number of possible tracks per event.

First a virtual stereo cluster is calculated using the stereo layers and matched with the cluster in the EO layer in the same manner as before. This track is defined as a found-track built from the SO, SI and EO layers and the associated clusters are stored. Additionally the number of tracks found for each event is stored. Note that these tracks consist of three clusters, one from each of the SO, SI and EO layers.
The application of the derived cuts severely limits the number of tracks reconstructed for an event. Due to the selection of clusters and the geometrical constraints, tracks were only reconstructed for 37,102 events out of the total 170,273.

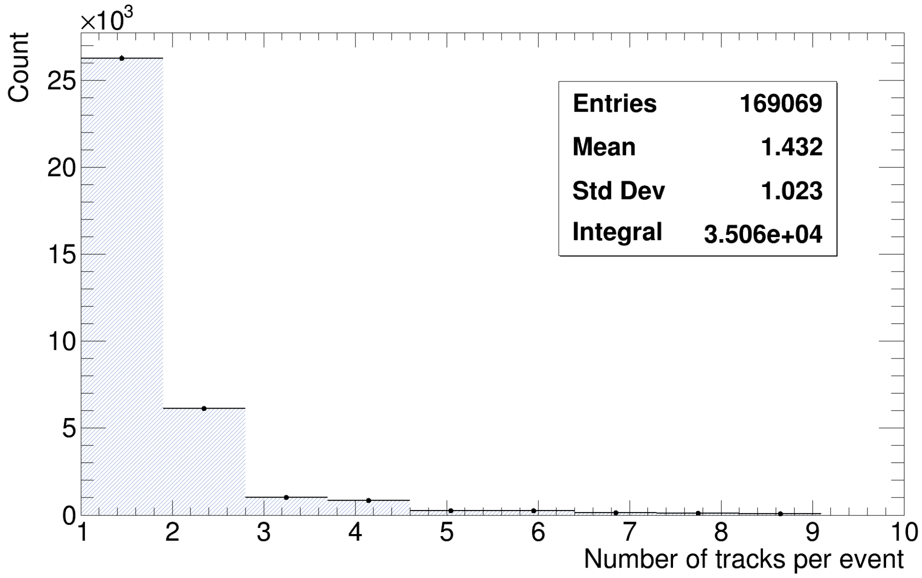

Figure 4.21: Distribution of the number of tracks found per event. 1204 events are cut due to being recorded during drops in the beam intensity.

The events are sorted by the number of tracks they contain. Events which consist of exactly three clusters (one in each of the SO, SI and EO layers) with the cuts applied, allow only a single possible track. These so-called single-track events are assumed to reliably represent a muon. The EI clusters were only subjected to the timing cut and a deselection of noisy channels, as the slope(m) and area(A) cuts are covered by the track-reconstruction. The deselection of noisy channels had no effect, implying that either the three cuts removed the corresponding clusters or that an efficient residual was found regardless. The timing cut on the EI layer guarantees that all clusters of as efficient track have a muon-like timing.
The number of possible tracks for an event is given by the number of combinations of clusters which pass the applied cuts. Events with a higher number of possible tracks were discarded due to their indecisive nature. Events forming two possible tracks were investigated seperately.

The found single-track events are then matched with the EI-layer in a seperate step. If any clusters are present in EI the smallest residual is calculated. If the residual lies within a predefined acceptance-range of 10 mm the track is considered an efficient reconstruction. The 10 mm range corresponds roughly to the width of 20 strips a cluster can form under the 60 degree inclination at the experiment.

The key difference between both methods is that in the efficiency analysis only unambigous events are accepted. The result shows a residual-distribution which resembles the expected Gaussian distribution (fig. 4.22a).
By comparison the minimization of the residual of the preceeding analysis allows multi-track events to contribute a track based on a small residual. The random distribution and frequency of neutron clusters leads to a sharp peak of residuals close to zero (fig. 4.22b).

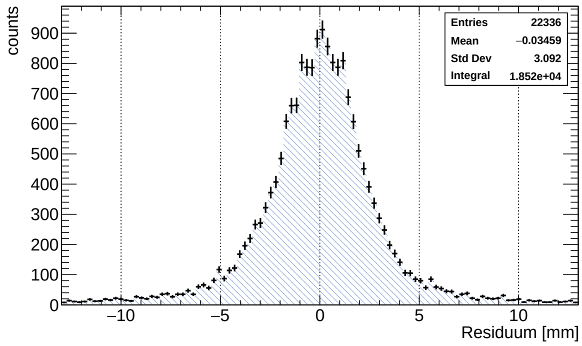

(a) Residual of the efficiency analysis

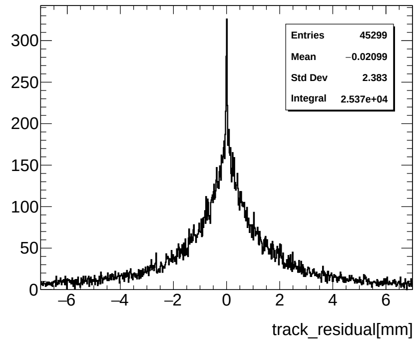

(b) Residual of the broad analysis

Figure 4.22: Comparison of the residual-distributions for the efficiency-algorithm and the initial data analysis. (a) Residual distribution for single-track events in the efficiency analysis with cuts applied. Using exclusively single track events veryfied by an efficient EI cluster, creates the expected Gaussian distribution (b) By comparison, the residual distribution of the initial data analysis failed, due to minimizing on arbitrary neutron clusters. Cuts were applied to reduce the central peak, limiting the number of tracks.

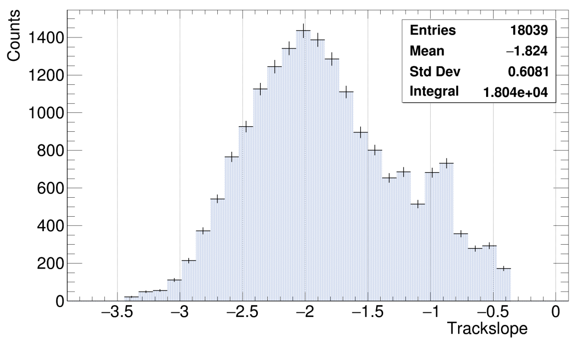

(a) Trackslopes of the efficiency analysis

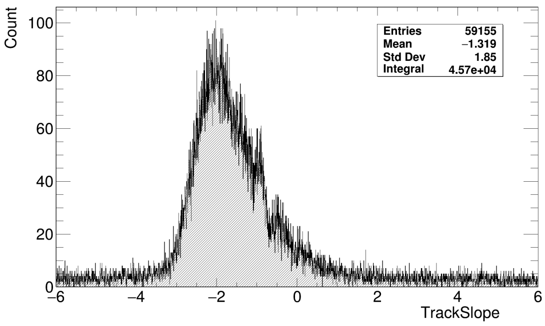

(b) Trackslopes of the broad analysis

Figure 4.23: Comparison of the slope distribution for the efficiency-algorithm (a) and the initial data analyis (b).

4.4 Results

The triggers of the setup are presumably initiating two false events for each muon due to the intense background. Accordingly up to 56,000 events out of the 170,273 events recorded should correspond to a muon. This number is further decreased by the instances of events with empty layers, multi-track events and noise.
Ultimately a total of 37,102 tracks were found, of which 26,253 reconstructed a single track. 18,039 of these single-track events formed an acceptable residual, resulting in a

mean efficiency of 68.7% for the experiment. Note that the beam was on high intensity for about 70% of the measurement.

Events total	170273
No Track	133171
Tracks found	37102
Single-Track events	26253
Two track events	6131
Events with 3+ tracks	4718

Table 4.2: Event Stats

4.4.1 Single Track Events

Only events are used in the further analysis, which consists of clusters forming a single track within the presented cuts. Events with several possible tracks were not considered. With the Timing, Active Area and Trackslope cuts in place, 15.4% of the recorded events form single-track events (roughly half of the expected 56,000 muon events).
Only these events are assumed to allow reliable reconstructions of a muon path, since the triggers are set to record single muon events.

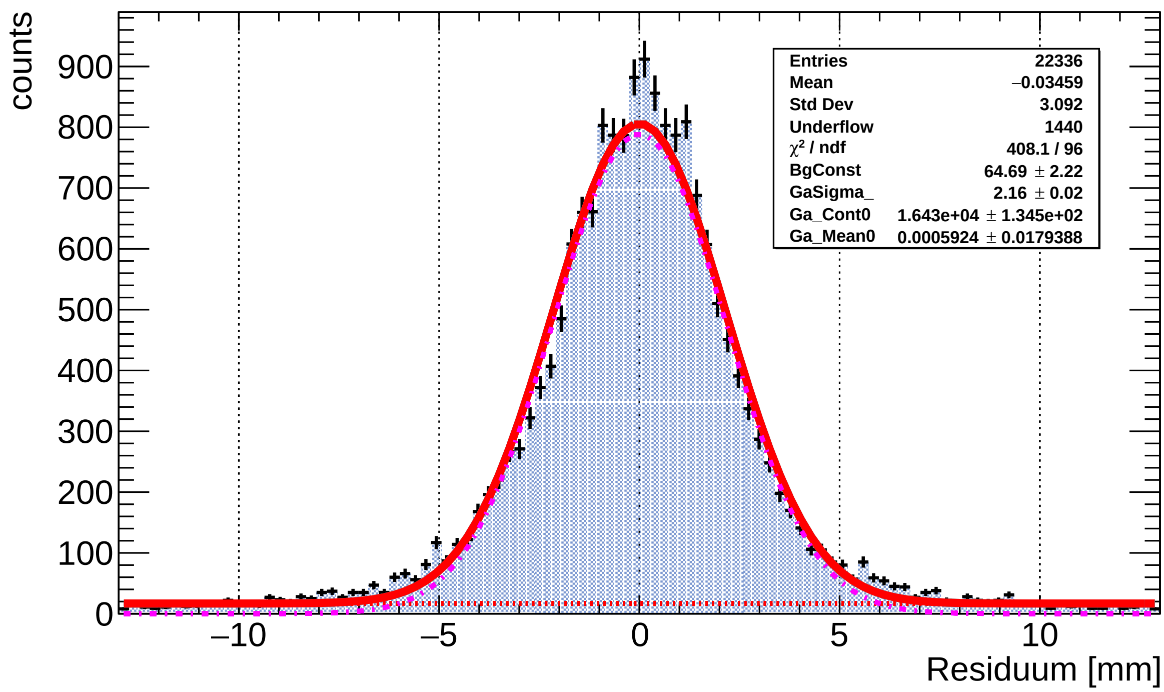

Figure 4.24: Residual for single-track muon events. The Gaussian-fit resembles the Gaussian distribution of the residual for pure muons from the CRF data (see fig. 4.6). Due to the 60° inclination, the standard deviation is 5 times as broad compared to the CRF (in agreement with (Lösel, 2017)).

Fig. 4.25 displays the track of a single-track event, reconstructed from all the clusters measured. Through the applied cuts, only the clusters depicted in fig. 4.25a remain.
Fig. 4.26 shows the single-track residual as a function of the size of the chosen EI cluster (a) and trackslope (b) respectively. Note that the residual is time-corrected and that trackslopes can only be calculated according to the P-direction. Both distributions are symmetric.

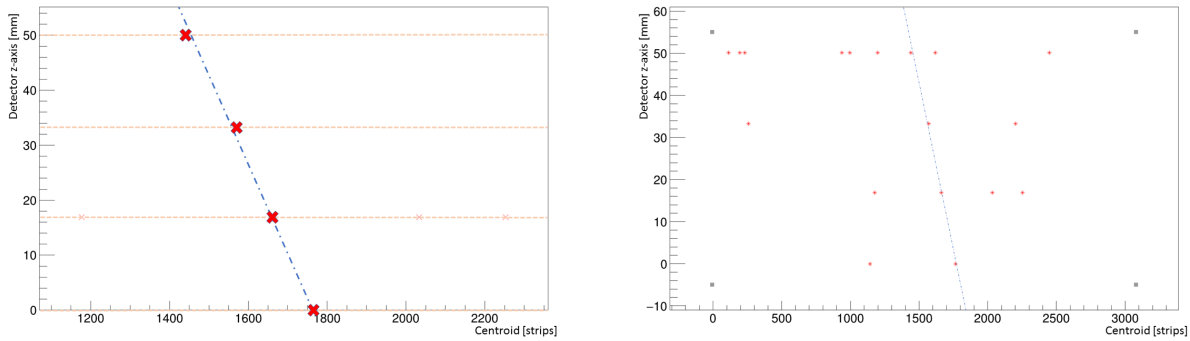

(a) Muon-track for a single-track event

(b) All clusters of the event

Figure 4.25: Event displays for a single-track event. (a) The track is formed from three clusters. In the SO layer (top) the cluster is positioned at strip 1450, in the SI layer at strip 1550 and at strip 1760 in the EO layer (bottom). In the EI layer all allowed clusters are depicted. The one at strip 1650 is chosen. The horizontal lines (orange) represent the detector layers, the dashed blue line the track formed by the four clusters (red crosses). (b) Depiction of all clusters recorded in this event. By cutting on the cluster timing, the allowed stereo combinations and the slope of the resulting track, only three clusters remain (not counting the EI layer) and form a single track, indicated by the dashed blue line.

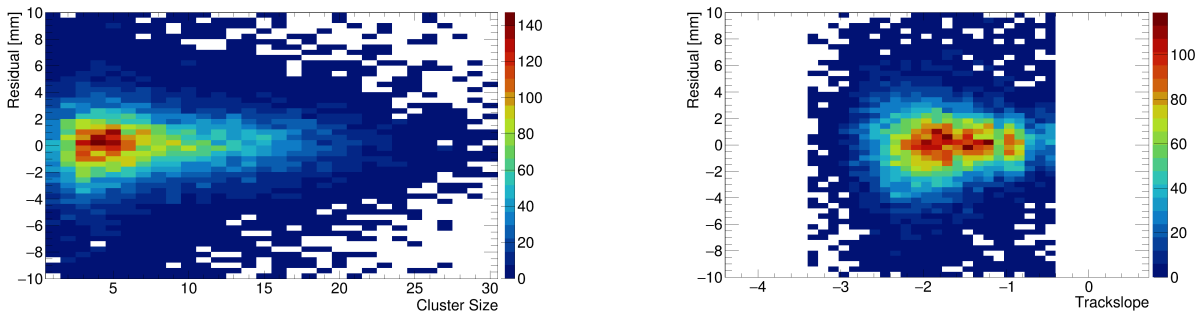

(a) Residual as a funtion of clustersize

(b) Rresidual as a function of the tackslope

Figure 4.26: (a) Single-track residual as a function of the EI clustersize (a) and trackslope (b).

Single-track events	26253
Verified muon tracks	18039
Tracks without EI-clusters	4122
Residual-rejected tracks	4092

Layer	Events without a cluster
EO	21841
EI	26657
SI	25767
SO	20702

Table 4.3: Stats for tracks and empty layers

4.4.2 Twin Cluster-Events

Through direct investigation of events which were reconstructed with two tracks, a frequent appearance of so-called twin-clusters was found. These clusters were defined to consist of two clusters in close vicinity to each other, such that combining them into one cluster changes the event to single-track event (see fig. 4.27). The source of these twin-clusters supposedly lies in the 60 degree inclination combined with the inhomogeneous energy deposition of muons and the suppression of noise during the experiment.
For a muon with a 60 degree inclination, the 5 mm thickness of the drift-gap of a single detector-layer covers about twenty strips due to the projection of 9 mm along the precision direction. As discussed above, muons tend to distribute energy along their path in an inhomogeneous manner (Flierl, 2018). Low charged strip signals are probably discarded due to the necessary noise suppression. The remaining signals are falsely identified as two separate clusters by the clustering-algorithm.

Therefore, the parameters of the cluster reconstruction as well as the algorithm were changed to allow for clusters being built from signals with a gap of up to 16 strips. This change resulted in the formation of roughly ten thousand additional single-track events, pushing the number of accepted tracks by two thirds to 26,253.
These changes and the resulting inclusion of the twin-clusters did not deform the distribution of the residual, supporting the assumtion they're split muon clusters. Bigger gaps of up to 20 strips did not show a significant increase in the number of Single Track events nor improvement in the detector efficiency (less than 1%).

This indicates another reason behind the low number of found tracks. With many tracks being falsely split into separate clusters due to little and separated energy depositions, it is reasonable to assume that an unknown portion of tracks did not form detectable clusters at all in some layers.
This has also a detrimental effect on the sizes of muon generated clusters, which is definded by the number of strips activated. With the inclination given by the tilted setup, one would assume an increase in the size parameter of muon clusters, which might have been used to further differentiate them from neutron generated clusters.
As a result the actual extend of any given cluster is unkown. This also factors into the failing reconstruction of the μTPC-slope.

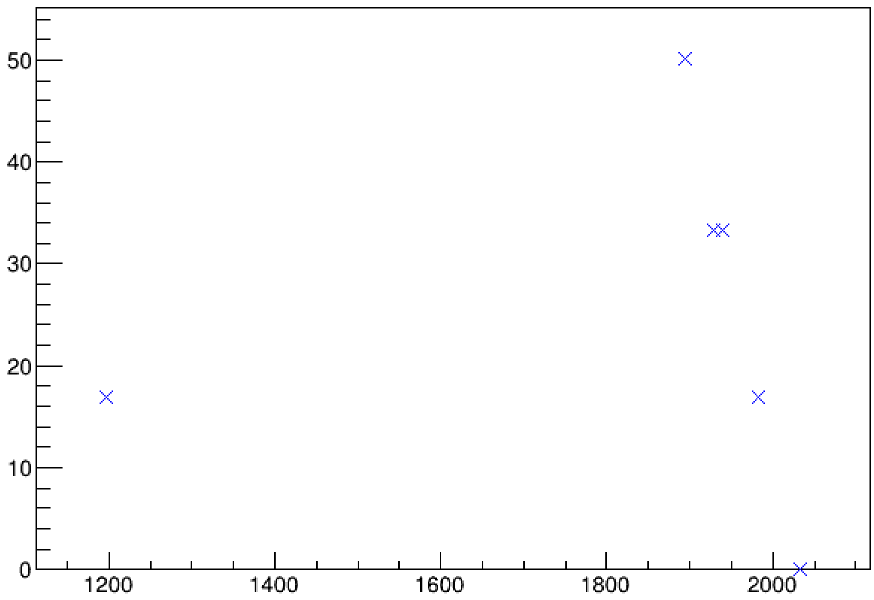

Figure 4.27: Event display containing a twin cluster in SI layer (second from the top). Due to seperation between the signals two clusters are reconstructed instead of one. Without correction two virtual stereo clusters can be calculated for the event, reconstructing two possible tracks and therefore dismissing the event. The frequent appearance of two clusters close to each other led to an investigation of the cluster-formation method.

4.4.3 Efficiency

The efficiency of the EI layer is given by the ratio of efficient tracks to the total number of reconstructed single-tracks. In the absence of particle backgrounds, this ratio would be determined by the number of sufficiently identified clusters. At the CRF the modules perform at efficiencies above 90%, owed to the purity of events and the low inclination. Furthermore. the extended measurement times at the CRF reduce the error in the efficiency calculation.
The neutron background at the tandem experiment leads to ambiguous events due to the plethora of clusters. A portion of neutron clusters can be filtered as priorly discussed. Those neutron clusters which mimic the characteristics of muon induced clusters pass the filter process however, reducing the efficiency. Another factor was the noise in four sections across three detectors and the loss of signals.
To get a measure of efficiency and to compare it to the neutron-background, the found and accepted tracks were grouped in time-segments of 30 min each and averaged (fig. 4.28). Dividing the accepted tracks (fig. 4.28b) per time-segment with the found tracks (fig. 4.28a) yields the average efficiency for that time-segment (fig. 4.29).

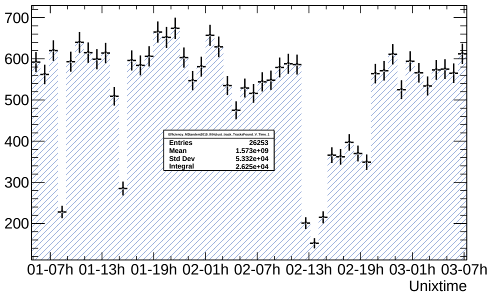

(a) Found single event tracks

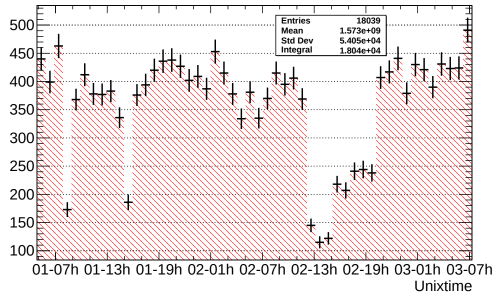

(b) Accepted single event tracks

Figure 4.28: (a) Single-tracks found over time. (b) Single-tracks accepted over time.

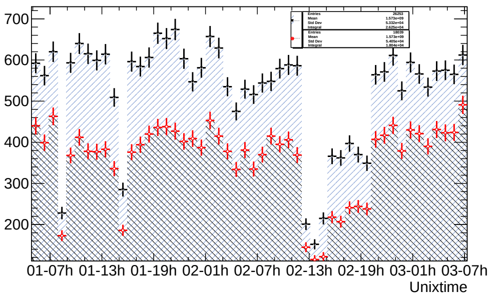

(a) Found and accepted tracks

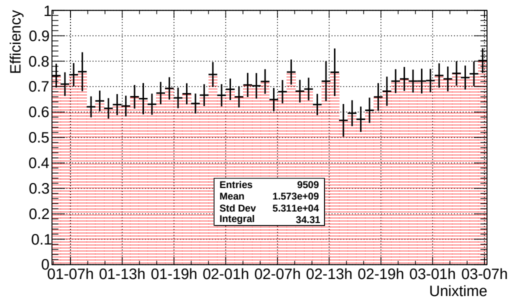

(b) Efficiency over time

Figure 4.29: Comparison (a) of found and accepted tracks over time and the resulting efficiency (b).

Beam-flux thresholds: The tandem beam and by result the neutron beam were run at two flux-rates and without flux respectively. During the measurements the beam fluctuated (see fig. 4.30). To get a clean picture of the correlation of the efficiency with the background, only data recorded with a stable beam was taken into account for this correlation. To select these times, the beam flux measurement was divided into time frames and checked to be above defined thresholds. This was done by timebins of 1 sec and removed 1204 events. The effect of this selection was marginal on the efficiency and number of tracks reconstructed and indistuingishable in the residual, due to the small number of these times contributing to the single-track events.

The selection is necessary to get an visually interpretable correlation see fig. 4.30. On the analysis itself, the effect is marginal with practically identical distributions for the residual and trackslope. Through the application of beam-thresholds, the mean efficiency decreases by 0.0179% as does the number of accepted single-tracks by 182 (about 1%).

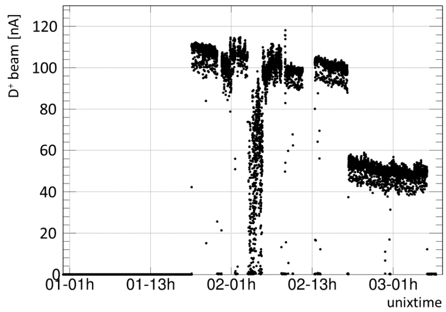

(a) beam thresholds

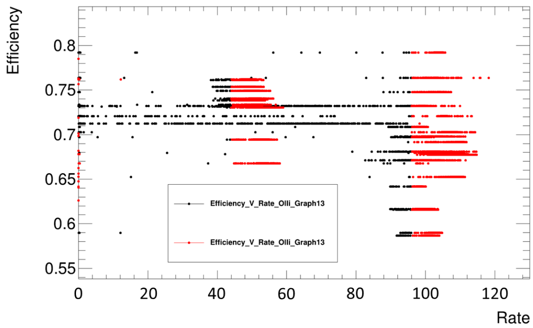

(b) Efficiency over time

Figure 4.30: (a) Beam flux of the deuterium beam produced by the tandem accelerator. Three current were applied: 0, 50 and 100 nA. Note that the beam was set to 100 nA at 01-09 h. The recording of the beam flux was started at 01-19 h. (b) Highlighted in red are the efficiencies that are not cut by beam flux thresholds. Note that the graph omits the frequency of occurence - black points correspond to 0.7% of the events.

Correlation with the beam intensity: Fig. 4.31 shows a comparison of the efficiency and the beam flux as a function of the time. The recording of the beam flux started at 19 o'clock on Nov 1st, while the beam has already been active as indicated by the sudden decrease in efficiency at 9 o'clock. To get a better picture of the corellation over the full measurement, fig. 4.33 uses the signal rate of one of the trigger channels. Here the sharp increase in registerd particles correlates with the decrease in efficiency. Thus fig. 4.33 shows a dependence of the efficiency with the intensity of the beam.
Notably the efficiency rises slightly with time, coinciding with slight decreases in beam-flux and trigger output. The behaviour of the efficiency shows a direct and sharply timed correlation with the background for the majority of the measurement. The exception is one region of decreased efficiency on Nov 2nd, from 14 to 20 o'clock. A change during this timeframe can also be observed in the slope distribution (fig. 4.32a) and charge of the EI clusters of reconstructed tracks (fig. 4.32b). The cause of this event is unclear.

The lower region of the efficiency on the 1st from 9 o'clock until the beam-recording startet around 19 o'clock (fig. 4.31), falsely contributes low efficiencies at zero beam-flux in fig. 4.34. These efficiencies belong to events under high background (100 nA), but were recorded without record of the background intensity.
Neglecting these results leaves a narrow distribution of the efficiency of up to 80% in the absence of a background (fig. 4.34), compared to the efficiency-clusters forming for the other two rates. Higher rates show a wider distribution of efficiencies, with the extend of the distribution increasing with the intensity.
This shows that the efficiency is directly correlated with the background, with the mean efficiency falling and efficiencies increasingly diverging as the background increases. Small decreases in the background cause small increases in the efficiency for the corresponding time frame.

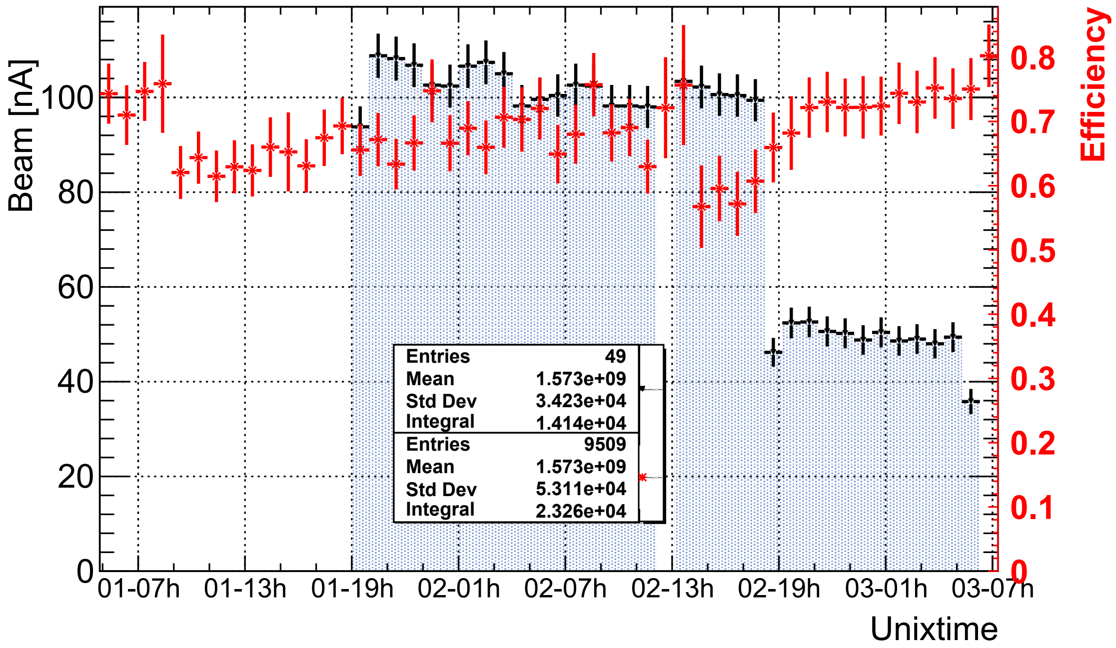

Figure 4.31: Comparison of the efficiency (red) and the beam-flux (blue) over time. The efficiency and beam flux were averaged over 30 min intervals. The beam was on prior to recording. The drop fig. 4.33 at 01-09 h reveals the corellation between the efficiency and neutron background upon activation of the beam. Fig. 4.28 shows a drop in the number of found (a) and accepted (b) tracks around the time frame from 02-14 h to 02-19 h, coinciding with the drop in efficiency. The cause of this behaviour is unkown. At the end of the measurement (03-06 h) the beam was off, causing a rise in efficency to 80%.

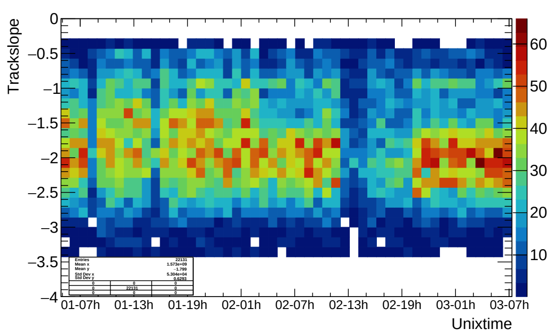

(a) Trackslopes as a function of time

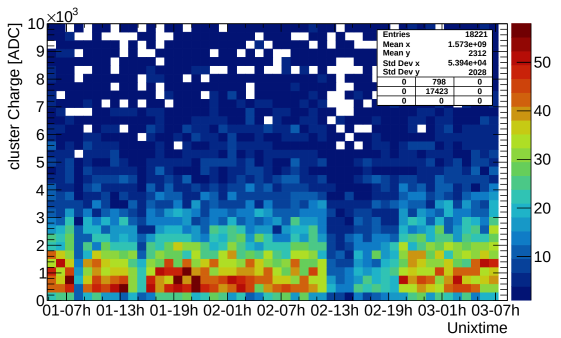

(b) Charge of residual-clusters as a function of time

Figure 4.32: (a) Efficient muon trackslopes as a function of time. (b) Charge of the residual-clusters of accepted muon tracks as a function of time.
Both graphics indicate the timeframe of an unkown event from 02-13 h to 02-20 h.

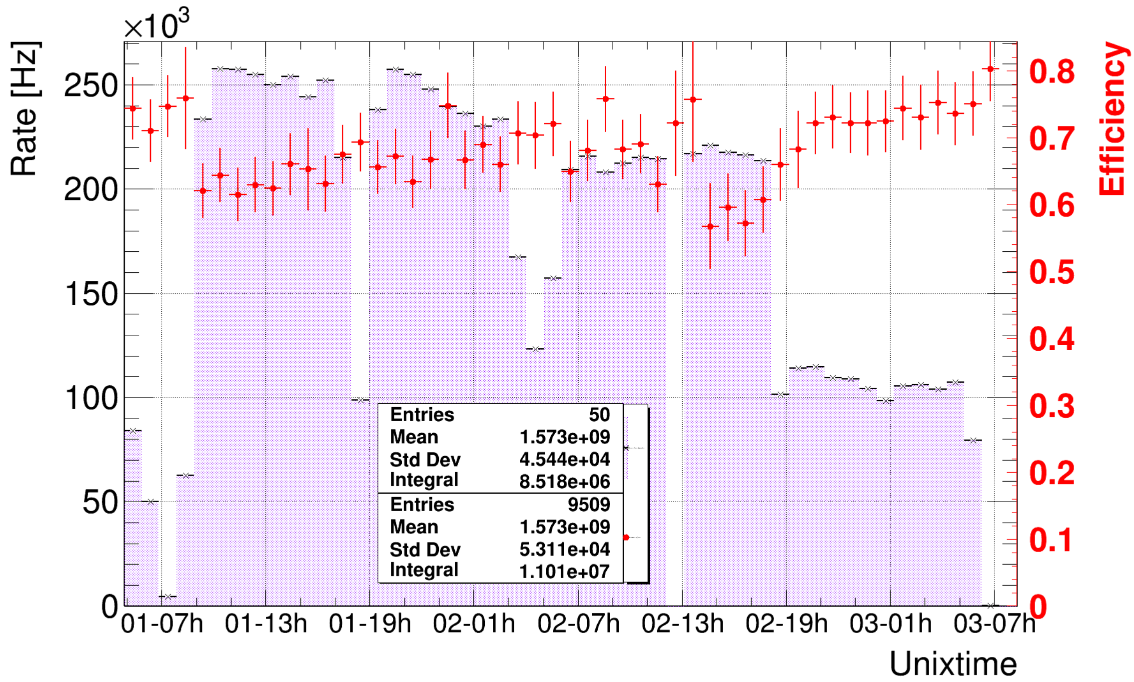

Figure 4.33: Comparison of the efficiency with the trigger rate [Hz] of one of the scintillators as a function of time. Efficiency and trigger rate were averaged over 30 min intervals. The activation of the beam around 1-09 h coincides with a decrease in efficiency.

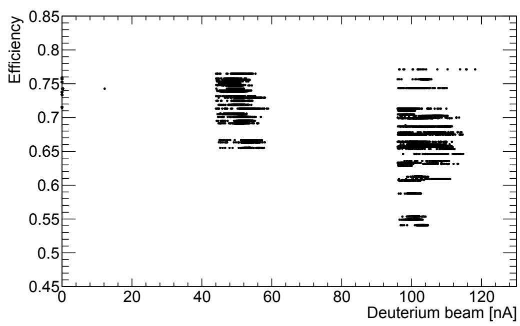

(a) Graph: Efficiency as a function of the beam

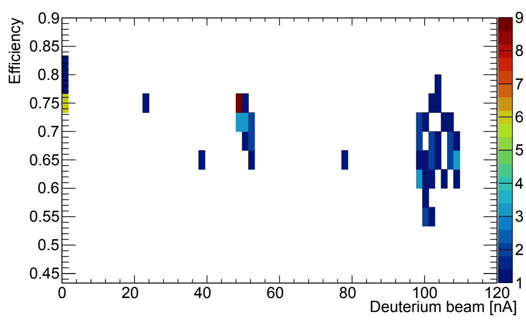

(b) Histogram: Efficiency as a function of the beam

Figure 4.34: Efficiency as a function of the beam-flux as a graph (a) and as a 2d histogram (b). Two visualizations were chosen as the graph depicits the extend of the distribution, while the histogram reveals concentrations. Both figures show a correlation between the beam intensity and the efficiency. For increasing beam intensities the mean efficiency decreases and becomes less consistent. Since the exact beam current was not recorded prior to 01-19 h, efficiencies from that timeframe are not depicted.
The graph (a) uses the threshold visualization and uses averages over 30 min for the efficiencies. Each point represents one second and shows the average efficiency for the corresponding time window as a function of the beam flux at that second (frequent combinations overlapp). (b) The histogram uses time-averaged bins, compressing both the horizontal and vertical structures of the graph.

Beam current I_D	Absolute efficiency	Relative efficiency
0 nA	80%	100%
50 nA	72%	90%
100 nA	65%	≈81%

Table 4.4: Absolute and relative efficiency in relation to the beam intensity (derived from fig. 4.31). Only efficiencies with measured beam intensities were taken into account. The efficiency without the neutron background sets the scale for the relative efficiencies at 50 and 100 nA beam intensity. The 65% efficiency takes the event during the time frame 02-15 h to 02-19 h into account (see figs. 4.31 and 4.34). Omitting this time frame would result in a higher efficiency for $I_D = 100$ nA.

The experiment shows that for an SM2 module set up at an inclination of 60°, the EI layer performs at an efficiency of 80% without the neutron background. The efficiency at this inclination is roughly 10% smaller compared to the performances measured at the CRF at zero inclination, which are taken over a significantly longer period of time and with monitored readout electronics.
As expected, the efficiency is lower under irradiation with a strong neutron background. For the strongest background generated ($I_D = 100$ nA) the relative efficiency still reaches 81% (compared to the reference efficiency for the 60° inclination).

Chapter 5

Conclusion and Outlook

Conclusion

Humidifier upgrades The motivation to study the performance of the SM2 Micromegas under induced water-pollutions was to determine whether small water portions could have beneficial effects, like they have been found in other gas-detector technologies.
The studies proved humidity to be detrimental to the detector's HV-stability, resulting in a high number of discharges. For a high-frequency precision-tracking detector like the SM2, the loss of several sectors to discharges due to humidity necessitates arid conditions.

Despite the aversion to humidity, a useful blueprint for a cost-efficient humidifying device was derived and observations about the behaviour of the module under changes in the working-gas were made. The former might be used in similar investigations of other detectors.
The studies have shown that the SM2 module will reach stable humidity levels below 2000 ppm within a few days, despite the warm and humid environment. During extended operation the modules should be able to reach and keep stable levels on its own. Naturally, control of the environmental temperature and humidity is beneficial.

SM2 module 3 irradiated by neutron-backgrounds The neutron-irridiated SM2 module performed with an average efficiency of close to 70%. This is roughly 20% less than in pure-muon experiments measured at the CRF. Without the background, efficiencies saturate around 80%. This reduced efficiency is owed to the inclination of 60 degrees compared to the perpendicular mean-inclination at the CRF. Noisy readout-channels and the necessarily strong noise-reduction impeded the efficiency further.
As expected, irridiation with neutrons leads to a decrease in efficiency. Using one cluster parameter and the geometric aspects of the experimental setup for cluster selection, the relative efficiency reached 81% under the strongest applied background and 90% for the medium background. The 18039 muon-tracks that were identified matched the expected profiles derived by (Herrmann, 2019) and (Flierl, 2018).

To increase the efficiency more insights are necessary. On one hand the apparent loss of muon-clusters indicated by the small cluster-sizes and emergence of twin-clusters, should be prevented as far as possible. On the other hand additional and refined selection parameters offer potential.
Standing out for potential improvements is the stereo position reconstruction and correction. Without the non-precision (NP) correction, the position of virtual clusters can differ by half a meter at a 60 degree inclination. Actual information about the NP-slopes instead of the assumption of a mean inclination should considerably improve the track selection and therefore the efficiency. This necessitates a second source of information for the NP-coordinates, which was not present at the tandem experiment.
The μTPC-slope offers another potent tool for cluster selection. According to (Bortfeldt, 2014), the μTPC-reconstruction becomes increasingly precise at stronger inclinations. Therefore usage of this feature of the SM2 Micromegas module for the analysis will improve the performance.

Outlook

Extended Humidity Studies

Humidifier upgrades The humidifier could easily be upgraded to keep the water portion stable by usage of dynamically adjusting valves over manually operated ones. The static valve positions used during the studies showed close to identical humidity curves over days with similar climatic conditions. Valves adjusting in a pre-programmed pattern offer an alternative to dynamically adjusting ones.
Another possibility would be further reducing the gas flow through the wet path of the humidifier while introducing a heating element in the reservoir to generate an additional degree of freedom in adjustability.
Should induced water portions prove beneficial to a detector-type, the usage of soft tubing-material over chosen length might offer a very cost-efficient option, if stable temperatures and air pressure are present.

Extended studies Further investigations of the behavior of water vapour inside the detector, like build-up of water droplets or degradation of components, would be possible by opening a module after the prolonged flooding with humidified gas, to search for damage. Another possibility would be using mixed in pigments in the gas flow. These pigments would collect at certain positions, accentuating where pooling occurs.
Obviously, the resulting contamination necessitates a throw away test module and pigments which behave close to vapour (or at least droplets), which is not given for the sizes of pigment molecules.

SM2 modules at ATLAS

The efficiency under inclinations can be further improved. Additional data points for the non-precision slopes would improve the positioning of the virtual stereo cluster (see correction terms eqs. 4.2 and 4.4), as well as adding a dimension to the trackslope cut.

Compared to the tandem experiment, the full muon-spectrometer at ATLAS will offer more redundancies and a more localized origin of particles. This allows to select track slopes in a more refined way, dependent on the point of transit reconstructed from the stereo-layers. Additionally, technical defects like noisy sections or electronics can be addressed during the prolonged measurements, which was not possible in the constrained time frame of the tandem experiment.
The combination of these should increase the efficiency of SM2 modules under inclinations and background noticebly.

The application of neural networks for the investigation of data is also promising. Developments of this type of algorithms in the recent years have been rapid. Where this thesis worked with *traditional* coding and *manual* analysis, the application of neural networks to processes like track finding or particle identification entices refined parameters and should result in increased performance.

List of Figures

List of Tables

Abbreviations

ASIC	Application Specific Integrated Circuit
ATLAS	A Torodial LHC ApparatuS
CERN	European Organization for Nuclear Research
CRF	Cosmic Ray Facility
CSC	Cathode-strip chambers
DOF	Degrees of Freedom
EI	Inner ETA layer
EO	Outer ETA layer
FEC	Front End Connector cards
FESTO	(see Appendix)
HL-LHC	High Luminosity LHC
HV	High Voltage
LHC	Large Hadron Collider
LM1	Large Micromegas Module 1
LM2	Large Micromegas Module 2
LMU	Ludwig-Maximilians-Universität München
MDT	Monitored Drift Tube
Micromegas	Micromesh Gaseous Structure
MIP	Minimum Ionizing Particle
NP	Non-Precision
NSW	New Small Wheel
P	Precision

PCB	Printed Circuit Boards
PMT	Photo Multiplier Tube
SI	Inner Stereo layer
SM1	Small Micromegas Module 1
SM2	Small Module 2
SO	Outer Stereo layer
sTGC	Small-strip Thin Gap Chambers
Vaisala	Vaisala© Drycap® dewpoint-transmitters (see Appendix)

References

Aleid, L. (2020, September). *The results of simulation of temperature distribution in atlas cavern.* Private Communication. (Internal Presentation ATLAS, https://indico.cern.ch/event/906700/, [accessed 05-Oktober-2020])

ATLAS Collaboration. (2008). The ATLAS Experiment at the CERN Large Hadron Collider. *JINST*, *3*. (https://iopscience.iop.org/article/10.1088/1748-0221/3/08/S08003/pdf [accessed 04-July-2019])

ATLAS Collaboration. (2013). *New Small Wheel Technical Design Report* (Bericht Nr. CERN-LHCC-2013-006. ATLAS-TDR-020). CERN. (http://cds.cern.ch/record/1552862/files/ATLAS-TDR-020.pdf [accessed 04-July-2019])

Bethe, H. (1930). Zur Theorie des Durchgangs schneller Korpuskularstrahlen durch Materie. *Annalen der Physik*, *397* (3), 325-400. (https://onlinelibrary.wiley.com/doi/abs/10.1002/andp.19303970303 [accessed 04-July-2019]) doi: 10.1002/andp.19303970303

Biebel, O., Binder, M., Boutemeur, M., Brandt, A., Dubbert, J., Duckeck, G., ... others (2003). A Cosmic Ray Measurement Facility for ATLAS Muon Chambers. *arXiv preprint physics/0307147*. (https://arxiv.org/pdf/physics/0307147.pdf [accessed 04-July-2019])

Bortfeldt, J. (2014). *Development of Floating Strip Micromegas Detectors* (Unveröffentlichte Dissertation). Ludwig-Maximilians Universität, München.

Brüning, O. S., Collier, P., Lebrun, P., Myers, S., Ostojic, R., Poole, J. & Proudlock, P. (2004). *LHC Design Report.* Geneva: CERN. (http://cds.cern.ch/record/782076/files/CERN-2004-003-V1-ft.pdf) doi: 10.5170/CERN-2004-003-V-1

Caron, J.-L. (1998, May). *Overall view of LHC experiments. Vue d'ensemble des experiences du LHC.* Zugriff auf https://cds.cern.ch/record/841555 (AC Collection. Legacy of AC. Pictures from 1992 to 2002.)

De Geronimo, G., Fried, J., Li, S., Metcalfe, J., Nambiar, N., Vernon, E. & Polychronakos, V. (2012, Oct). VMM1 - An ASIC for micropattern detectors. In *2012 ieee nuclear science symposium and medical imaging conference record (nss/mic)* (S. 633-639). doi: 10.1109/NSSMIC.2012.6551184

Flierl, B. (2018). *Particle Tracking with Micro-Pattern Gaseous Detectors* (Unveröffentlichte Dissertation). Ludwig-Maximilians Universität, München.

Giomataris, Y., Rebourgeard, P., Robert, J. P. & Charpak, G. (1996). MICROMEGAS:

a high-granularity position-sensitive gaseous detector for high particle-flux environments. *Nuclear Instruments and Methods in Physics Research, Section A*, *376*, 29-35.

Groom, D. E., Mokhov, N. V. & Striganov, S. I. (2001). Muon Stopping Power and Range Tables 10 MeV - 100TeV. *Atomic Data and Nuclear Data Tables*, *78(2)*.

Herrmann, M. G. (2019). *Series calibration of segmented and multi-layered micromegas modules for atlas* (Unveröffentlichte Dissertation). lmu.

Iengo, P., Alviggi, M., Iodice, M. & Sekhniaidze, G. (2018, Dezember). *Effect of humidity on resistive micromegas.* Private Communication. (Internal Presentation ATLAS Muon Week, https://indico.cern.ch/event/761831/contributions/3236872/attachments/1764954/2865110/20181204-ExMeRH-RD51MiniWeek-Iengo.pdf,[accessed 21-December-2020])

Klitzner, F. (2019). *Development of Novel Two-Dimensional Floating Strip Micromegas Detectors with an In-depth Insight into the Strip Signal Formation* (Unveröffentlichte Dissertation). Ludwig-Maximilians Universität, München.

Kortner, O. (2002). *Schauerproduktion durch hochenergetische Myonen und Aufbau eines Höhenstrahlungsprüfstandes für hochauflösende ATLAS-Myonkammern* (Unveröffentlichte Dissertation). Ludwig-Maximilians Universität.

Lösel, P. (2017). *Precision Calibration of Large Area Micro Pattern Gaseous Detectors* (Unveröffentlichte Dissertation). Ludwig-Maximilians Universität, München.

Olive et al. (2014, 1. 8). Review of particle physics. *Chinese Physics C*, *38* (9). doi: 10.1088/1674-1137/38/9/090001

Pequenao, J. (2008, Mar). *Computer generated image of the whole ATLAS detector.* (https://cds.cern.ch/record/1095924 [accessed 06-August-2019])

Raether, H. (1964). *Electron Avalanches and Breakdown in Gases*. London: Butterworths.

Rauscher, F. (2005). *Untersuchung des Verhaltens von Driftrohren bei starker Gamma-Bestrahlung sowie Vermessung von Driftrohrkammern mit Hilfe von Myonen der kosmischen Höhenstrahlung* (Unveröffentlichte Dissertation). Ludwig-Maximilians Universität, München.

Sidiropoulou, O. (2018). *Characterization of the ATLAS-type Micromegas Detectors* (Unveröffentlichte Dissertation). Julius-Maximilians-Universität, Würzburg.

Townsend, J. (1910). *The theory of ionization of gases by collision.* Van Nostrand. (https://archive.org/details/theoryofionizati00townuoft [accessed 04-July-2019])

Appendix

Appendix A: Vaisala Dewpoint Transmitter

The "Vaisala DMT 143 Dewpoint Transmitter" was used to measure water portions in the working gas. To read and record the sensor output, the Vaisala can be connected to a computer via a cable connected to the digital port. The sensor is covered with a special cap, which connects to FESTO tubing.
As experience has shown, the cap needs to be re-tightened after prolonged use, as they tend to loosen (likely due to being moved during handling).

Figure 5.1: Vaisala DMT 143. Taken from https://www.vaisala.com/de/products/instruments-sensors-and-other-measurement-devices/instruments-industrial-measurements/dmt143

Connection for readout: A single Vaisala can be connected to a computer via the USB connector "USB Service Cable M8-4F, RS485" (Product code: 219690; `https://store.vaisala.com/en/spares/219690`).
This thesis used an Arduino and a specifically made wiring harness to simultaneously read several Vaisalas.

To communicate with one Vaisala: Open a terminal and search for it:
("ls /dev/tty*").
There should be a "/dev/ttyUSB[n]" if connected via USB port, or a
"/dev/ttyACM[n]" if connected via Arduino ([n] being an integer).

"screen /dev/ttyACM[n] 19200" (/ttyUSB respectively). A black screen should appear. Type "?" or "??" (*question mark*) and press enter. The Vaisala information (including its address integer) should be displayed. Alternatively use 'send' to see if readout is displayed.

Common commands: The commands can be found in the manual. Presented are the ones used most frequently for this thesis:

send: Prints the output of all open Vaisalas. (Only useful for one open Vaisala, as multiple will result in a faulty display)

send n: Prints the output of the Vaisala with address 'n'. Works for *closed* ones (as used in the python program).

addr n: Sets the address of all(!) open Vaisalas to 'n'.

open n: Puts the Vaisala with address 'n' into 'open' mode.

close n: Puts the Vaisala with address 'n' into 'closed' mode.

?: Displays the information for the open Vaisala(s)

Appendix B: Arduino-Readout

To set up an Arduino, you need to load the appropriate sketch into it. The sketch can be found under "$/project/etp3/strost/Arduino/$Arduino_Serial". The executable code for 3 Vaisalas under: "$/project/etp3/strost/H2O/vaisalaPerfect.py$".
The code needs to be executed with "python3 vaisalaPerfect.py". It will create a textfile (with the current date) at the output-folder (defined in code) and fill it with the readout for every connected Vaisala each second, until terminated. For a setup with more/less than 3 Vaisalas, change the corresponding parameter in the code.

To assign an address for Vaisala: Each Vaisala needs its own address and you need to assign each address individually (see manual or Appendix A). Before plugging in the next Vaisala, close the one(s) in open state (or disconnect them). Vaisalas remember their assigned address when disconnected.
Stay in the screen for the next Vaisalas. Upon connection of a new Vaisala, its information should appear.

Troubleshooting: Solutions and work-arounds for encountered problems.

2+ Vaisalas on the Arduino: Make sure the extra power supply is connected to the wiring harness.

All Vaisalas should be in 'closed' mode so to not interfer with each other. A freshly connected Vaisala will be in 'open' mode. Use the screen to 'close' it.

"Screen terminating / Permission denied":
use "ssh [user]@[thisPC]" to log yourself in on the computer you're already logged in and try again to screen the Vaisala.

no module named serial:
"python3", ">>> import serial" (or unplug and plug in the USB connection).

Nothing happens:
Check if the led of the Vaisala is on

'Gibberish':
Check if all Vaisalas have different addresses and if all are in closed mode.

'Off values':
Vaisalas are auto-calibrating. It takes several minutes until the values are precise. This can also lead to small steps during prolonged measurements.

Arduino Sketch:

```
/*
  Multiple Serial test

  Receives from the main serial port, sends to the others.
  Receives from serial port 1, sends to the main serial (Serial 0).

  This example works only with boards with more than one serial like
Arduino Mega, Due, Zero etc.

  The circuit:
  - any serial device attached to Serial port 1
  - Serial Monitor open on Serial port 0

  created 30 Dec 2008
  modified 20 May 2012
  by Tom Igoe & Jed Roach
  modified 27 Nov 2015
  by Arturo Guadalupi

  This example code is in the public domain.
*/

#include <SoftwareSerial.h>

SoftwareSerial mySerial (4, 5);
void setup() {
  // initialize both serial ports:
  Serial.begin(19200);
  mySerial.begin(19200);
}

void loop() {
  // read from port 1, send to port 0:
  if (mySerial.available()) {
    int inByte = mySerial.read();
    Serial.write(inByte);
  }

  // read from port 0, send to port 1:
  if (Serial.available()) {
    int inByte = Serial.read();
    mySerial.write(inByte);

  }
}
```

Program to read 3 Vaisalas:

```
import serial
import time
import sys
import datetime
import io

#==============================================================================
#Running for one Vaisala (Vaisalas at 2,3,4)
#
#
#ser=serial.Serial("/dev/ttyACM0",19200)
#
#while 1:
#
# ser.write(b'send 2\r\n')
#
# result=ser.readline()
#
# print(result)
#
#
# time.sleep(1)
#
#==============================================================================

# original plan: count = 0 -> vais = 2 + (count%3) for iteration

vaisala = 1                  # first Vaisala address
vaisCount = 2                # highest address-number of vaisalas connected
vais_step = 1                # address steps between vaisalas (demands adresses to be equally apart from each other)

txtTitle = "/project/etpdaq4/strost/CRFH20/dataHumid/h2o_ppm_"  # creates file at specific location
txtTitle += datetime.datetime.now().strftime("%Y%m%d-%H%M%S")  # creates file with unige name by using date and time
txtTitle += ".txt"

ppm = open(txtTitle, "w+" )    # w creates new file if none exists with the name | + for read and write

ser=serial.Serial("/dev/ttyACM1", 19200, timeout=1)

#------------------------------------------------
vais_iterate = vaisala
iteration_step = 0


print('Closing chosen Vaisalas:')
for vaisClosure in range(vaisala, vaisCount+1):
```

```
    vais_close = 'close '
    vais_close += str(vaisClosure)
    vais_close += '\r\n'
    ser.write(vais_close.encode('utf-8'))
#     print(vais_close)
print('   Vaisalas closed')


while 1:        #later: "while 1:" || now short loop for debug

    print(iteration_step)

    while vais_iterate <= vaisCount:

        command = 'send '
        command += str(vais_iterate)
        command += '\r\n'
#         print(command)

        ser.write(command.encode('utf-8'))
#         print('command: ', command )

        result = ser.readline()
#         print('readline: ', result)
        results_raw = str(result)
#         print(results_raw)
        results_cut0 = results_raw.split( 'ppm' )[0]
        results_cut1 = results_cut0.split("H2O")[1]
        results_cut2 = results_cut1.strip('/***')
        results_cut3 = results_cut2.replace('\\***','') # replace( , )/strip
        results_cut4 = results_cut3.replace("\\x90",'') # replace( , )/strip
        results_cut5 = results_cut4.strip('\xb0').replace('\\x**','')
        results_cut6 = results_cut5.strip('\xa2').strip('\xb0')

        results = 'Vaisala'+str(vais_iterate)+': H2O'+results_cut6+'ppm'+"||     unixtime " + datetime.datetime.now().strftime("%s")

        if vais_iterate < vaisCount:
            results += '\n'
        else:
            results += '\n\n'

        print(results)

        ppm.write( results )
#         print('empfangen')

        if vais_iterate < vaisCount:
            ppm.write('\n')
```

```
        else:
            ppm.write('\n\n')

        vais_iterate += vais_step

    iteration_step += 1


#    print(result)

    vais_iterate = vaisala                    # reset to first Vaisala address

    time.sleep(1)
```

Appendix C: Festo Verbindungstechnik

http://www.festo.com/cat/de_de/products_071000
Part numbers: soft tubing 159664, hard tubing 558206

Appendix D: CRF Temperature

The CRF has temperature control, which kept the temperature within a range of 3° C during mid July .

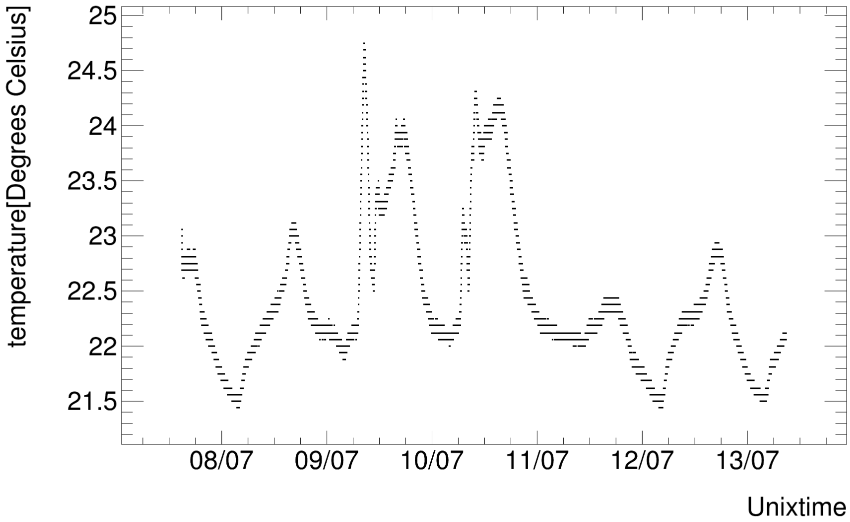

Figure 5.2: Temperature measurement at the CRF early July.

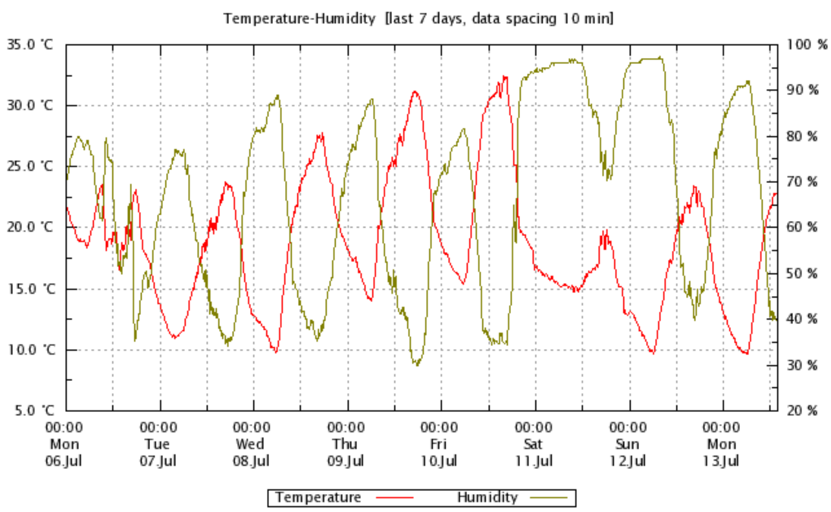

Figure 5.3: Temperature and humidity at Garching Forschungszentrum. Taken from `http://www.wetter-garching.de/week.html`

Appendix E: Additional Graphics

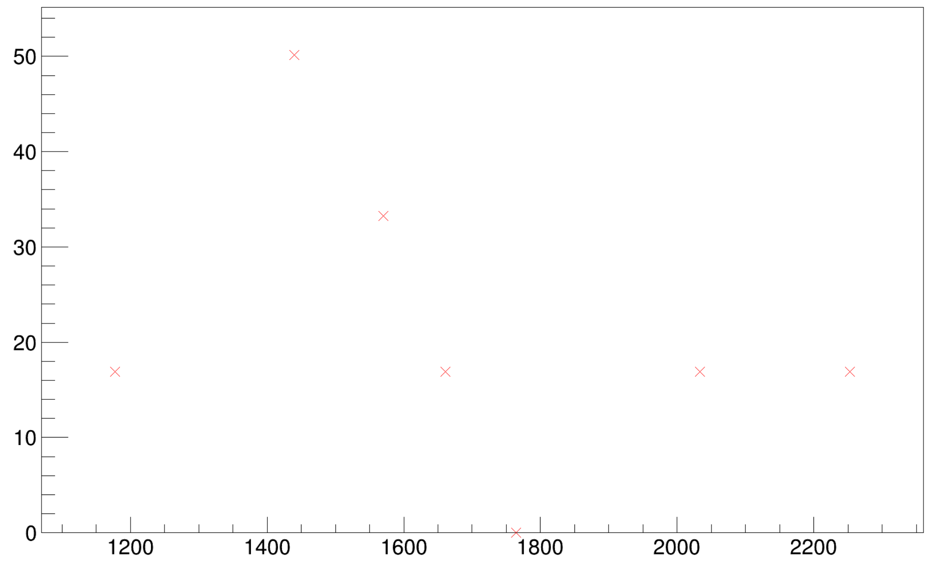

Figure 5.4: Event display of the muon event showcased in chapter 5, without visual overlays.

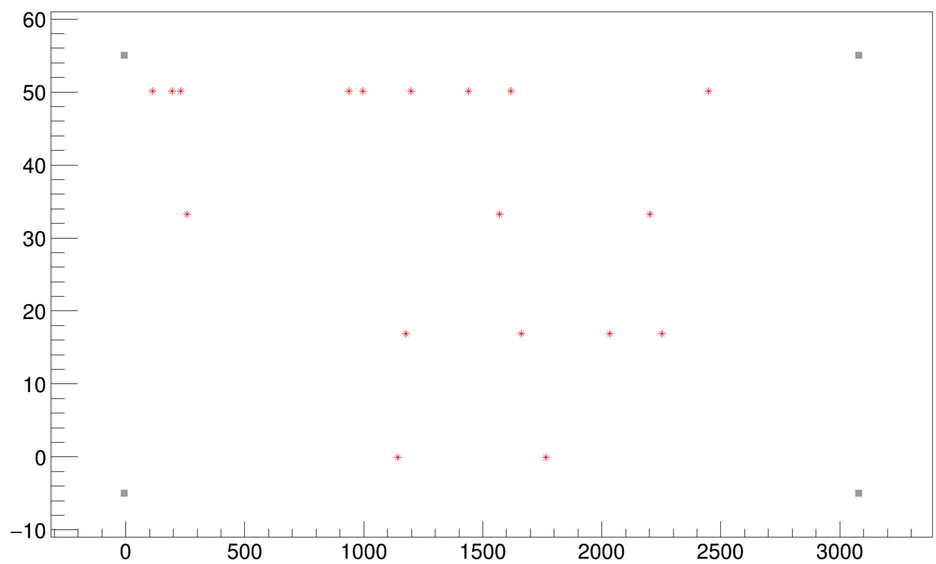

Figure 5.5: Event display of the complete muon event showcased in chapter 5. All clusters are depicted.

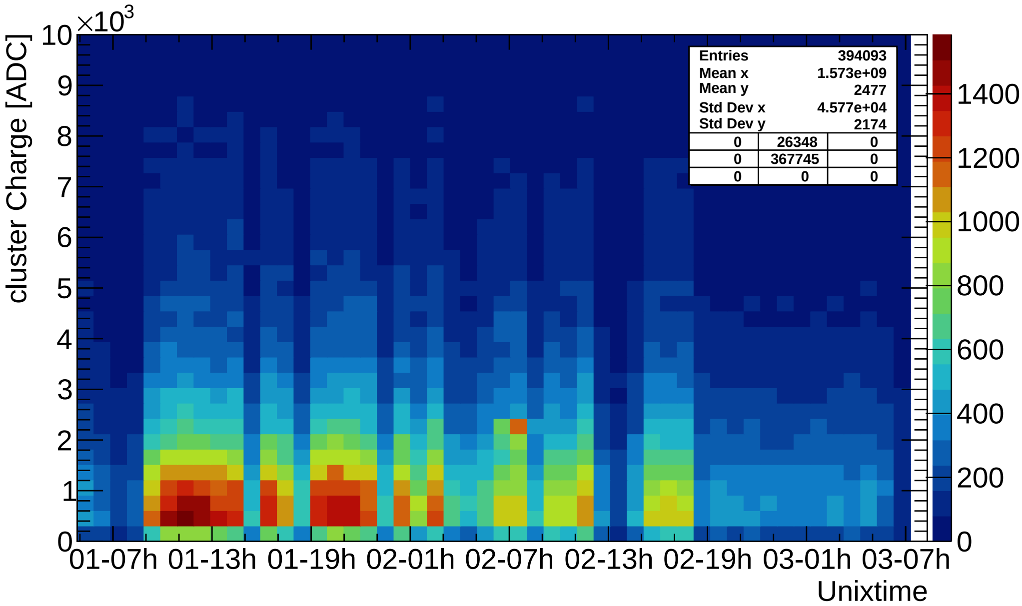

Figure 5.6: Total charge in EI as a function of time. Depicted are the charges of all clusters.

Acknowledgements

Finally I'd like to thank all the people who made this thesis the wonderful experience it was.

I want to thank Prof. Dr. Otmar Biebel for the chance to do this thesis, for his dedication towards his students and the knowledge he shared with us beyond our work and even the field of physics.

I'm grateful to Prof. Dr. Dorothee Schaile for the environment she created through her leadership.

My sincere gratitude goes to my supervisor Dr. Maximilian Herrmann, for his teaching, caring and company.

My special thanks to Dr. Ralf Hertenberger, who so close to Christmas dedicated time to proofreading.

I am thankful to all the members of the *Hardware Group* I've met and worked with: Dr. Bernhard Flierl, Christoph Jagdfeld, Dr. Felix Klitzner, Katrin Penski, Maximilian Rinnagel, Dr. Chrysostomos Valderanis and Fabian Vogel.
A group that friendly and supporting is not to be taken for granted. It was my pleasure to work alongside all of you.

Finally I dedicate this thesis to my beloved partner Gloria Zörnack and my family, whose support and love compelled and enabled me to do this thesis in the first place.

Statutory declaration

Hiermit erkläre ich, die vorliegende Arbeit selbständig verfasst zu haben und keine anderen als die in der Arbeit angegebenen Quellen und Hilfsmittel benutzt zu haben.

Munich, ...
Sebastian Trost